Application of Engineered Cementitious Composites for Enhanced Wellbore Integrity During Geologic Carbon Sequestration

by

Jubilee T. Adeoye

A dissertation submitted in partial fulfillment
of the requirements for the degree of
Doctor of Philosophy
(Environmental Engineering)
in the University of Michigan
2019

Doctoral Committee:

Assistant Professor Brian R. Ellis, Chair
Dr. Nicolas Huerta, Pacific Northwest National Laboratory
Professor Victor C. Li
Assistant Professor Selena Y. Smith

Jubilee Adeoye

jtadeoye@umich.edu

ORCID iD: 0000-0002-3494-3694

DEDICATION

To my parents Professor Gideon Olajire Adeoye and Dr. Comfort Modupeore Adeoye. Thank you for your unconditional love, support, and sacrifices over the years. I could not have made it this far without you. You are my heroes.

ACKNOWLEDGMENTS

This dissertation work is partly supported by the U.S. Department of Energy through grant DE-FE0030684. I also received funding support from the Rackham Graduate School through the Rackham Predoctoral Fellowship, Rackham Travel Grant, and Rackham Professional Development Grant programs.

I would like to acknowledge my advisor Dr. Brian Ellis for giving me the opportunity to carry out research as a graduate student in his research group. Thank you for your consistent support and mentorship while I carried out this dissertation work and for giving me the freedom to explore my areas of interest. I particularly appreciate your patience and encouragement during the challenging seasons; I could always count on you to look out for my best interest. I would also like to thank Dr. Victor Li for inspiring my interest in Engineered Cementitious Composites. Your willingness to share your knowledge and expertise was pivotal in completing this work. My special thanks go to my dissertation committee members Dr. Selena Smith and Dr. Nicolas Huerta for their helpful feedback, guidance, and insight on my work.

I am grateful for the support of my current and former colleagues who have been very instrumental in my research. I have been fortunate to work in a great environment with bright minds; people who are always willing to share their knowledge and lend a helping hand. In particular, I will like to appreciate Anne Menefee, Duo Zhang, Saikat Das, and Alex Naves Jr, with whom I have worked closely on several projects and who have contributed significantly to my success. I am also grateful for the staff in the Department of Civil and Environmental

Engineering for providing support in various aspects of my work. Steve Donajkowski was very instrumental in helping to design and construct several of my experimental setups. Thank you, Steve, for always going the extra mile and for being a great friend. I would like to thank Tom Yavarasky for all his support with my sample analysis and setting up of the lab. I also truly appreciate all our conversations in the hallway.

My sincere gratitude goes to my parents, Gideon and Comfort, who have always been there for me. I am grateful for all your prayers, love, and encouragement. You two are my greatest blessing and I cannot thank you enough. I also want to appreciate my siblings Morenike Joose, Mission Oludun, Beulah Ayodeji, Zion Ekundayo, David, and Comfort Abeni. Thank you all for inspiring and supporting me in many ways. I would also like to acknowledge my brother Tolulope Jeremiah, who, although no longer with us, continues to inspire me by this his lifelong example of dedication, hard work, generosity, and selflessness. I also want to thank my girlfriend, Tere Cooley, for her love, friendship, and support. Thanks for all your words of encouragement and for making my memories of graduate school beautiful. I also want to thank my girlfriend's parents Teressa and Lawrence for their support and generosity.

I have been privileged to have a great community of friends at the University of Michigan while carrying out this work. I would like to acknowledge my friends at the Redeemed Christian Fellowship and the Harvest Mission Community Church. It is great to have a family of believers that support you during challenging times. In particular, I will like to acknowledge my friends Samuel Ayinde and Tiwa Ajbewa for being a huge source of encouragement and friendship throughout my dissertation work. I also want to thank Kunle and Ashley Adebiyi for their constant generosity and words of encouragement.

TABLE OF CONTENTS

LIST OF TABLES

LIST OF FIGURES

LIST OF APPENDICES

ABSTRACT

Geologic carbon storage (GCS), which entails the capture of carbon dioxide (CO_2) from large CO_2 emitters and storage in deep geologic formations, is being proposed as a bridging technology to combat global climate change caused by the emission of anthropogenic CO_2. However, leakage of CO_2 from storage reservoirs, such as through damaged wellbore cement sheaths, remains a major challenge for GCS. Laboratory and field studies carried out over the past decade have provided significant insight regarding the alteration mechanisms in traditional wellbore cement exposed to CO_2 during GCS and indicate that deterioration of the physical and mechanical properties of the wellbore cement could occur in the long-term when exposed to CO_2. However, very little work has been done to investigate substitute materials that can prevent such cement sheath deterioration during GCS. In this dissertation, a novel ultra-ductile fiber-reinforced cementitious composite, engineered cementitious composites (ECC), is proposed as a substitute material for wellbore cement used during GCS to ensure superior mechanical performance of cement sheaths. Conventional ECC was exposed to CO_2 under typical GCS reservoir temperature and pressure conditions and X-ray computed tomography and scanning electron microscopy analyses were carried out on the reacted and unreacted materials to understand the unique changes in ECC's microstructure. Results showed that the interaction of ECC with CO_2 would alter its microstructure uniquely. Particularly, the fiber/matrix interfacial transition zone (ITZ) will be densified due to carbonation reactions. Further studies carried out to investigate the implication of the ITZ densification on a version of ECC rheologically re-engineered for wellbore cementing applications showed that the densification of the ITZ reduced the ductility of ECC. However, the altered ECC

continued to exhibit superior ductile performance in comparison to conventional wellbore cement. Additionally, ECC exhibited fluid transport characteristics comparable to conventional wellbore cement, which suggests that it will be an effective diffusive barrier to limit the movement of fluids through the cement sheath. To investigate cyclic crack healing in damaged ECC, pre-cracked specimens were exposed to CO_2 under typical GCS environmental conditions and permeability evolution was determined at various time points. Crack healing occurred in several specimens under the different conditions tested. Specimens exposed to CO_2-acidified water, which simulates the environmental conditions near the downhole region of the wellbore, exhibited the most significant crack healing, accompanied by a substantial reduction in permeability. Similarly, specimens exposed to CO_2-acidified water recorded the least decline in tensile strain capacity and a significant increase in tensile strength post carbonation, indicating that the application of ECC as a primary cementing material is most viable in the downhole region of GCS. This study establishes ECC as a promising candidate for consideration as a substitute wellbore cementing material during GCS to ensure secure storage of CO_2.

CHAPTER 1

Introduction

1.1 Background and motivation

1.1.1 Greenhouse gas emissions and global climate change

Climate change is one of the most pressing global concerns today with far-reaching consequences that are already being experienced, as evidenced by record annual temperatures, rising sea levels, extreme drought, and record-setting flooding events in various parts of the world (Frumkin et al., 2008; Mirza, 2003). Although there are still uncertainties regarding how climate change will impact different regions, studies have shown that there is a correlation between the rapidly changing global climate and the warming of our atmosphere, which has been linked to excessive emissions of anthropogenic greenhouse gases (GHGs).

According to the U.S. Environmental Protection Agency (EPA), GHGs are gases that have the tendency to trap heat in the atmosphere. Although these gases allow sunlight with relatively shortwave energy to reach the surface of the earth unhindered, they absorb and trap longer-wave energy in the atmosphere, permitting less heat to escape back to space. Such gases can occur naturally or as a result of human activities. Greenhouse gases of importance include carbon dioxide (CO_2), methane (CH_4), ozone (O_3), nitrous oxide (NO_2), and chlorofluorocarbons (CFCs). In particular, the emission of anthropogenic CO_2, a byproduct of fossil fuel combustion, is a major concern because of extensive burning of coal, refined crude oil products, natural gas, and biomass on a global scale for transportation, electricity and heat generation, industrial production,

construction, and recreation. According to the Intergovernmental Panel on Climate Change (IPCC) report of 2014, CO_2 accounts for over 75% of total greenhouse gas emissions (IPCC and Edenhofer, 2014) and thus deserves attention in order to limit the potential of irreversible global climate change.

1.1.2 CO_2 mitigation strategies

Several strategies and technologies are being proposed and adopted to limit the emission of CO_2 and ensure a cleaner energy future. These technologies can be divided into two broad groups. The first seeks to reduce or limit the quantity of CO_2 generated by switching to less carbon-intensive energy sources such as wind, nuclear, solar, tidal, and hydropower (Burton et al., 2001; Sims et al., 2003). This approach also includes technologies that convert coal-fired power plants, which are largest point source CO_2 emitters, to natural gas, thus reducing the amount of CO_2 emissions per unit of energy generated (Jaramillo et al., 2007; Turconi et al., 2013; World Nuclear Association (WNA), 2011). Additionally, the implementation of a carbon tax and credit system to encourage users to limit their CO_2 emissions has been proposed in several countries around the world (Metcalf, 2009). The second approach is carbon capture, utilization, and storage (CCUS). CCUS involves capturing and storing the emitted CO_2, either from large point sources (e.g. coal-fired power plants, cement plants, and oil and gas refineries) or through direct air capture, and either storing the captured CO_2 in deep geologic formations (Friedmann, 2007) or utilizing it to produce valuable products such as plastic (Darensbourg, 2007), liquid fuels (Hou et al., 2011; Hu et al., 2013; Varghese et al., 2009), or high-strength concrete (Lim et al., 2010; Shao et al., 2006).

Although low-carbon technologies can be very effective for controlling emissions in the long term, large-scale adoption is needed in the short term to achieve targets for limiting global temperature rise and avoid irreversible climate change. However, such large-scale adoption may

be unrealistic in the short term due to limitations with our current energy infrastructures and the significant dependence of our current energy mix on fossil fuels. It is, therefore, necessary to adopt a bridging technology that can be coupled with current energy infrastructure to achieve the short-term CO_2 emissions targets.

1.1.3 Geologic carbon storage

Geologic carbon storage is the capture of CO_2 from large point sources and subsequent storage in deep geologic formations such as depleted oil and gas reservoirs (Bergman et al., 1997; Koide et al., 1992; Le Gallo et al., 2002; Li et al., 2006), deep saline aquifers (Bachu and Adams, 2003; Nordbotten et al., 2005), unmineable coal seams (Reeves, 2001; Shi and Durucan, 2005), and stable basalt formations (Adeoye et al., 2017; McGrail et al., 2006; Menefee et al., 2017; Xiong et al., 2017). Because fossil fuels are expected to continue to serve as the primary source of energy for the next several decades, GCS is considered an important technology in the portfolio of climate change mitigation strategies to stabilize the atmospheric concentration of CO_2 (IPCC and Metz, 2005). GCS is very attractive to slow climate change because of its potential to eliminate large streams of CO_2. Current estimates of global CO_2 storage capacity exceeds several thousand gigatonnes ($GtCO_2$), which is significant considering that the annual global emissions of CO_2 are approximately 30 $GtCO_2$ (Friedmann, 2007). Additionally, there is a vast knowledge base that can be leveraged to deploy GCS on a global scale because the requisite technologies are similar to technologies that have been used for several decades in the petroleum industry for crude oil and natural gas recovery. When coupled with CO_2-enhanced oil recovery, GCS also has the potential to increase revenue streams from oil and gas recovery (IPCC and Metz, 2005).

1.1.4 Wellbore cementing and Integrity

During GCS, wells are drilled into the geologic formation to access a porous and permeable CO_2 storage zone. This operation involves a completion process that begins with the installation of steel casings along the wellbore to support the geologic formation and prevent it from caving. Subsequently, a cement slurry is pumped into the annular gap between the steel casing and formation to isolate the different fluid-bearing zones, which prevents fluid migration, provides structural support for the well casing, and protects the steel casing from corrosion by reducing contact with reservoir fluids in the formation (Nelson, 1990). Following the installation of the cement sheath, the downhole region of the well is perforated to aid the flow of the CO_2 into the reservoir. At the end of the well's service life, the well will be plugged with cement in different zones to prevent the flow of CO_2 to the surface. This plugging process is referred to as well abandonment. **Figure 1.1** illustrates elements of a typical completed well.

One of the major challenges for GCS is the potential leakage of CO_2 from the reservoir. In particular, wellbores have been identified as potential leakage pathways for CO_2 during GCS (Bachu and Celia, 2009)**.** This is because the process of wellbore installation and CO_2 injection operations can create damaged zones near the wellbore that can act as CO_2 leakage pathways. To ensure the use of appropriate materials and safe construction techniques that will limit such leakage, the EPA has developed guidance for wellbore cementing during GCS that leverages the tested recommended practices set out by the American Petroleum Institute (API) for wellbore cementing during oil and gas recovery (American Petroleum Institute, 2010; EPA, 2012). However, legacy wells installed in potential CO_2 repositories during the 20th century using substandard, outdated materials and methods pose leakage risk, and such leakage continues to

hinder the prospective long-term success of GCS as a carbon mitigation strategy (Carroll et al., 2016; Watson and Bachu, 2009). According to the U.S. Department of Energy (DOE), GCS operations must achieve a storage efficiency of 99% to be an effective technology to mitigate the increase in the atmospheric concentration of CO_2 (Chow et al., 2003; DOE, 2007).

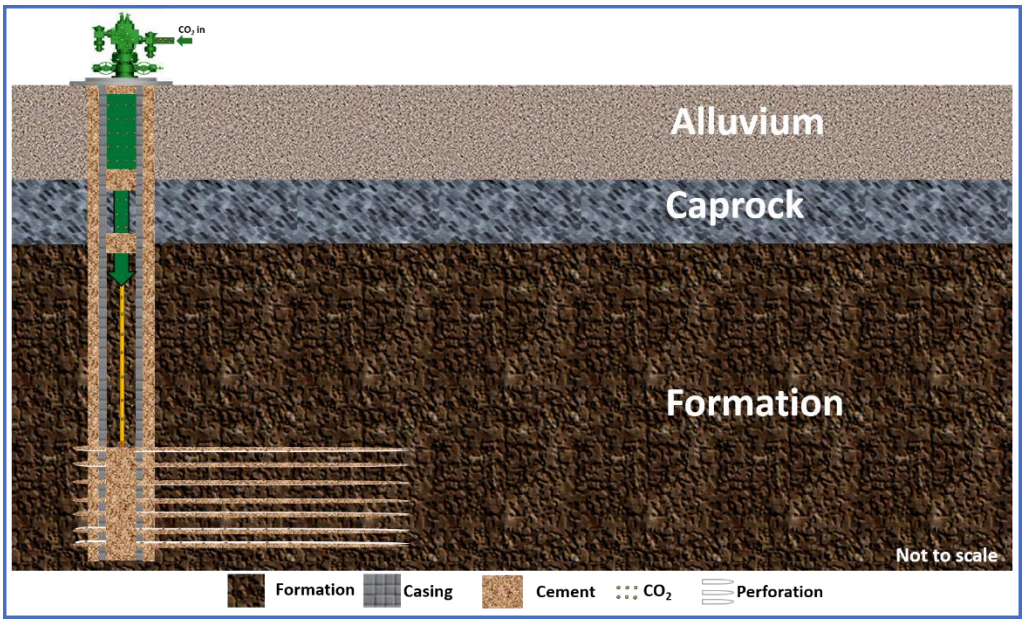

Figure 1.1: Schematics of a typical completed wellbore during geologic CO_2 carbon storage. Image not drawn to scale.

Figure 1.2 illustrates potential CO_2 leakage pathways through wellbores in CO_2 storage reservoirs. These pathways include open-hole flow (*Path 1*), dissolution-induced flow pathways (*Path 2*), damaged steel casing (*Path 3*), steel casing-cement interfaces (*Path 4*), fractured cement sheath (*Path 5*), and formation-cement interface (*Path 7*). Of these pathways, fractured cement sheath and cement-casing/cement-formation interfaces have been identified as the most likely leakage pathways (Carroll et al., 2016).

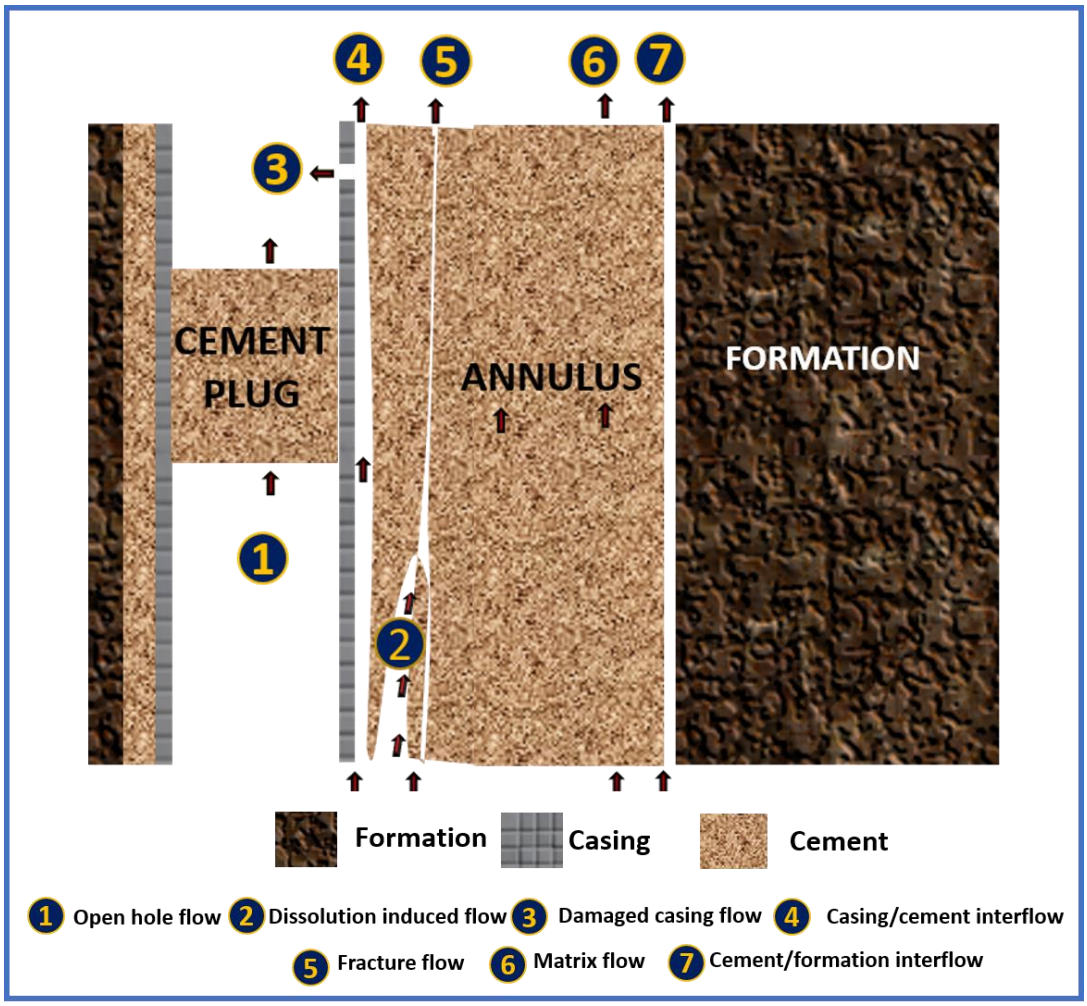

Figure 1.2: Pictorial model showing various CO_2 leakage pathways for CO_2 from a geologic, through a plugged well, during GCS. Image not drawn to scale.

While the cement sheath interfaces are primarily caused by poor adhesion of the cement slurry to the steel casing and formation or debonding of the cement sheath due to cement shrinkage during curing, fractures can be generated in the cement sheath due to pressure and temperature swings in the reservoir during its operating life, overpressure during CO_2 injection into the formation, and chemically induced reactive cracking of the material due to the formation of calcium carbonates (Sahmaran et al., 2007; Wigand et al., 2009). Regardless of the mode of fracture initiation, these fractures may continue to dilate once initiated due to downhole stresses and continuous dissolution at the fracture interface as a result of chemical attacks, leading to larger

pathways that can promote leakage of CO_2 to the atmosphere. Conversely, fractures can self-heal following the precipitation of calcium carbonate within the fracture aperture, restricting the further flow of CO_2-enriched fluid from the reservoir (Carroll et al., 2016).

To understand the processes that promote or inhibit cement sheath fracture dilation or self-healing, a thorough understanding of the chemical composition and chemistry of cement is needed. Ordinary Portland cement (OPC) is made from oxides of calcium, aluminum, iron, and silicon, which are reacted together at high temperatures of ~ 1,450^{o}C in a rotary kiln to produce a material called clinker. OPC is polycrystalline and is composed of four major minerals, namely tricalcium silicate ("$3CaO.SiO_2$" or "C_3S"; alite; 21 to 67%), dicalcium silicate ("$2CaO.SiO_2$" or "C_2S"; belite; 0 to 49%), tricalcium aluminate ("$3CaO.Al_2O_3$" or "C_3A"; 1 to 17%) and tetracalcium aluminoferrite ($4CaO.Al_2O_3.Fe_2O_3$" or "C_4AF"; 6 to 18%) (Bourgoyne, 1986; Li et al., 2015a; Nelson, 1990). For oil and gas wells, additives such as magnesium oxide (MgO) and gypsum ($CaSO_4.2H_2O$) are blended into the cement clinker to enhance its mechanical properties and resistance to acid attack. Based on the blend and purpose of the cement application, the American Petroleum Institute (API) has classified these materials into classes from A to H. Cement classes A, G, and H are typically used for oil well cementing jobs (Liteanu and Spiers, 2011; Michaux et al., 1990). The hydrated form of OPC is composed of two major components, namely calcium silicate hydrate (C-S-H; ~ 70% of hydrated cement) and portlandite ($Ca(OH)_2$; ~ 20% of hydrated cement) (Nelson, 1990). When in contact with CO_2-acidified fluids under GCS conditions, the calcium-rich hydrated phases in the cement ($Ca(OH)_2$ and C-S-H) will dissolve, releasing copious amounts of calcium ions and leaving behind a porous and mechanically-weak amorpoush silicate phase ($amSiO_2$). Such acid attack can weaken the cement sheath following alteration. Conversely, because hydrated cement contains a significant amount of portlandite, which is a strong base, and

the pore fluid pH of unaltered cement is strongly alkaline, it provides a buffered environment suitable for calcium carbonate ($CaCO_3$) precipitation following acid attack (Johnson et al., 2004; Kutchko et al., 2007). Carbonate precipitates can fill the cement pores and enhance its compressive strength (Shao et al., 2006).

Studies carried out on neat (i.e. cement with no additives) intact cement cores under different temperature and pressure conditions show that following several days of reaction between cement specimens and CO_2-acidified water, three distinct reaction zones will form in an altered cement specimen (Brunet et al., 2013; Kutchko et al., 2008, 2007). The outer zone in direct contact with CO_2-acidified water will be altered extensively due to the dissolution of Portlandite and CSH, according to the chemical reaction presented in **Eq. 1.1** and **Eq. 1.2**, respectively, and is characterized as amorphous silica-rich silica gel with high porosity and lower structural integrity in comparison to the unaltered cement (Kutchko et al., 2008, 2007). Next to the amorphous zone is a region where calcium carbonate precipitation occurs, as described in **Eq. 1.3**, which reduces cement porosity and permeability, resulting in higher compressive strength and hardness relative to the unaltered cement (Kutchko et al., 2007; Li et al., 2015a). The reduced porosity and permeability due to precipitation of calcium carbonate will inhibit further transport of CO_2 into the cement matrix (Bruckdorfer, 1986; Fernández Bertos et al., 2004), which can protect the cement from further deterioration. The third zone is characterized by depletion of calcium, described in **Eq. 1.4**, and increased porosity caused by dissolution of portlandite and outward diffusion of calcium ions into the calcium carbonate-rich zone (Kutchko et al., 2007). Such alteration of the cement has been found to lead to significant deterioration of its mechanical properties (Kutchko et al., 2007; Li et al., 2015a; Mason et al., 2013), and fractures generated in this altered material could act as leakage pathways for CO_2 from geologic formations.

For neat class H cement exposed to supercritical CO_2, Kutchko et al. (2008) observed that in contrast to the three altered zones seen in cement exposed to CO_2-acidified solutions, calcium carbonate was distributed over the entire exterior of the cement, limiting the diffusion of CO_2 into the cement matrix. This absence of reaction zones was due to the lack of water molecules to aid the transport of ions into the cement matrix (Kutchko et al., 2011).

Zone 1: $Ca(OH)_2 \rightarrow Ca^{2+} + 2OH^-$ **Eq. 1.1**

$CSH \rightarrow Ca^{2+} + OH^- + amSiO_2$ **Eq. 1.2**

Zone 2: $Ca^{2+} + HCO_3^- + OH^- \rightarrow CaCO_3 + H_2O$ **Eq. 1.3**

Zone 3: $CaCO_3 + H_2CO_3 \rightarrow Ca^{2+} + 2HCO_3^-$ **Eq. 1.4**

Despite the potential damage of cement in contact with CO_2-rich fluids under GSC conditions, there is consensus that CO_2 diffusion through an intact cement matrix is unlikely to lead to the leakage of CO_2 from the reservoir on timescales of decades (Carey et al., 2007; Kutchko et al., 2008; Liteanu and Spiers, 2011). However, reaction-driven alteration of the wellbore cement can promote cracks and fractures that will enhance permeability and the likelihood of CO_2 leakage from the reservoir (Kutchko et al., 2009; Li et al., 2015b).

While prior wellbore studies on CO_2-cement interactions have helped to develop predictive tools to assess long-term wellbore integrity (Brunet et al., 2016; Carroll et al., 2016; Huerta et al., 2016; Walsh et al., 2013), thereby reducing uncertainties regarding the mechanisms that govern the alteration of conventional wellbore cement under GCS conditions, practical solutions to prevent cement sheath damage, such as developing damage tolerant and self-healing cementitious materials, are lacking (Cunningham et al., 2011). Given that GCS wells need to be constructed with the perspective of serving as permanent protective barriers for stored CO_2, novel damage-

resistant and self-healing cementitious materials that can withstand chemical attacks from CO_2-acidified solutions and potentially self-heal when fractured under GCS conditions need to be developed.

1.1.5 Engineered cementitious composites

Engineered cementitious composites (ECC) are a class of fiber-reinforced cementitious materials also referred to as bendable concrete (Herbert and Li, 2013; Kawabata et al., 2012; Li, 2003, 2002). ECC has a tensile strain capacity in the range of 2 to 5 %, which is about 200 to 500 times greater than conventional Portland cement and concrete. Under tensile stress, ECC undergoes a strain hardening stage during which multiple microcracks (with crack widths less than 60 μm) are formed (Kan et al., 2010). When exposed to CO_2 under atmospheric conditions, ECC has been found to undergo autogenous self-healing that is desirable in wellbore cement where the integrity of the cement matrix is crucial (Herbert and Li, 2013; Yang et al., 2013). ECC incorporates polymer fibers, typically polyvinyl alcohol (PVA), that are randomly distributed in the composite. The interactions between the fibers and the matrix are micromechanically tailored to achieve the desired strain hardening behavior (Li et al., 2002). Additionally, the fibers can promote autogenous crack healing by acting as nucleation sites for healing products such as calcium carbonate (Li and Yang, 2007).

Because of these desirable properties (i.e. high tensile ductility, strain hardening, tight microcracking, and self-healing behaviors) that can be leveraged to ensure the integrity of cement sheath under GCS conditions, ECC is being proposed as a substitute wellbore cementing material for primary cementing in injection wells during GCS. However, the interaction of ECC with CO_2-rich solutions may present new challenges that will impact its long-term mechanical performance as a protective barrier against CO_2 leakage. Before ECC can be adopted as a substitute for

conventional wellbore cement, it is vital to understand its behavior under GCS conditions. We hypothesize that ECC will exhibit similar alteration patterns observed in conventional wellbore cement when exposed to CO_2, but the nature and extent of such alterations and their effect on the long-term integrity of the material are unknown.

1.2 Research Question

The objective of this dissertation is to assess the potential of ECC as a substitute for conventional wellbore cementing materials during GCS. Particularly, this study evaluates the ability of ECC to provide superior structural and mechanical performance compared to conventional wellbore cement and maintain the integrity of the cement sheath, to ensure safe and secure storage of CO_2. In order to achieve the overarching objective of this work, the following questions will be addressed:

Q1. What are the CO_2-driven physical, chemical, microstructural, and micromechanical changes in ECC exposed to CO_2 under typical GCS conditions? How do these alteration patterns compare to those observed in conventional wellbore cementing materials? What is the role of the different components of ECC, particularly microfibers, for such alterations? What are the implications of these changes for the mechanical properties of ECC and its ability to act as an effective long-term seal?

Q2. What is the effect of carbonation reactions on the overall mechanical integrity of ECC? Will ECC tailored for wellbore cementing applications continue to exhibit superior mechanical performance after carbonation in comparison to conventional cement? Will carbonation reactions compromise the strain hardening and multiple microcracking behaviors of ECC? How do the porosity and permeability of ECC evolve under GCS conditions? What are the implications of these porosity and permeability changes for the seal integrity of ECC?

Q3. Can ECC undergo crack healing during GCS? What is the residual tensile strain capacity of self-healed ECC under GCS conditions? Is there a critical crack aperture width beyond which cracks in ECC will cease to self-heal during GCS?

The questions identified above will be addressed in Chapters 2 through 4 of this dissertation. These studies were carried out using a combination of static batch experiments, flow-through experiments, and material characterization techniques. Further information is provided in the chapter summaries.

1.3 Chapter summaries

Chapter 2 addresses the "**Q1**" group of questions. In this chapter, a combination of static batch and flow-through experiments were carried out to investigate the unique effects of CO_2-acidified water on the microstructure of ECC in comparison to conventional wellbore cement. The batch experiments model diffusive mass transport conditions while the flow-through experiment models advective mass transport conditions. The extent of alteration of the ECC at different time points was also evaluated, and the data was used to predict the 50-year extent of alteration in the material using Fick's law of diffusion. Furthermore, the role of PVA fibers for the long-term integrity of ECC and its effect on porosity and permeability was investigated using a combination of x-ray computed tomography (XCT) and scanning electron microscopy (SEM).

Chapter 3 evaluates the effect of carbonation on the mechanical integrity of ECC, which addresses the "**Q2**" group of questions. The work in this chapter builds on the results of Chapter 2, which demonstrated that the fiber/matrix interface will be altered after reacting with CO_2. A wellbore cementing material with rheological properties similar to conventional wellbore cement was exposed to CO_2 under GCS conditions. Several control experiments were conducted to isolate the unique interaction of ECC with CO_2-acidified water. The evolution of the ductility of the

material and the crack patterns were investigated at different time points. To further capture the added benefits of fibers incorporated in ECC, its resistance to deformation in comparison to conventional wellbore cement was investigated using microhardness analysis. Additionally, the evolution of the porosity of the material and its implications for the long-term fluid flow through the ECC matrix was investigated using mercury intrusion porosimetry.

Chapter 4 discusses the **"Q3"** group of questions, which address the potential for crack self-healing in ECC. Crack healing and cyclic crack healing are desirable properties in wellbore cement because wellbore sheath undergoes cyclic stresses due to the intermittent injection of CO_2 into the reservoir. ECC is unique because its strain hardening capacity and superior tensile ductility may enable it to withstand such stresses. To answer this question, ECC samples were strained to 1% tensile strain, leading to the generation of several microcracks, and subsequently exposed to CO_2 under various conditions to test for self-healing. The extent of self-healing following exposure to CO_2 was then investigated by conducting optical microscopy analysis on the healed specimens. Furthermore, the healed samples were strained following self-healing to characterize the residual tensile strain of the composite.

Chapter 5 presents the conclusions of the findings from **Chapter 2** to **Chapter 4** of this dissertation and offers recommendations to improve ECC for future application during GCS. Potential areas for future work are also discussed.

1.4 References

Adeoye, J.T., Menefee, A.H., Xiong, W., Wells, R.K., Skemer, P., Giammar, D.E., Ellis, B.R., 2017. Effect of transport limitations and fluid properties on reaction products in fractures of unaltered and serpentinized basalt exposed to high PCO_2 fluids. Int. J. Greenh. Gas Control 63, 310–320. https://doi.org/10.1016/j.ijggc.2017.06.003

American Petroleum Institute, 2010. Specifications for cements and materials for cementing, 24th ed.

Bachu, S., Adams, J.J., 2003. Sequestration of CO_2 in geological media in response to climate change: capacity of deep saline aquifers to sequester CO_2 in solution. Energy Convers. Manag. 44, 3151–3175. https://doi.org/10.1016/S0196-8904(03)00101-8

Bachu, S., Celia, M.A., 2009. Assessing the potential for CO2 leakage, particularly through wells, from geological storage sites, in: Geophysical Monograph Series. American Geophysical Union, Washington, D. C., pp. 203–216.

Bergman, P.D., Winter, E.M., Chen, Z.-Y., 1997. Disposal of power plant CO_2 in depleted oil and gas reservoirs in Texas. Energy Convers. Manag., Proceedings of the Third International Conference on Carbon Dioxide Removal 38, S211–S216. https://doi.org/10.1016/S0196-8904(96)00271-3

Bourgoyne, A.T. (Ed.), 1986. Applied drilling engineering, SPE textbook series. Society of Petroleum Engineers, Richardson, TX.

Bruckdorfer, R.A., 1986. Carbon Dioxide Corrosion in Oilwell Cements. Presented at the SPE Rocky Mountain Regional Meeting, Society of Petroleum Engineers. https://doi.org/10.2118/15176-MS

Brunet, J.-P.L., Li, L., Karpyn, Z.T., Huerta, N.J., 2016. Fracture opening or self-sealing: Critical residence time as a unifying parameter for cement–CO_2–brine interactions. Int. J. Greenh. Gas Control 47, 25–37. https://doi.org/10.1016/j.ijggc.2016.01.024

Brunet, J.-P.L., Li, L., Karpyn, Z.T., Kutchko, B.G., Strazisar, B., Bromhal, G., 2013. Dynamic Evolution of Cement Composition and Transport Properties under Conditions Relevant to Geological Carbon Sequestration. Energy Fuels 27, 4208–4220. https://doi.org/10.1021/ef302023v

Burton, T., Sharpe, D., Jenkins, N., Bossanyi, E., 2001. Wind Energy Handbook. John Wiley & Sons.

Carey, J.W., Wigand, M., Chipera, S.J., WoldeGabriel, G., Pawar, R., Lichtner, P.C., Wehner, S.C., Raines, M.A., Guthrie Jr., G.D., 2007. Analysis and performance of oil well cement with 30 years of CO2 exposure from the SACROC Unit, West Texas, USA. Int. J. Greenh. Gas Control, 8th International Conference on Greenhouse Gas Control TechnologiesGHGT-8 1, 75–85. https://doi.org/10.1016/S1750-5836(06)00004-1

Carroll, S., Carey, J.W., Dzombak, D., Huerta, N.J., Li, L., Richard, T., Um, W., Walsh, S.D.C., Zhang, L., 2016. Review: Role of chemistry, mechanics, and transport on well integrity in CO_2 storage environments. Int. J. Greenh. Gas Control 49, 149–160. https://doi.org/10.1016/j.ijggc.2016.01.010

Chow, J.C., Watson, J.G., Herzog, A., Benson, S.M., Hidy, G.M., Gunter, W.D., Penkala, S.J., White, C.M., 2003. Separation and Capture of CO_2 from Large Stationary Sources and Sequestration in Geological Formations. J. Air Waste Manag. Assoc. 53, 1172–1182. https://doi.org/10.1080/10473289.2003.10466274

Cunningham, A.B., Gerlach, R., Spangler, L., Mitchell, A.C., Parks, S., Phillips, A., 2011. Reducing the risk of well bore leakage of CO_2 using engineered biomineralization barriers. Energy Procedia, 10th International Conference on Greenhouse Gas Control Technologies 4, 5178–5185. https://doi.org/10.1016/j.egypro.2011.02.495

Darensbourg, D.J., 2007. Making Plastics from Carbon Dioxide: Salen Metal Complexes as Catalysts for the Production of Polycarbonates from Epoxides and CO2. Chem. Rev. 107, 2388–2410. https://doi.org/10.1021/cr068363q

DOE, 2007. Carbon Sequestration Technology and Program Plan. URL http://cepac.cheme.cmu.edu/pasi2008/slides/siirola/library/reading/2007Roadmap.pdf (accessed 12.28.16).

EPA, 2012. Geologic Sequestration of Carbon Dioxide: Underground Injection Control (UIC) Program Class VI Well Construction Guidance 58.

Fernández Bertos, M., Simons, S.J.R., Hills, C.D., Carey, P.J., 2004. A review of accelerated carbonation technology in the treatment of cement-based materials and sequestration of CO2. J. Hazard. Mater. 112, 193–205. https://doi.org/10.1016/j.jhazmat.2004.04.019

Friedmann, S.J., 2007. Geological Carbon Dioxide Sequestration. Elements 3, 179–184. https://doi.org/10.2113/gselements.3.3.179

Frumkin, H., Hess, J., Luber, G., Malilay, J., McGeehin, M., 2008. Climate Change: The Public Health Response. Am. J. Public Health 98, 435–445. https://doi.org/10.2105/AJPH.2007.119362

Herbert, E.N., Li, V.C., 2013. Self-Healing of Microcracks in Engineered Cementitious Composites (ECC) Under a Natural Environment. Materials 6, 2831–2845. https://doi.org/10.3390/ma6072831

Hou, W., Hung, W.H., Pavaskar, P., Goeppert, A., Aykol, M., Cronin, S.B., 2011. Photocatalytic Conversion of CO2 to Hydrocarbon Fuels via Plasmon-Enhanced Absorption and Metallic Interband Transitions. ACS Catal. 1, 929–936. https://doi.org/10.1021/cs2001434

Hu, B., Guild, C., Suib, S.L., 2013. Thermal, electrochemical, and photochemical conversion of CO_2 to fuels and value-added products. J. CO2 Util. 1, 18–27. https://doi.org/10.1016/j.jcou.2013.03.004

Huerta, N.J., Hesse, M.A., Bryant, S.L., Strazisar, B.R., Lopano, C., 2016. Reactive transport of CO_2-saturated water in a cement fracture: Application to wellbore leakage during geologic CO_2 storage. Int. J. Greenh. Gas Control 44, 276–289. https://doi.org/10.1016/j.ijggc.2015.02.006

IPCC, Edenhofer, O. (Eds.), 2014. Climate change 2014: mitigation of climate change: Working Group III contribution to the Fifth Assessment Report of the Intergovernmental Panel on Climate Change. Cambridge University Press, New York, NY.

IPCC, Metz, B. (Eds.), 2005. IPCC special report on carbon dioxide capture and storage. Cambridge University Press, for the Intergovernmental Panel on Climate Change, Cambridge.

Jaramillo, P., Griffin, W.M., Matthews, H.S., 2007. Comparative Life-Cycle Air Emissions of Coal, Domestic Natural Gas, LNG, and SNG for Electricity Generation. Environ. Sci. Technol. 41, 6290–6296. https://doi.org/10.1021/es063031o

Johnson, J.W., Nitao, J.J., Knauss, K.G., 2004. Reactive transport modelling of CO_2 storage in saline aquifers to elucidate fundamental processes, trapping mechanisms, and sequestration partitioning. Geol. Storage Carbon Dioxide. https://doi.org/10.1144/GSL.SP.2004.233.01.08

Kan, L.-L., Shi, H.-S., Sakulich, A.R., Li, V.C., 2010. Self-Healing Characterization of Engineered Cementitious Composite Materials. ACI Mater. J. 107, 617–624.

Kawabata, Y., Kato, E., Iwanami, M., 2012. Enhanced Long-Term Resistance of Concrete with Marine Sessile Organisms to Chloride Ion Penetration [WWW Document]. URL https://www.jstage.jst.go.jp/article/jact/10/4/10_4_151/_article (accessed 7.30.17).

Koide, H., Tazaki, Y., Noguchi, Y., Nakayama, S., Iijima, M., Ito, K., Shindo, Y., 1992. Subterranean containment and long-term storage of carbon dioxide in unused aquifers and in depleted natural gas reservoirs. Energy Convers. Manag., Proceedings of the First International Conference on Carbon Doxide Removal 33, 619–626. https://doi.org/10.1016/0196-8904(92)90064-4

Kutchko, B.G., Strazisar, B.R., Dzombak, D.A., Lowry, G.V., Thaulow, N., 2007. Degradation of Well Cement by CO_2 under Geologic Sequestration Conditions. Environ. Sci. Technol. 41, 4787–4792. https://doi.org/10.1021/es062828c

Kutchko, B.G., Strazisar, B.R., Hawthorne, S.B., Lopano, C.L., Miller, D.J., Hakala, J.A., Guthrie, G.D., 2011. H_2S–CO_2 reaction with hydrated Class H well cement: Acid-gas injection and CO_2 Co-sequestration. Int. J. Greenh. Gas Control 5, 880–888. https://doi.org/10.1016/j.ijggc.2011.02.008

Kutchko, B.G., Strazisar, B.R., Huerta, N., Lowry, G.V., Dzombak, D.A., Thaulow, N., 2009. CO_2 Reaction with Hydrated Class H Well Cement under Geologic Sequestration Conditions: Effects of Flyash Admixtures. Environ. Sci. Technol. 43, 3947–3952. https://doi.org/10.1021/es803007e

Kutchko, B.G., Strazisar, B.R., Lowry, G.V., Dzombak, D.A., Thaulow, N., 2008. Rate of CO_2 Attack on Hydrated Class H Well Cement under Geologic Sequestration Conditions. Environ. Sci. Technol. 42, 6237–6242. https://doi.org/10.1021/es800049r

Le Gallo, Y., Couillens, P., Manai, T., 2002. CO_2 Sequestration in Depleted Oil or Gas Reservoirs. Presented at the SPE International Conference on Health, Safety and Environment in Oil and Gas Exploration and Production, Society of Petroleum Engineers. https://doi.org/10.2118/74104-MS

Li, Q., Lim, Y.M., Flores, K.M., Kranjc, K., Jun, Y.-S., 2015a. Chemical Reactions of Portland Cement with Aqueous CO_2 and Their Impacts on Cement's Mechanical Properties under Geologic CO_2 Sequestration Conditions. Environ. Sci. Technol. 49, 6335–6343. https://doi.org/10.1021/es5063488

Li, Q., Lim, Y.M., Flores, K.M., Kranjc, K., Jun, Y.-S., 2015b. Chemical Reactions of Portland Cement with Aqueous CO_2 and Their Impacts on Cement's Mechanical Properties under Geologic CO_2 Sequestration Conditions. Env. Sci Technol 49, 6335–6343. https://doi.org/10.1021/es5063488

Li, V., Wu, C., Wang, S., Ogawa, A., Saito, T., 2002. Interface Tailoring for Strain-Hardening Polyvinyl Alcohol-Engineered Cementitious Composite (PVA-ECC). ACI Mater. J. 99. https://doi.org/10.14359/12325

Li, V.C., 2003. On engineered cementitious composites (ECC). J. Adv. Concr. Technol. 1, 215–230.

Li, V.C., 2002. Large volume, high-performance applications of fibers in civil engineering. J. Appl. Polym. Sci. 83, 660–686.

Li, V.C., Yang, E.-H., 2007. Self healing in concrete materials, in: Self Healing Materials. Springer, pp. 161–193.

Li, Z., Dong, M., Li, S., Huang, S., 2006. CO_2 sequestration in depleted oil and gas reservoirs—caprock characterization and storage capacity. Energy Convers. Manag. 47, 1372–1382. https://doi.org/10.1016/j.enconman.2005.08.023

Lim, M., Han, G.-C., Ahn, J.-W., You, K.-S., 2010. Environmental Remediation and Conversion of Carbon Dioxide (CO_2) into Useful Green Products by Accelerated Carbonation Technology. Int. J. Environ. Res. Public. Health 7, 203–228. https://doi.org/10.3390/ijerph7010203

Liteanu, E., Spiers, C.J., 2011. Fracture healing and transport properties of wellbore cement in the presence of supercritical CO_2. Chem. Geol. 281, 195–210. https://doi.org/10.1016/j.chemgeo.2010.12.008

Mason, H.E., Du Frane, W.L., Walsh, S.D.C., Dai, Z., Charnvanichborikarn, S., Carroll, S.A., 2013. Chemical and Mechanical Properties of Wellbore Cement Altered by CO_2-Rich Brine Using a Multianalytical Approach. Environ. Sci. Technol. 47, 1745–1752. https://doi.org/10.1021/es3039906

McGrail, B.P., Schaef, H.T., Ho, A.M., Chien, Y. -j., Dooley, J.J., Davidson, C.L., 2006. Potential for carbon dioxide sequestration in flood basalts. J Geophys Res 111. https://doi.org/10.1029/2005JB004169

Menefee, A.H., Li, P., Giammar, D.E., Ellis, B.R., 2017. Roles of Transport Limitations and Mineral Heterogeneity in Carbonation of Fractured Basalts. Environ. Sci. Technol. 51, 9352–9362. https://doi.org/10.1021/acs.est.7b00326

Metcalf, G.E., 2009. Designing a Carbon Tax to Reduce U.S. Greenhouse Gas Emissions. Rev. Environ. Econ. Policy 3, 63–83. https://doi.org/10.1093/reep/ren015

Michaux, M., Nelson, E.B., Vidick, B., 1990. 2 Chemistry and Characterization of Portland Cement, in: Nelson, E.B. (Ed.), Developments in Petroleum Science, Well Cementing. Elsevier, pp. 2–1. https://doi.org/10.1016/S0376-7361(09)70300-0

Mirza, M.M.Q., 2003. Climate change and extreme weather events: can developing countries adapt? Clim. Policy 3, 233–248. https://doi.org/10.3763/cpol.2003.0330

Nelson, E.B., 1990. Well Cementing. Newnes.

Nordbotten, J.M., Celia, M.A., Bachu, S., 2005. Injection and Storage of CO2 in Deep Saline Aquifers: Analytical Solution for CO_2 Plume Evolution During Injection. Transp. Porous Media 58, 339–360. https://doi.org/10.1007/s11242-004-0670-9

Reeves, S.R., 2001. Geological Sequestration of CO_2 in Deep, Unmineable Coalbeds: An Integrated Research and Commerical-Scale Field Demonstration Project. Presented at the SPE Annual Technical Conference and Exhibition, Society of Petroleum Engineers. https://doi.org/10.2118/71749-MS

Shao, Y., Mirza, M.S., Wu, X., 2006. CO_2 sequestration using calcium-silicate concrete. Can. J. Civ. Eng. 33, 776–784. https://doi.org/10.1139/l05-105

Shi, J.Q., Durucan, S., 2005. CO_2 Storage in Deep Unminable Coal Seams. Oil Gas Sci. Technol. 60, 547–558. https://doi.org/10.2516/ogst:2005037

Sims, R.E.H., Rogner, H.-H., Gregory, K., 2003. Carbon emission and mitigation cost comparisons between fossil fuel, nuclear and renewable energy resources for electricity generation. Energy Policy 31, 1315–1326. https://doi.org/10.1016/S0301-4215(02)00192-1

Turconi, R., Boldrin, A., Astrup, T., 2013. Life cycle assessment (LCA) of electricity generation technologies: Overview, comparability and limitations. Renew. Sustain. Energy Rev. 28, 555–565. https://doi.org/10.1016/j.rser.2013.08.013

Varghese, O.K., Paulose, M., LaTempa, T.J., Grimes, C.A., 2009. High-Rate Solar Photocatalytic Conversion of CO_2 and Water Vapor to Hydrocarbon Fuels. Nano Lett. 9, 731–737. https://doi.org/10.1021/nl803258p

Walsh, S.D.C., Frane, W.L.D., Mason, H.E., Carroll, S.A., 2013. Permeability of Wellbore-Cement Fractures Following Degradation by Carbonated Brine. Rock Mech. Rock Eng. 46, 455–464. https://doi.org/10.1007/s00603-012-0336-9

Watson, T.L., Bachu, S., 2009. Evaluation of the Potential for Gas and CO_2 Leakage Along Wellbores. SPE Drill. Complet. 24, 115–126. https://doi.org/10.2118/106817-PA

World Nuclear Association (WNA), 2011. Comparison of Lifecycle Greenhouse Gas Emissions of Various Electricity Generation Sources.

Xiong, W., Wells, R.K., Menefee, A.H., Skemer, P., Ellis, B.R., Giammar, D.E., 2017. CO_2 mineral trapping in fractured basalt. Int. J. Greenh. Gas Control 66, 204–217. https://doi.org/10.1016/j.ijggc.2017.10.003

Yang, L., Steefel, C.I., Bechtel, H., 2013. Microfluidic and capillary tube experimental study of forsterite carbonation by CO_2 bearing fluids. AGU Fall Meet. Abstr. 41.

CHAPTER 2

Physical and Chemical Alterations in Engineered Cementitious Composite Under Geologic CO_2 Storage Conditions

[*]Reprinted from: Jubilee T. Adeoye, Cameron Beversluis, Alessandra Murphy, Victor C. Li, and Brian R. Ellis, Physical and chemical alterations in engineered cementitious composite under geologic CO_2 storage conditions, International Journal of Greenhouse Gas Control, 2019, https://doi.org/10.1016/j.ijggc.2019.01.025.

2.1 Introduction

Wellbore cement sheaths have been identified as potential leakage pathways for CO_2 from reservoirs utilized for geologic carbon sequestration (GCS) (Bachu and Celia, 2009)**,** and such leakage risks continue to be a major challenge for the long-term success of GCS as a carbon mitigation strategy. According to the U.S. Department of Energy, GCS operations must achieve a storage efficiency of 99% to be an effective technology for mitigating the increase in atmospheric concentration of CO_2 (Chow et al., 2003; Deel, 2007). Portland cement, which is the base material for wellbore cementing, consists of tricalcium silicate ($3CaO{\cdot}SiO_2$), dicalcium silicate ($2CaO{\cdot}SiO$), tricalcium aluminate ($3CaO{\cdot}Al_2O_3$), and calcium alumino ferrite ($4CaO{\cdot}Al_2O_3{\cdot}Fe_2O_3$) (Li et al., 2015; Michaux et al., 1990). While the proportion of the various constituents of Portland cement may vary, fully hydrated cement consists of approximately 70% calcium-silicate hydrates (C−S−H), which is the primary binder in hardened cement, and 20% portlandite ($Ca(OH)_2$), respectively. Numerous studies have been carried out to understand the interaction of hydrated Portland cement with CO_2 under GCS conditions. These studies have found

that distinct reaction zones develop along the exterior of reacted cement specimens following prolonged contact with CO_2-acidified water at typical reservoir temperature and pressure conditions (Bruckdorfer, 1986; Duguid and Scherer, 2010; Fernández Bertos et al., 2004; Kutchko et al., 2008, 2007; Q. Li et al., 2015). The outer zone in direct contact with CO_2-acidified water is altered extensively and is highly porous, with an abundance of amorphous silica relative to that of the unaltered cement (Kutchko et al., 2009; Kutchko et al., 2007). Next to this outer degraded zone is a region where calcium carbonate precipitates, resulting in reduced porosity and permeability, and an increase in compressive strength compared to the unaltered cement. The reduction in porosity and permeability due to the precipitation of calcium carbonate inhibits the diffusion of CO_2 further into the cement specimens (Bruckdorfer, 1986; Fernández Bertos et al., 2004; Neves Junior et al., 2013). The third zone is characterized by increased porosity and depletion of calcium (Kutchko et al., 2007). The governing chemical reactions and CO_2 transport limitations in these altered zones are presented in Kutchko et al. (2007) and Li et al. (2015). Such alteration of Portland cement has been found to lead to significant deterioration of the mechanical properties of the material (Kutchko et al., 2007; Q. Li et al., 2015; Mason et al., 2013) including reaction-induced fractures that may serve as leakage pathways for sequestered CO_2.

Although poor-quality well completion and abandonment techniques in legacy oil and gas wells make prevention of CO_2 leakage along wellbores challenging (Carroll et al., 2016; Watson and Bachu, 2009), ensuring the long-term integrity of injection wells drilled for GCS is also a crucial step toward achieving GCS storage security. Prior wellbore integrity studies have helped to develop predictive tools for assessing long-term wellbore integrity that reduce the uncertainties for leakage risk related to the mechanisms governing the alteration of conventional wellbore cementing materials under GCS conditions (Brunet et al., 2016; Carroll et al., 2016; Huerta et al.,

2016; Walsh et al., 2013), but there is still a need for innovative solutions to prevent wellbore CO_2 leakage.

Several studies have reported the incorporation of additives such as fibers, micro ribbons, and elastomers into cement slurry to improve the mechanical properties of wellbore cement and promote self-healing of fractured cement sheaths under various reservoir conditions during fossil fuel and geothermal energy extraction (Carter et al., 1968; Cavanagh et al., 2007; Dean and Torres, 2002; Morris et al., 2003; Reddy et al., 2010; Yao and Hua, 2007). Morris et al. (2003), Dean and Torres (2002), and Carter et al. (1968) reported the use of synthetic fibers to enhance the toughness of hardened cement and prevent brittle failure during downhole perforation. Reddy et al. (2010) developed a self-healing cement adopting low viscosity elastomers that promote self-healing independent of contact with reservoir fluid. Engelke et al. (2017) reported the use of a slurry that incorporates CO_2-swellable particles to promote self-healing in wells exposed to CO_2-rich environments, while Barlet-Gouédard et al. (2006) reported the testing of a CO_2 resistant cement for application under GCS conditions. Although several of these cement compositions have been successfully adopted to promote self-healing or improve the tensile properties of the cement in the hardened state, these materials may not exhibit strain hardening under tension that is needed to prevent the formation of brittle fractures during GCS where stresses from temperature swings, cyclic CO_2 injection, and volume expansion from secondary carbonation of the cementitious material are expected to occur downhole. Given that GCS wells need to serve as long-lasting barriers for stored CO_2, novel engineered wellbore cementing materials that can withstand such stresses in the downhole region, self-heal when fractures occur, and weather chemical attack from CO_2-acidified solutions without compromising their long-term mechanical integrity need to be developed.

Engineered cementitious composites (ECC) are a novel ultra-ductile fiber-based cementitious material also referred to as bendable concrete (Herbert and Li, 2013; Kawabata et al., 2012; Li, 2009, 2003) with unique tensile properties. **Figure 2.1** shows the tensile stress vs. strain curves and material failure mechanisms for conventional cement and ECC, respectively, under tensile and flexural stress. In contrast to conventional wellbore cements that exhibit brittle failure under tensile and flexural stress (**Figure 2.1a**), ECC behaves like a ductile material and has a tensile strain capacity of 2–5%, which is about 200–500 times larger than that of conventional Portland cement and fiber reinforced concrete. Under tensile stress, ECC undergoes a strain hardening stage (**Figure 2.1b**) during which several microcracks, with crack width below 60 μm, are formed (Kan et al., 2010; Li, 2009). Such tight crack width has been shown to promote effective self-healing (Herbert and Li, 2013; Kan et al., 2010; Li, 2009). The most studied ECC contains polyvinyl alcohol (PVA) fibers that impart reinforcement to the cementitious material and promote the self-healing of cracks by serving as nucleation sites for healing products such as calcium carbonate (Li and Yang, 2007)**.**

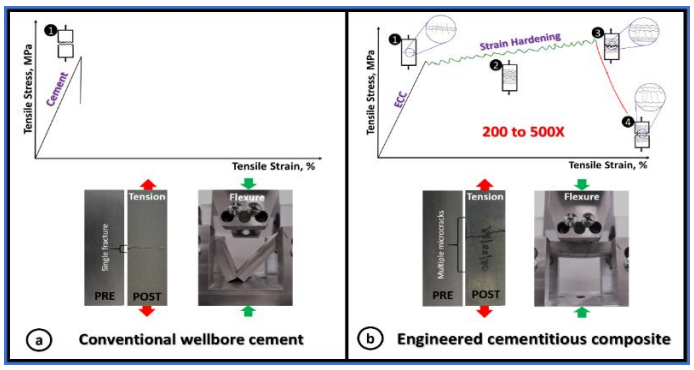

Figure 2.1: Tensile stress vs. strain curves for **(a)** conventional cement and **(b)** ECC. Inserts in the Figure show the failure mechanisms for both conventional cement and ECC under tension and flexural stress, respectively. For conventional cement and ECC, "1" represents the first crack point under the stress-strain curves which corresponds to the failure point for conventional cement. "2" is the strain hardening stage during which multiple micro-cracks are generated in ECC. Point "3" represents crack localization and "4" is the failure point.

When exposed to CO_2 and water under atmospheric conditions, ECC microcracks undergo autogenous self-healing which is a desirable property in wellbore cement where the integrity of the cement matrix is crucial (Herbert and Li, 2013; Y. Yang et al., 2009). These beneficial properties (strain-hardening, autogenously controlled tight crack width, and self-healing ability) make ECC a prime candidate for consideration as a leak-proof wellbore cementing material. Additionally, because ECC is a cement-based composite, with similar preparation procedures as conventional wellbore cement, it could serve as a substitute cementing material that requires minimal modification to current cementing machinery making it a potentially attractive alternative to operators. It is therefore important to understand the nature of the alterations in ECC following chemical attack under GCS conditions to assess its suitability as a substitute wellbore cementing material over conventional Portland cement.

This study was undertaken to evaluate the alteration of ECC chemical and mechanical properties after contact with CO_2-acidified water under GCS reservoir conditions. A combination of static batch and flow-through experiments were carried out to investigate the alteration in ECC under diffusive and advective mass transport conditions, respectively. The changes in the microstructure of the composite were characterized to predict the long-term integrity of ECC. Although the rheological properties, such as plastic viscosity and yield stress, of the conventional ECC used in this study are not yet optimized for wellbore cementing operations, the objective of this research is to gain an initial understanding of the unique interactions between ECC and CO_2-rich fluids under GCS conditions and evaluate the impact of such interactions on its microstructural and micromechanical properties.

2.2 Material and methods

2.2.1 ECC raw materials and design considerations

The ECC used in this study is the standard M45 mix with proportions optimized for multiple microcracking during strain hardening up to strain capacity of 5% (Li, 2009) while maintaining a crack width of 60μm or less. The mix proportions of the materials by weight of the binder are presented in **Table 2.1**. The cement used is Type I Portland cement, similar to Class A wellbore cement, intended for cementing from the surface to 6,000 ft in environments where special properties are not required. Class F fly ash, the most common pozzolanic admixture in oil well cement slurries (Nelson et al., 1990), was added to the mix to enhance its flowability, improve the tensile strain capacity, and reduce the crack width during the strain hardening stage. Fly ash improves the ductility of ECC because of its ability to enhance the interfacial friction bond between the fiber and the matrix through densification of the fiber/matrix interface (W. Li et al., 2015; Yang et al., 2009, 2007). In the absence of fly ash, conventional cement with microfiber admixture may not exhibit the desired tight crack width and strain hardening behaviors under tension. The silica sand is finely graded with an average particle size of 110 μm, which is similar to silica sand added to cement slurries designed for downhole environments where low permeability and high compressive strength are required (Le Saoût et al., 2006; Nelson et al., 1990). Although finely graded sand is added to ensure volume stability in the design of standard M45 mix used in this study, the mix composition of ECC can be re-engineered, excluding sand, without compromising its inherent strain hardening capacity. REC15 polyvinyl alcohol (PVA) fibers (Kuraray, Japan) with average diameter of 39 μm and length of 12 mm were added to the mix at 2% volume of slurry. The fibers were surface-coated with a proprietary hydrophobic oiling agent (1.2% by weight) to reduce the fiber/matrix interfacial bonding. To improve the workability of the mixture

in the fresh state, a polycarboxylate superplasticizer (SP) was added. Further design considerations for standard M45 ECC are presented in Li (2009).

Table 2.1: Design proportions by weight for standard ECC-M45. Solid component and water fractions are presented as fractions of the cement weight.

	Cement	**Fly ash**	**Sand**	**SP**	**Water**	**Fiber vol. (%)**
Proportion by weight of cement	1	1.2	0.8	0.012	0.56	2

2.2.2 Sample preparation

The fresh slurry was cast in 2-inch cubic molds, de-molded after 24 hours, and cured in plastic bags at 23±3ºC for 28 days. Several 1-inch and 0.5-inch diameter cylindrical cores were subsequently made from the ECC cubes using a water-cooled core drill similar to the approach used in previous wellbore cement studies (Barlet-Gouédard et al., 2009, 2007, 2006; Rimmelé et al., 2008). The cores were then wrapped in paper towels to expel the surficial water prior to the start of the experiment. A 0.5-inch core was sliced into two half-cylinder sections using a precision saw with a diamond blade (Isomet) and the surface of one half-cylinder was roughened using 60-grit sandpaper to serve as a fluid-flow pathway for the flow-through studies.

2.3 Experimental procedure

2.3.1 Static batch study

Six 1-inch ECC cores were oriented lengthwise in a 600-mL stainless steel batch reactor (Parr Instrument) and stacked in a grid as shown in **Figure 2.2.** The cores were separated using thin boat-shaped teflon strips to maximize direct exposure of the samples to the CO_2-saturated water. 490 mL of deionized (DI) water with a resistivity greater than 18.2 MΩ-cm was added to the reactor at the beginning of the experiment, resulting in a solid to water ratio of approximately 1:6.

The solid to water ratio was constrained by the volume of the reactor and the need to ensure that the cores were fully submerged during the experiment.

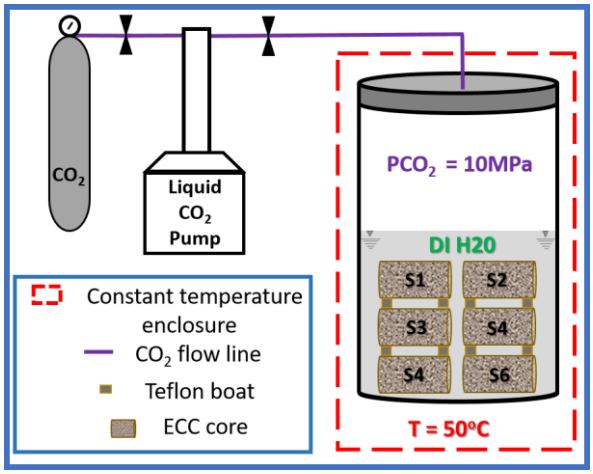

Figure 2.2: Experimental setup for the static-batch study. Cores were separated using boat-shaped teflon strips to maximize direct exposure of the samples to the CO_2-saturated water.

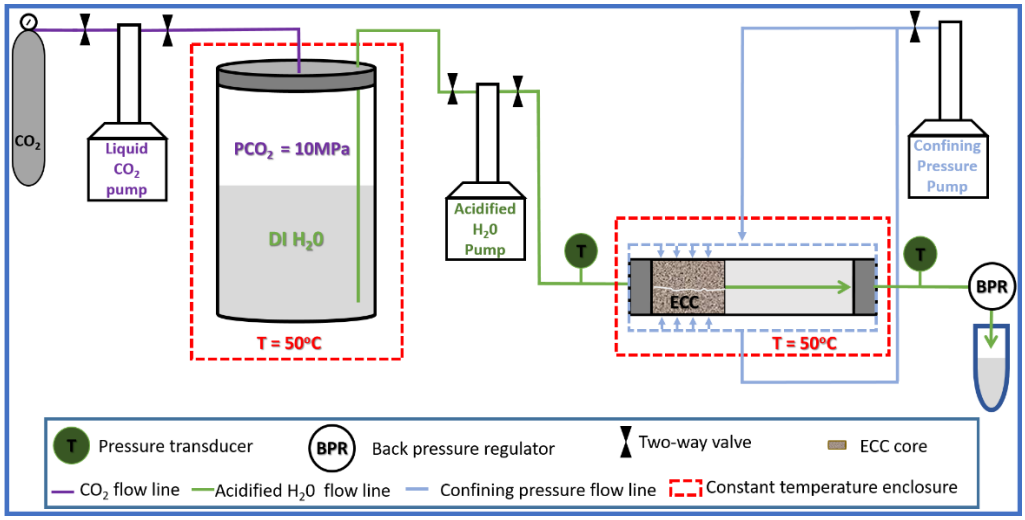

Figure 2.3: Experimental setup of the flow-through study. Purple, green, and blue flow lines represent the CO_2, acidified water, and confining fluid streams, respectively.

Given the relatively small volume of water, it is likely that the buildup of Ca^{2+} in the reactor may have slowed the rate of calcium leaching over time (Matteo et al., 2018; Matteo and Scherer, 2012). A syringe pump (500D, Teledyne Isco) was used to maintain a constant headspace CO_2

pressure (P_{CO2}) of 10 MPa and a temperature of 50±1°C was maintained via a heating jacket and a temperature regulator (Briskheat). This temperature and pressure condition was chosen in accordance with typical GCS conditions and an approximate storage depth of 1 km (Bachu, 2000; Barlet-Gouédard et al., 2006; McGrail et al., 2006; Schaef and McGrail, 2009). Samples were removed from the batch reactor after 2, 9, 16, 23, 30, and 44 days of exposure to the CO_2-saturated water. For each sample retrieval, the temperature in the vessel was decreased to 35^oC after which the CO_2 pressure in the headspace was slowly reduced to atmospheric conditions over 90 minutes, and 82 mL of water was removed from the batch reactor to maintain a constant solid to water ratio in the reactor. Subsequently, the pressure and temperature conditions in the reactor were restored as detailed above. Each retrieved sample was dried in an oven at 50^oC for 24 hours followed by a second round of drying during which the temperature was elevated to 80^oC to expel the water from the cement pores.

Although GCS reservoirs will typically be highly saline, DI water was used in this work to simplify the parameter space for studying fundamental interactions of ECC with CO_2 and water under GCS temperature and pressure conditions. This approach, which has also been adopted in previous wellbore integrity studies such as those by Rimmelé et al. (2008) and Huerta et al. (2016), is reasonable as the major impact of salinity on the reaction process is limited to its effect on the extent of CO_2 solubility, the pH of the initial system, and the activity of the aqueous species (Duan and Sun, 2003; Spycher and Pruess, 2005). In a study carried out by Barlet-Gouédard et al. (2009) on Portland cement, the alteration pattern characterized by a series of carbonation and dissolution fronts was similar for the test performed with pure water and that with 4 M NaCl brines. However, the extent of alteration observed in the system with pure water was 10 times greater than in the system with saline water due to faster reaction kinetics at lower pH (Barlet-Gouédard et al., 2009).

By carrying out this study using DI water, we have evaluated the composite under the most extreme initial reactive environment at the given experimental pressure and temperature conditions.

2.3.2 Flow-through study

To investigate the alteration of ECC under advective-flow conditions such as may occur due to the generation of cracks during CO_2 injection, a flow-through experiment was conducted using a tri-axial core-flooding cell (Core Laboratories; **Figure 2.3**). DI water was saturated with CO_2 in a 600-mL stainless steel batch reactor at a P_{CO2} of 10 MPa and a temperature of 50°C. The CO_2-acidified solution was then injected through the fractured core at a constant rate of 1 mL/h. Discrete effluent samples aggregated over 2-hour periods were collected at various intervals for 192 hours.

A backpressure regulator was installed downstream of the core and set at a pressure of approximately 10.4 MPa to prevent degassing of the CO_2 during flow. The differential pressure in the system was monitored over the duration of the experiment using pressure transducers installed in the upstream and downstream sections of the reactor flow line. Changes in the pressure gradient were used to infer permeability evolution along the fracture according to the cubic law for the flow of an incompressible fluid between two parallel smooth plates (Zimmerman and Bodvarsson, 1996).

2.3.3 Characterization of aqueous chemistry and reaction products

Post-reaction aqueous samples from the batch reactor and effluent samples from the flow-through experiment were obtained and pH was estimated based on charge balance calculations. Cation analysis (Ca, Mg, Fe, Si, Na, K, and Al) was carried out via inductively coupled plasma mass spectrometry (ICPMS; 7900 Agilent Technologies, CA) on samples acidified with HNO_3 to a pH < 2, while anion analysis was done using ion chromatography (Agilent Technologies, CA).

CO_2 solubility under each experimental condition was calculated using the thermodynamic model presented by Duan and Sun (2003) and equilibrium constants were adjusted to account for the system temperature (50^{o}C) and pressure (10 MPa) conditions using SUPCRT92 with the DPRONS92 database (Johnson et al., 1992). The activity coefficients of the aqueous species were estimated using the Davies equation, and the pH of the solution at each sampling point was calculated based on the measured cations and anions concentrations within the constraint of electroneutrality. Secondary mineral phases in the reacted samples were characterized using Raman spectroscopy (Renishaw inVia microscope) with a 532-nm laser, and the mineral species were identified using the RRUFF database (Armbruster and Danisi, 2015; Lafuente et al., 2015).

2.3.4 X-ray computed tomography (XCT)

The extent of mineral precipitation in the pores and along the PVA fibers following CO_2-ECC reactions was determined by comparing pre- and post-reaction XCT scans (XTH225, Nikon Metrology, Inc.) of the cores from the batch experiment. The scans used a beam energy of 140 KV and current of 115 μA. 3141 projections were taken at steps of 0.11° with a 4-frame integration per projection. The data was reconstructed using CT Pro (XT5.1.3, NikonMetrology, Inc), and ImageJ (National Institutes of Health, Bethesda, Maryland) was used for image analysis.

2.3.5 Scanning electron microscopy (SEM) and optical microscopy

150 μm petrographic thin sections were made from each reacted sample and a scanning electron microscope (JEOL 7800-FLV) equipped with a backscatter electron (BSE) detector was used to obtain grayscale images of the reacted samples. Changes in the grayscale intensities and textures of the different alteration zones in the BSE images were used to infer the extent of alteration of ECC following reaction with CO_2-acidified water. Energy dispersive spectroscopy (EDS) elemental maps were collected to evaluate changes in the elemental composition of the

altered ECC material. Optical images of the petrographic thin sections were also obtained using an optical microscope (Scienscope) and a Sobel edge-detection filter (Kanopoulos et al., 1988) was used to determine the penetration depth of the reaction front.

2.3.6 Microhardness

Vickers microhardness (HV) analysis was carried out on the reacted and unreacted ECC samples to infer the change in the mechanical strength of ECC following CO_2 reaction. Samples were dry-polished using a series of finer sandpaper grit sizes, with a final polish using 4000-grit sandpaper. To capture the evolution of microhardness from the altered zone to the unaltered region, the polished sample surfaces were divided into multiple sections from the edge to the center of the core as shown in **Figure 2.4a**. The first two millimeters in the altered zone were divided into four 0.5-mm sections while the last eleven millimeters were divided into 1-mm, 2-mm, and 8-mm sections, respectively. This was done to obtain higher resolution measurements in the altered region. Seven representative indents were made on the surface of the polished cementitious material in each zone with a Vickers microhardness probe (LECO LM2) using a 500-g load and a dwell time of 15 s (Kutchko et al., 2007; Zhang et al., 2013). Given the heterogeneity of the ECC samples and the presence of the large sand grains in the material, indents were made only on the

cementitious material and the areal extents of the indents were converted to HV values using the **Eq. 2.1**:

$$\mathrm{HV} = \frac{1854.4\mathrm{F}}{\mathrm{d}^2} \qquad \textbf{Eq. 2. 1}$$

Where d (μm) represents the average length of the diagonal impressions of the indenter and F (g) is the load applied (Dieter and Bacon, 1986) (**Figure 2.4b**). The average of the seven hardness values was then used to infer the overall hardness in each zone.

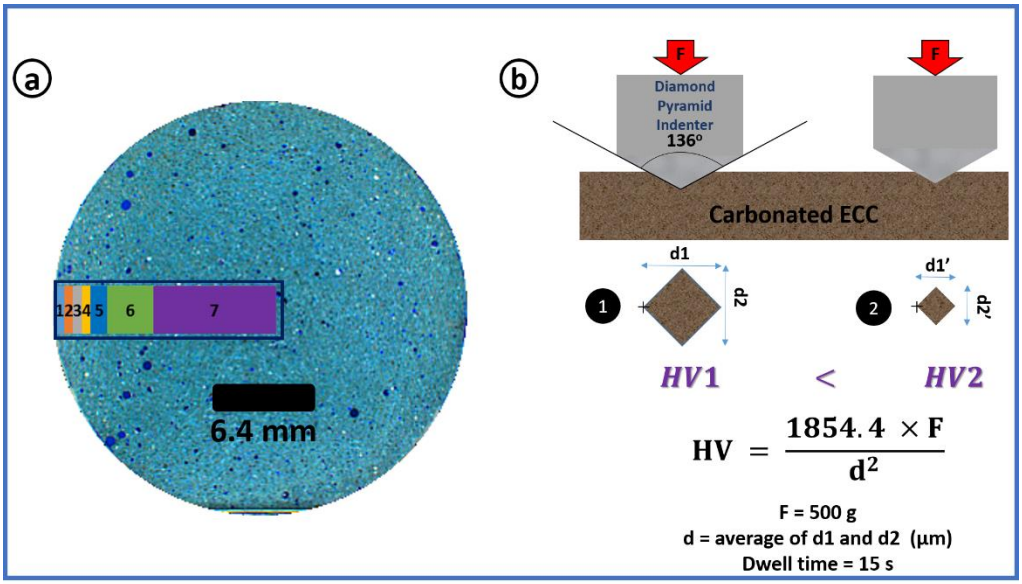

Figure 2.4: (a) Optical image of the thin section of an unreacted sample. Colored boxes represent the pre-defined sections for micro hardness analysis. Sections 1 – 4 are 0.5 mm wide while sections 5, 6, and 7 are 1 mm, 2 mm, and 8 mm wide respectively. **(b)** Model and mathematical correlation for calculating HV of a carbonated sample. Indent 2 is on a more carbonated region than indent 1. Hence, it has a higher HV.

2.4 Results and Discussion

2.4.1 Physical characteristics and extent of alteration

In the static batch study, the pH of the CO_2-saturated water remained acidic (4.5 to 4.8) throughout the course of the experiment (see **Appendix A; Section A.1 and Appendix Figure A.1** for aqueous chemistry and pH evolution). Following the reaction of the cores with the CO_2-rich water, a distinct orange coloration developed on the exterior of all the samples. This is consistent with prior studies that exposed cement to CO_2-acidified fluids (Carey, 2013; Duguid and Scherer, 2010; Kutchko et al., 2008; Kutchko et al., 2007; Li et al., 2015). Optical images of petrographic thin sections of the cores revealed an increase in the depth of the orange altered zone with the duration of exposure (**Figure 2.5 a)**. Previous attempts to characterize the chemical composition of this orange-colored alteration zone suggest the presence of non-crystalline Fe(III) hydroxides (Carey,

2013; Q. Li et al., 2015). In this study, EDS maps of the altered zone indicated no variation in the relative abundance of Fe along this zone as a function of distance from the edge of the core. While the exact mineral reaction products within this altered region are not known, similar orange coloration has also been observed in cement following hydrochloric acid attack (Huerta et al., 2009) and can be used to infer the extent of penetration of acidic fluids following the interaction of ECC with CO_2-acidified solution.

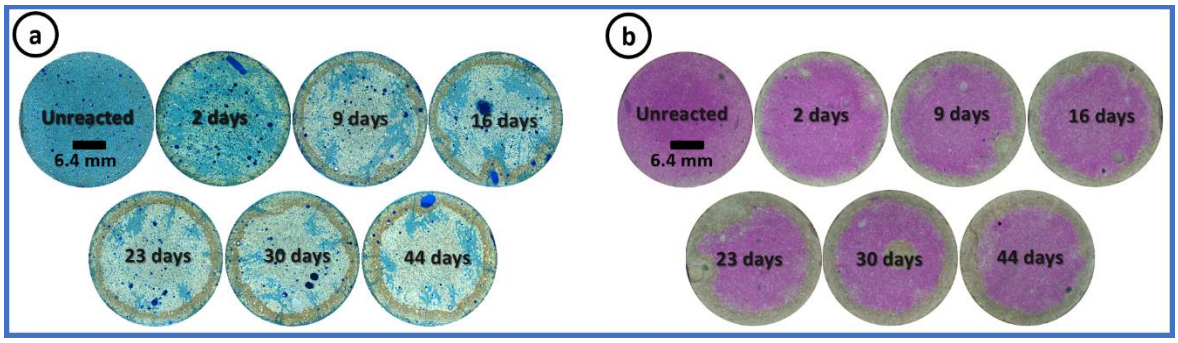

Figure 2.5: (a). Optical images of thin sections of reacted cores showing the progression of the altered front after 2, 9, 16, 23, 40, and 44 days of reaction with CO_2-acidified solution at 50°C and 10 MPa of CO_2. The blue coloration of the sample is from blue epoxy with which the samples have been impregnated. **(b).** Optical images of cross-sections of the ECC cores stained with phenolphthalein pH indicator to reveal the extent of carbonation of the cores. The pink region of each core is the unaltered zone, while the colorless region is the carbonated zone.

Further analysis was carried out to estimate the depth of CO_2 penetration based on variations in the pH of the carbonated zone while the unaltered zone is identified by the pink coloration that occurs at pH values above 9 (Verbeck, 1958). The depth of alteration for each sample was estimated from the average of 20 measurements from the edge of the core to the leading edge of the alteration zone determined via optical image analysis of sample thin sections through the application of a Sobel edge detection filter (**see Appendix Figure A.2**) and pH variation using phenolphthalein solution. The rate of alteration was determined using a form of Fick's second law that correlates the depth of alteration under a constant concentration boundary with the square root of time (Kutchko et al., 2009, 2008; Neville, 2011) described in **Eq. 2.2**:

$$L = \propto t^{0.5} \qquad \textbf{Eq. 2. 2}$$

where L is the depth of the altered zone in mm, α is the diffusion coefficient in mm/$t^{0.5}$, and t is the duration of exposure in days. The plots of L versus square root of exposure time using both Soble edge detection and pH indicator exhibited linear correlations (R^2 = 0.98 and 0.97) with diffusion coefficients of 0.53 and 0.52 mm/$day^{0.5}$, respectively (**Figure 2.6**). Thus, the rate of alteration of ECC due to penetration of CO_2-acidified water is demonstrated to be a diffusion-controlled process, which is consistent with prior GCS wellbore cement integrity studies (Barlet-Gouédard et al., 2006; Kutchko et al., 2009; Kutchko et al., 2008). Based on these correlations and assuming that the alteration mechanism will progress similarly over periods greater than the duration of the experiment, the depth of alteration of intact ECC after 50 years of reaction with CO_2-acidified water at 50°C and 10 MPa P_{CO2} is predicted to be approximately 72 mm. In a similar study carried out by Kutchko et al., (2009) on samples with a pozzolan to cement ratio of 35:65, a total altered depth of approximately 224 mm was predicted after 50 years of exposure to CO_2-acidified water under similar temperature and pressure conditions of 50°C and 15 MPa. Although the higher P_{CO2} used in the Kutchko et al. (2009) study will decrease the system pH below that of the current study, it is unlikely that such enhanced acidity will lead to a threefold increase in the depth of alteration over the same period. Furthermore, since the pozzolanic composition of the material used by Kutchko et al. (2009) is lower than that used in this study (fly ash:cement ratio of 55:45), and since higher proportions of pozzolan have been shown to lead to faster rates of CO_2 penetration in cementitious materials (Kutchko et al., 2009; Lye et al., 2015; Zhang and Li, 2013), it is concluded that the ability of standard M45 ECC to limit the penetration of CO_2-acidified water through uncracked cementitious material under a constant P_{CO2} boundary condition is greater than that of a typical 35:65 pozzolan:cement mix used for wellbore cementation.

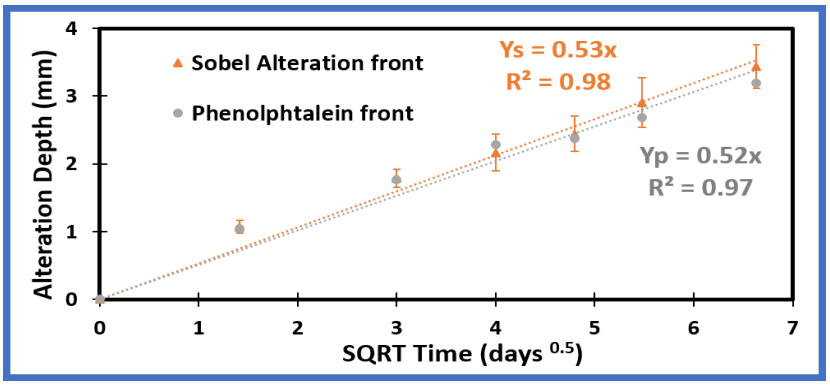

Figure 2.6: Combined plot of the alteration depth vs. SQRT time using Sobel edge detection, phenolphthalein pH indicator. Equations Ys and Yp describe CO_2 diffusion and depth of alteration in ECC as a function of time using the Sobel edge detection filter and phenolphthalein pH indicator, respectively. Error bars represent the standard deviation of 20 measurements of the altered depth from the rim of the core to the leading edge of the alteration zone. The goodness of the linear fit of the alteration depth vs. square root (SQRT) of time indicates that CO_2 transport in ECC is a diffusion-controlled process.

2.4.2 Extent of mineral carbonation

BSE images (**Figure 2.7**) of the petrographic thin sections provide further insight into the textural and microstructural changes in the reacted zone of the ECC. The pore spaces and the PVA fibers appear as the lowest grayscale intensity (black) while the sand grains and C-S-H appear as dark-gray materials distributed within the matrix. The sand grains are identifiable by their distinct grain boundaries, while the unhydrated cement phase appears as the brightest intensity (Stutzman, 2001). BSE images of the unreacted sample reveal an abundance of the unhydrated cement prior to carbonation. Following exposure to the CO_2-rich water, the abundance of the unhydrated phase in the altered zone decreased and the grainy texture in the unreacted material was converted to a smooth, more-homogeneous consistency due to the conversion of the calcium-rich cementitious materials into calcium carbonate (Kutchko et al., 2009; Kutchko et al., 2007). The presence of calcium carbonate within the pores was confirmed by Raman analysis as the spectra of the precipitates corresponded to the vibrational modes of CO_3^{2-} in calcite (**see Appendix Figure A.3**). In contrast to previous studies on neat Portland cement in which three distinct altered zones have

been found following the reaction of cement with CO_2-acidified water, only one distinct alteration zone was observed in the reacted ECC and is characterized by pores filled with secondary mineral precipitates. The absence of multiple distinct reaction zones has been reported in previous studies on fly ash-amended cement following carbonation under static batch conditions (Zhang et al., 2014) (Kutchko et al., 2009) and in sidewall cores retrieved from a well penetrating a natural CO_2 production reservoir (Crow et al., 2010). This can be attributed to lower portlandite content and pH of the matrix, in comparison to ordinary Portland cement, because of increased pozzolanic reactions in the presence of fly ash (Lye et al., 2015). Such low portlandite content will lead to lower dissolution of the matrix and mobility of OH^- and Ca^{2+} species, promoting in-place carbonation. In this study, the depth of the pore-filled region increased as the duration of CO_2 reaction increased and was comparable to the depth of the orange zone observed in the **Figure 2.5**.

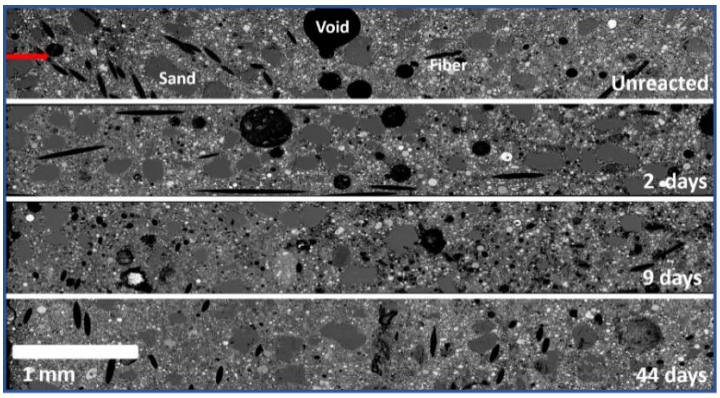

Figure 2.7: BSE image of unreacted ECC sample and reacted samples after 2, 9, and 44 days of reaction respectively. The red arrow represents the direction of the altered front from the constant concentration boundary. Pore filling and texture refinement of the parent material were observed at the edge of the core due to the carbonation of the composite.

2.4.3 The role of PVA fibers for mineral carbonation

BSE images and EDS maps of the area around the fiber of the unreacted sample (**Figure 2.8a**) reveal the presence of Ca, O, C, and Si-rich materials consistent with hydrated cement. Higher magnification of this region identifies a gap between the ECC matrix and the fibers in the unreacted

ECC sample (**Figure 2.8a insert, see Appendix Figure A.4**). This gap is referred to as the fiber/matrix interfacial transition zone (ITZ) (Sakulich and Li, 2011) and is vital for maintaining the strain-hardening property exhibited by ECC under tensile loading (Redon et al., 2001). It is promoted by the oil coating applied on the PVA fibers, which reduces the hydrophilicity of the fibers and consequently the chemical bond between the fibers and the ECC matrix. Thus, instead of rupturing under tensile load, the fibers pull out as the ITZ acts as a slipping plane, promoting ECC ductility and maintenance of tight crack width (Kan et al., 2010; Sahmaran et al., 2007; Tosun-Felekoğlu et al., 2014).

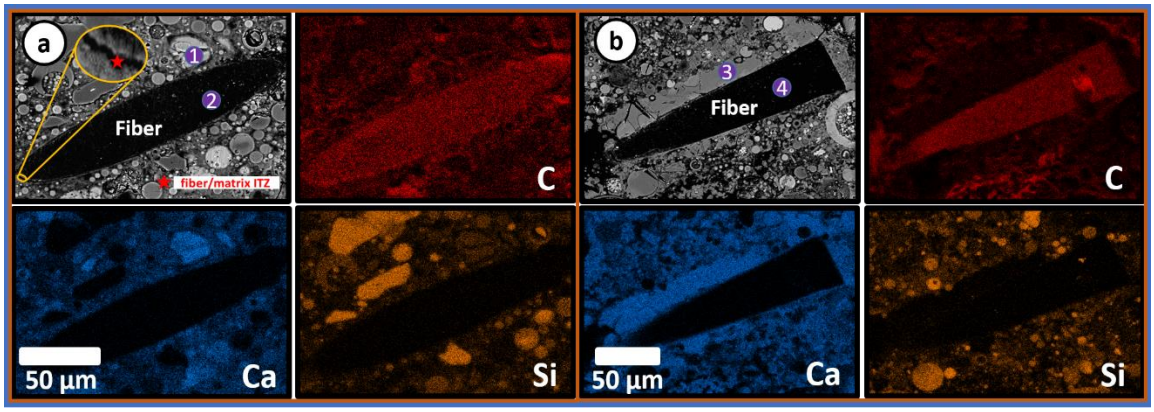

Figure 2.8: **(a)** BSE and EDS maps of the region around a fiber in an unreacted sample.EDS analysis of the area marked "1" in purple showed that the material is rich in C, Ca, Si, O, which are the primary elemental constituents of hydrated cement. The area marked "2" represents a polyvinyl alcohol (PVA) fiber. The area marked with the red star indicates the fiber/matrix interfacial transition zone (ITZ) prior to carbonation **(b)** BSE and EDS maps of the region around a fiber in a reacted sample. The area marked "3" is rich in Ca, C, and O in comparable proportion to calcite. PVA fiber is marked as "4".

Figure 2.8b shows a similar fiber after 4 weeks of contact with CO_2-acidified water where is it clear that a secondary precipitate appears to fill the gap between the fiber and the ECC matrix. EDS mapping of the region shows that the secondary material is calcium-rich, and its EDS point analysis showed a molecular weight percent ratio which is comparable to the composition of calcium carbonate ($CaCO_3$; Ca:C:O weight percent of 40:12:47). **Figure 2.9a** presents XCT scans of a section of the core before and after carbonation. In the pre-reaction scan, fibers (solid-gray)

can be seen streaking through a vug and are not covered with any material. Following six weeks of reaction, there is evidence of mineral precipitates on the PVA fibers shown in the XCT data. This suggests that in addition to improving the mechanical performance of the cementitious material under tensile loading conditions, the fibers incorporated in ECC can serve as nucleation sites for secondary mineral carbonates, thereby promoting secondary carbonation and filling of macropores within the ECC (**Figure 2.9b**). Such filling of ECC porosity will aid in reducing the permeability of the cementitious material to CO_2 and lead to improved wellbore seal integrity. Furthermore, carbonation improves the compressive strength of the cementitious material in the long-term (Bruckdorfer, 1986; Kutchko et al., 2007). In contrast to the section where fibers extend into a vug and serve as nucleation sites for carbonate precipitates, BSE images show that carbonation occurred within the matrix for sections of the fiber embedded in the matrix. Although carbonation occurred along the ITZ, the ITZ did not appear to be fully clogged by the new material as some gaps were clearly visible between the precipitates and the fiber, potentially allowing for maintenance of the positive strain-hardening property of ECC following carbonation.

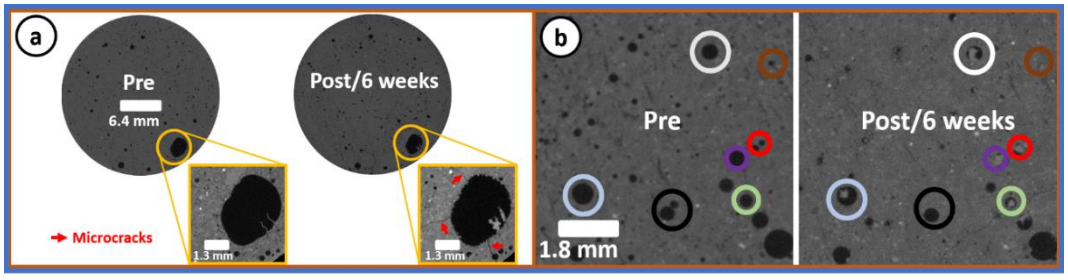

Figure 2.9: **(a)** XCT scans showing mineral carbonation in a vug with fibers acting as nucleation sites for secondary mineral precipitation. Microcracks generated in the sample are indicated by the red arrows and were measured to be < 60 μm in width. **(b)** XCT scans showing the pre and post-reaction (after 6 weeks) condition of the pores. Multiple pores have been filled with secondary calcite precipitates. Ovals surrounding the pre- and post-reaction sections of the core are color-coded similarly to aid interpretation.

2.4.4 Effect of carbonation on the mechanical strength of ECC

Figure 2.10 shows a plot of Vickers's michrohardness values (HV) for unreacted and reacted ECC samples up to 6 weeks of high P_{CO2} exposure, with error bars corresponding to the standard deviation of seven data points. For this discussion, the rim region represents the section of the core with the light orange color, i.e. 0 to 1 mm and 0 to 1.5 mm from the exposed surface for samples reacted for 2 to 16 days and 23 to 44 days, respectively, while the carbonated region represents the section of the core with the brown coloration, i.e. 1 to 2 mm and 1.5 to 3 mm for samples reacted for 2 to 16 days and 23 to 44 days, respectively. For the unreacted ECC samples, the HV was consistent in all regions tested with a mean of 35.7± 2.2 HV/500g. The mapping of the HV for ECC along the altered front following exposure to CO_2-acidified water showed a general increase in HV in comparison to the HV of unaltered ECC, and the HVs within and outside the colored zone for all reacted cores were generally higher than the HV for unreacted ECC. For samples exposed for 2 to 16 days, the highest HV was recorded between 0.5 to 2 mm from the edge of the core while for the samples reacted for 23 to 44 days, the highest HVs were measured between 1.5 to 3 mm from the edge. The region with the highest hardness value corresponds to the zone with the thick brown color and is potentially the most carbonated region. The highest HV was not observed right at the edge of the core due to the higher porosity along the outer edge of the core compared to that of the inner carbonated region. The increase in HV near the rim of the core is supported by observations from post-reaction BSE images which show extensive pore filling in the entire altered zone in comparison to materials in the unaltered zone (**Figure 2.7**). This general increase in hardness suggests that the carbonation of ECC may lead to an increase in its compressive strength (Bruckdorfer, 1986; Kutchko et al., 2007). Previous studies by Zhang et al. (2013) and Kutchko et al. (2009) on Pozzolan-amended Portland cement have also reported a general increase in HVs following reaction with CO_2-acidified solutions, with the increase in HV

attributed to precipitation of calcite in the pores. However, continuous pore refinement of the ECC matrix due to the pozzolanic activity of the fly ash under high-temperature and pressure conditions may have contributed to the increase in hardness observed in the interior of the core (Kutchko et al., 2007). The fact that some probed regions on the altered core had HVs comparable to the unreacted material can be explained by the heterogeneity of the material, the varying degree of pozzolanic activity, and the presence of isolated regions for which penetration of reactive fluid was hindered (Cao et al., 2015).

To evaluate the accuracy of the 50-year estimate of the extent of alteration derived using the edge detection approach, the limit of the carbonated zone was determined based on the point of transition from elevated hardness to the original hardness of the unaltered material. The distance from the edge of the core to this transition point when plotted as a function of the square root of time exhibits a linear trend (R^2 = 0.94) with a diffusion coefficient of 0.48 mm/day$^{0.5}$ (**see Appendix Figure A.5**). Assuming that the rate of change in the penetration depth of the carbonation front measured by changes in HV is also a diffusion-controlled process, the extent of alteration after 50 years of contact between ECC and CO_2-acidified water under GCS conditions is estimated to be 64 mm. This difference in estimation of the long-term CO_2 penetration depth in comparison to that predicted by the Sobel edge detection and phenolphthalein approaches (**Section 2.5.1**) may be due to the fact that the HV estimate is based on a single data point while the Sobel edge detection and phenolphthalein estimates are based on the mean of 20 measurements taken from the rim of the core to the alteration front. However, the HV estimate is not significantly different as it falls within the margin of statistical error of the Sobel estimate.

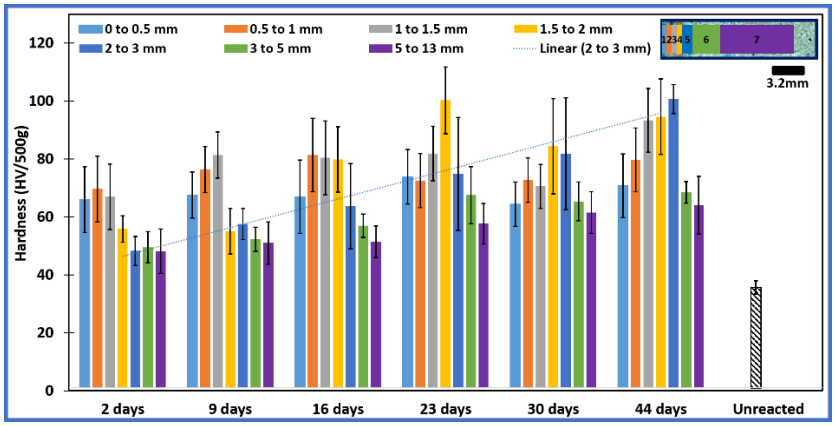

Figure 2.10: Vickers microhardness (HV) for reacted and unreacted ECC samples exposed to CO_2-acidified water for 2, 9, 16, 23, 30, and 44 days. Error bars represent the standard deviation of the HV for seven indents made in each region, as illustrated in the Figure insert. The insert on the top right corner highlights the zones defined in **Section 2.4.6.**

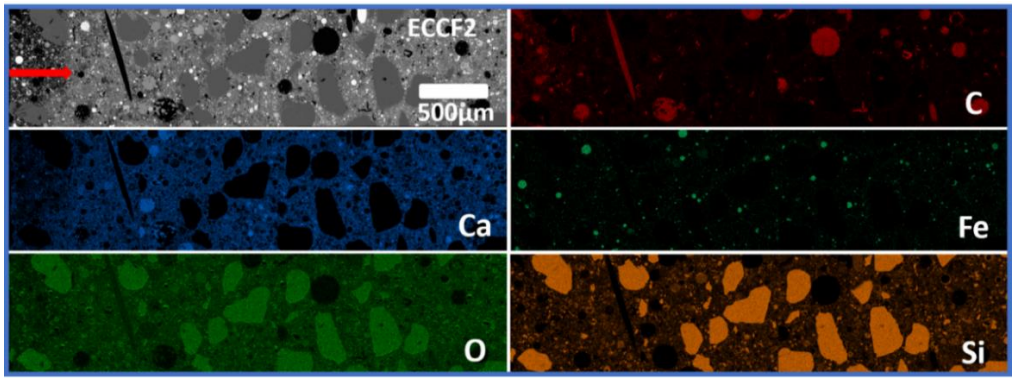

Figure 2.11: BSE image and EDS maps of the altered region in the flow-through experiment. The red arrow indicates the direction of the reaction front perpendicular to the fracture surface.

2.4.5 Development of microcracks in carbonated ECC

In contrast to previous studies on Portland cement in which fracturing and spalling have been observed following reaction with CO_2-acidified solutions (Barlet-Gouédard et al., 2006; Brandl et al., 2011; Li et al., 2015), physical examination of the ECC samples following reaction under static batch conditions showed no fracturing. However, optical images of the thin sections of the reacted samples revealed the development of microcracks at the rim of the core after 9 days of reaction (**Figure 2.5a**). The extent and occurrence of these microcracks increased with greater time of exposure to the CO_2-acidified water. While thermal stresses can lead to the generation of cracks

in cement, the fact that the cracks did not show up until later times when carbonation of the core was more extensive and were limited to the rim of the core (**Figure 2.5a**) where carbonation occurred, suggests that they were initiated by stresses from secondary mineral carbonation in the pores as the reaction progressed. Precipitation of calcium carbonate leads to the generation of stresses because calcium carbonate has a higher molar volume than the parent hydrated cement phases (Fabbri et al., 2009; Pham and Prince, 2014; Thiery et al., 2005)**.**

In this study, the crack apertures observed from BSE and XCT images were generally less than 60 µm after 6 weeks of reaction, which is comparable to the microcrack width observed in ECC undergoing strain hardening (Kan et al., 2010; Li, 2009). The self-controlled microcrack width ensures improved long-term secure storage of CO_2 relative to typical wellbore cements that undergo brittle fracturing, as **s**everal studies have shown that with tighter cracks the potential for self-healing is enhanced (Carroll et al., 2016; Huerta et al., 2016; Luquot et al., 2013).

2.4.6 Permeability evolution in flow-through study

Post reaction BSE image and EDS maps of the mid-section of the core showed erosion of the ECC into the matrix adjacent to the fracture (**Figure 2.11**). This is likely due to the low pH conditions of the influent during the flow-through experiment (pH = 3.1; **Appendix Figure A.6**), leading to greater dissolution along the fluid flow path. This contrasts with the observations of minimal ECC dissolution in the batch experiment and shows that CO_2-acidified waters may have a negative effect on the integrity of the cementing material if fracture pathways exist within the composite or along cement/casing or cement/caprock interfaces. This observation is consistent with prior work from Luquot et al. (2013) and Deremble et al. (2011) who saw and extensive dissolution of the cement matrix adjacent to the fracture during the flow of CO_2-rich water. XCT scans revealed that the pores adjacent to the eroded section of the fractured ECC core filled

extensively with secondary mineral carbonates. Over the course of 120 hours, the permeability of the fracture decreased from approximately 930 mD to 100 mD (**Figure 2.12**). Permeability reductions can result from dissolution-driven processes such as particle mobilization leading to clogging of the fracture aperture (Ellis et al., 2013) and dissolution of critical asperities leading to closure of the fracture (Brunet et al., 2016; Tsang and Witherspoon, 1981), or through precipitation-driven processes whereby secondary minerals clog the fracture pathway (Cao et al., 2015; Luquot et al., 2013). Post reaction SEM analysis of the fracture pathway revealed no evidence of mineral carbonation in the upstream section of the core, but did confirm the presence of rhombohedral calcium carbonate crystals along the downstream section of the core (**Figure 2.13**). Such localized downstream precipitation has been reported in previous studies by Cao et al. (2015) and Huerta et al. (2011), and is attributed to the increase in pH and concentration of calcium ions in the downstream section of the core, conditions which can promote precipitation of secondary carbonate minerals (e.g., $CaCO_3$). In this study, the pH of the injected fluid increased from 3.1 (influent) to over 4 (effluent) during the experiment**.** XCT analysis also showed the development of preferential flow channels along the fracture pathway, which may be due to reaction front instabilities or non-uniform aperture distribution of the initial fracture. An orange coloration similar to that observed in the batch study maps the flow path along the fracture (**Figure 2.13**).

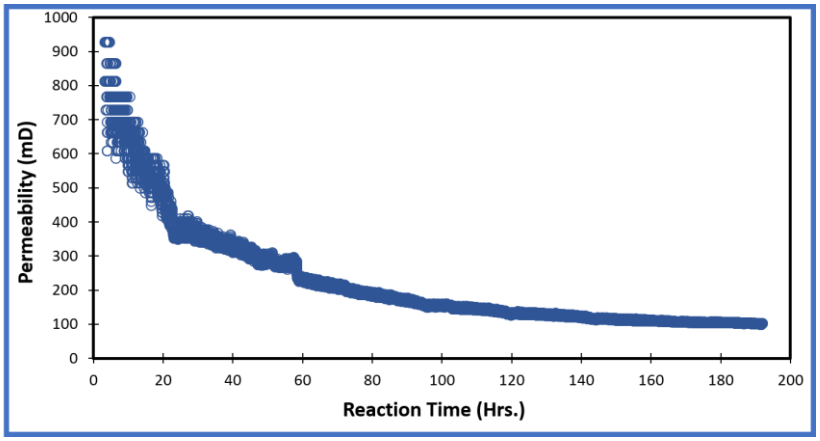

Figure 2.12: Permeability evolution of a saw-cut half-inch ECC core under flow-through conditions, determined using the cubic law for flow of an incompressible fluid between two parallel smooth plates. Permeability along the fracture pathway decreased from approximately 930 mD to 100 mD after 192 hours.

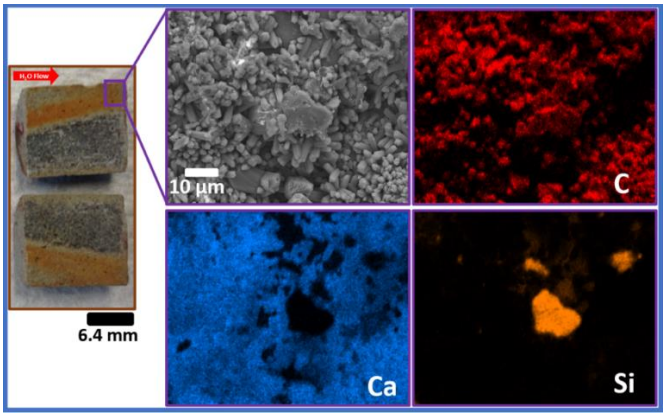

Figure 2.13: Image of half sections of the saw-cut 0.5-inch core following the flow-through experiment (left). The orange coloration delineates the region of preferential flow in the second half of the core (left). Precipitate identified to be calcite was found in the downstream section of the core (right). EDS maps show that precipitate in the downstream section of the core is rich in Ca and C.

2.5 Conclusion

Although it is unlikely that diffusion of CO_2 through well-placed cement will lead to CO_2 leakage from reservoirs during GCS operations (Carroll et al., 2016; Crow et al., 2010), spalling and brittle fracturing of wellbore cement following carbonation or cyclic stresses may compromise

the long-term safety and security of CO_2 storage (Barlet-Gouédard et al., 2006; Q. Li et al., 2015). In this work, a novel fiber-reinforced cementitious material engineered for superior tensile ductility and intrinsically tight crack width in comparison to conventional Portland cement was tested under typical GCS temperature and pressure conditions to investigate its performance as an effective barrier for CO_2 leakage. Optical microscopy, XCT, and BSE analyses all showed that the depth of carbonation was limited to the rim of the core with a 50-year estimated altered depth of 72 mm. This suggests that diffusion of CO_2 into the ECC matrix is unlikely to lead to CO_2 leakage from the reservoir. Microhardness results also showed that carbonation reactions did not diminish the mechanical integrity of ECC. The absence of spalling as well as limited occurrence and width of microcracks, which were generally less than 60µm, showed that carbonation did not induce extensive damage to the core because of the engineered properties of ECC. This suggests that the use of ECC as a wellbore cementing material may serve to limit crack width, which could help promote self-healing in damaged wellbore cement. ECC was also shown to withstand prolonged contact with aggressive CO_2-acidified fluids while maintaining its mechanical integrity under GCS conditions. However, further studies are needed to understand the more detailed effect of carbonation on the tensile strength and crack healing potential in ECC used for GCS wellbore sealing applications.

2.6 References

Armbruster, T., Danisi, R.M., 2015. Highlights in Mineralogical Crystallography. De Gruyter, Berlin, Boston. https://doi.org/10.1515/9783110417104

Bachu, S., 2000. Sequestration of CO_2 in geological media: criteria and approach for site selection in response to climate change. Energy Convers Manag 41, 953–970. https://doi.org/10.1016/S0196-8904(99)00149-1

Bachu, S., Celia, M.A., 2009. Assessing the potential for CO_2 leakage, particularly through wells, from geological storage sites, in: Geophysical Monograph Series. American Geophysical Union, Washington, D. C., pp. 203–216.

Barlet-Gouédard, V., Rimmelé, G., Goffé, B., Porcherie, O., 2007. Well Technologies for CO_2 Geological Storage: CO_2-Resistant Cement. Oil Gas Sci. Technol. - Rev. IFP 62, 325–334. https://doi.org/10.2516/ogst:2007027

Barlet-Gouédard, V., Rimmelé, G., Goffe, B., Porcherie, O., 2006. Mitigation Strategies for the Risk of CO_2 Migration Through Wellbores. Presented at the Presented at the IADC/SPE Drilling Conference, p. 17. https://doi.org/10.2118/98924-MS

Barlet-Gouédard, V., Rimmelé, G., Porcherie, O., Quisel, N., Desroches, J., 2009. A solution against well cement degradation under CO_2 geological storage environment. Int. J. Greenh. Gas Control 3, 206–216. https://doi.org/10.1016/j.ijggc.2008.07.005

Brandl, A., Cutler, J., Seholm, A., Sansil, M., Braun, G., Incorporated, B.H., 2011. Cementing Solutions for Corrosive Well Environments 12.

Bruckdorfer, R.A., 1986. Carbon Dioxide Corrosion in Oilwell Cements. Presented at the SPE Rocky Mountain Regional Meeting, Society of Petroleum Engineers. https://doi.org/10.2118/15176-MS

Brunet, J. -p. L., Li, L., Karpyn, Z.T., Huerta, N.J., 2016. Fracture opening or self-sealing: Critical residence time as a unifying parameter for cement–CO_2–brine interactions. Int J Greenh Gas Control 47, 25–37. https://doi.org/10.1016/j.ijggc.2016.01.024

Cao, P., Karpyn, Z.T., Li, L., 2015. Self-healing of cement fractures under dynamic flow of CO2-rich brine. Water Resour Res 51, 4684–4701. https://doi.org/10.1002/2014WR016162

Carey, J.W., 2013. Geochemistry of Wellbore Integrity in CO2 Sequestration: Portland Cement-Steel-Brine-CO_2 Interactions. Rev Miner. 77, 505–539. https://doi.org/10.2138/rmg.2013.77.15

Carroll, S., Carey, J.W., Dzombak, D., Huerta, N.J., Li, L., Richard, T., Um, W., Walsh, S.D.C., Zhang, L., 2016. Review: Role of chemistry, mechanics, and transport on well integrity in CO_2 storage environments. Int J Greenh Gas Control 49, 149–160. https://doi.org/10.1016/j.ijggc.2016.01.010

Carter, L.G., Slagle, K.A., Smith, D.K., 1968. Stress Capabilities Improved by Resilient Cement. Presented at the Drilling and Production Practice, American Petroleum Institute.

Cavanagh, P.H., Johnson, C.R., Le Roy-Delage, S., DeBruijn, G.G., Cooper, I., Guillot, D.J., Bulte, H., Dargaud, B., 2007. Self-Healing Cement - Novel Technology to Achieve Leak-Free Wells. Presented at the SPE/IADC Drilling Conference, Society of Petroleum Engineers. https://doi.org/10.2118/105781-MS

Chow, J.C., Watson, J.G., Herzog, A., Benson, S.M., Hidy, G.M., Gunter, W.D., Penkala, S.J., White, C.M., 2003. Separation and Capture of CO_2 from Large Stationary Sources and Sequestration in Geological Formations. J. Air Waste Manag Assoc 53, 1172–1182. https://doi.org/10.1080/10473289.2003.10466274

Crow, W., Carey, J.W., Gasda, S., Brian Williams, D., Celia, M., 2010. Wellbore integrity analysis of a natural CO_2 producer. Int. J. Greenh. Gas Control, The Ninth International Conference on Greenhouse Gas Control Technologies 4, 186–197. https://doi.org/10.1016/j.ijggc.2009.10.010

Dean, G.D., Torres, R.S., 2002. Novel Cement System for Improved Zonal Isolation in Steam Injection Wells. Presented at the SPE International Thermal Operations and Heavy Oil Symposium and International Horizontal Well Technology Conference, Society of Petroleum Engineers. https://doi.org/10.2118/78995-MS

Deel, D., 2007. Carbon Sequestration Technology Roadmap and Program Plan 2007 48.

Deremble, L., Loizzo, M., Huet, B., Lecampion, B., Quesada, D., 2011. Stability of a leakage pathway in a cemented annulus. Energy Procedia, 10th International Conference on Greenhouse Gas Control Technologies 4, 5283–5290. https://doi.org/10.1016/j.egypro.2011.02.508

Dieter, G.E., Bacon, D.J., 1986. Mechanical metallurgy. McGraw-hill New York.

Duan, Z., Sun, R., 2003. An improved model calculating CO_2 solubility in pure water and aqueous NaCl solutions from 273 to 533 K and from 0 to 2000 bar. Chem. Geol. 193, 257–271. https://doi.org/10.1016/S0009-2541(02)00263-2

Duguid, A., Scherer, G.W., 2010. Degradation of oilwell cement due to exposure to carbonated brine. Int J Greenh Gas Control 4, 546–560. https://doi.org/10.1016/j.ijggc.2009.11.001

Ellis, B.R., Fitts, J.P., Bromhal, G.S., McIntyre, D.L., Tappero, R., Peters, C.A., 2013. Dissolution-Driven Permeability Reduction of a Fractured Carbonate Caprock. Environ. Eng. Sci. 30, 187–193. https://doi.org/10.1089/ees.2012.0337

Engelke, B., Miranda, D., R, C., Daou, F., Petersen, D., Aponte, S.A., Oliveira, F., Ocando, L.M.S., Conceição, A.C.F., Guillot, D., 2017. CO_2 Self-Healing and Resistant Cement Technology From Laboratory to the Field. Presented at the SPE/IADC Drilling Conference and Exhibition, Society of Petroleum Engineers. https://doi.org/10.2118/184641-MS

Fabbri, A., Corvisier, J., Schubnel, A., Brunet, F., Goffé, B., Rimmele, G., Barlet-Gouédard, V., 2009. Effect of carbonation on the hydro-mechanical properties of Portland cements. Cem 39, 1156–1163. https://doi.org/10.1016/j.cemconres.2009.07.028

Fernández Bertos, M., Simons, S.J.R., Hills, C.D., Carey, P.J., 2004. A review of accelerated carbonation technology in the treatment of cement-based materials and sequestration of CO_2. J. Hazard. Mater. 112, 193–205. https://doi.org/10.1016/j.jhazmat.2004.04.019

Herbert, E.N., Li, V.C., 2013. Self-Healing of Microcracks in Engineered Cementitious Composites (ECC) Under a Natural Environment. Materials 6, 2831–2845. https://doi.org/10.3390/ma6072831

Huerta, N.J., Bryant, S.L., Strazisar, B.R., Hesse, M., 2011. Dynamic alteration along a fractured cement/cement interface: Implications for long term leakage risk along a well with an annulus defect. Energy Procedia 4, 5398–5405. https://doi.org/10.1016/j.egypro.2011.02.524

Huerta, N.J., Bryant, S.L., Strazisar, B.R., Kutchko, B.G., Conrad, L.C., 2009. The influence of confining stress and chemical alteration on conductive pathways within wellbore cement. Energy Procedia 1, 3571–3578.

Huerta, N.J., Hesse, M.A., Bryant, S.L., Strazisar, B.R., Lopano, C., 2016. Reactive transport of CO_2-saturated water in a cement fracture: Application to wellbore leakage during geologic

CO_2 storage. Int J Greenh Gas Control 44, 276–289. https://doi.org/10.1016/j.ijggc.2015.02.006

Johnson, J.W., Oelkers, E.H., Helgeson, H.C., 1992. SUPCRT92: A software package for calculating the standard molal thermodynamic properties of minerals, gases, aqueous species, and reactions from 1 to 5000 bar and 0 to 1000 C. Comput. Geosci. 18, 899–947.

Kan, Shi, H. -s., Sakulich, A.R., Li, V.C., 2010. Self-Healing Characterization of Engineered Cementitious Composite Materials. ACI Mater 107, 617–624.

Kanopoulos, N., Vasanthavada, N., Baker, R.L., 1988. Design of an image edge detection filter using the Sobel operator. IEEE J Solid-State Circuits 23, 358–367. https://doi.org/10.1109/4.996

Kawabata, Y., Kato, E., Iwanami, M., 2012. Enhanced Long-Term Resistance of Concrete with Marine Sessile Organisms to Chloride Ion Penetration [WWW Document]. URL.

Kutchko, B.G., Strazisar, B.R., Dzombak, D.A., Lowry, G.V., Thaulow, N., 2007. Degradation of Well Cement by CO_2 under Geologic Sequestration Conditions. Env. Sci Technol 41, 4787–4792. https://doi.org/10.1021/es062828c

Kutchko, B. G., Strazisar, B.R., Huerta, N., Lowry, G.V., Dzombak, D.A., Thaulow, N., 2009. CO_2 Reaction with Hydrated Class H Well Cement under Geologic Sequestration Conditions: Effects of Flyash Admixtures. Env. Sci 43, 3947–3952. https://doi.org/10.1021/es803007e

Kutchko, Barbara G., Strazisar, B.R., Huerta, N., Lowry, G.V., Dzombak, D.A., Thaulow, N., 2009. CO_2 Reaction with Hydrated Class H Well Cement under Geologic Sequestration Conditions: Effects of Flyash Admixtures. Environ. Sci. Technol. 43, 3947–3952. https://doi.org/10.1021/es803007e

Kutchko, B.G., Strazisar, B.R., Lowry, G.V., Dzombak, D.A., Thaulow, N., 2008. Rate of CO_2 Attack on Hydrated Class H Well Cement under Geologic Sequestration Conditions. Env. Sci 42, 6237–6242. https://doi.org/10.1021/es800049r

Lafuente, B., Downs, R.T., Yang, H., Stone, N., 2015. 1. The power of databases: The RRUFF project, in: Highlights in Mineralogical Crystallography. De Gruyter, Berlin, Boston. https://doi.org/10.1515/9783110417104-003

Le Saoût, G., Lécolier, E., Rivereau, A., Zanni, H., 2006. Chemical structure of cement aged at normal and elevated temperatures and pressures, Part II: Low permeability class G oilwell cement. Cem. Concr. Res. 36, 428–433. https://doi.org/10.1016/j.cemconres.2005.11.005

Li, Q., Lim, Y.M., Flores, K.M., Kranjc, K., Jun, Y.-S., 2015. Chemical Reactions of Portland Cement with Aqueous CO_2 and Their Impacts on Cement's Mechanical Properties under Geologic CO_2 Sequestration Conditions. Env. Sci Technol 49, 6335–6343. https://doi.org/10.1021/es5063488

Li, V.C., 2009. Engineered Cementitious Composites (ECC) – material, structural and durability performance, in: Concrete Construction Engineering Handbook. CRC Press, Boca Raton.

Li, V.C., 2003. On engineered cementitious composites (ECC). J Adv 1, 215–230.

Li, V.C., 2002. Advances in ECC research. Spec. Publ. 206, 373–400.

Li, V.C., Yang, E.-H., 2007a. Self Healing in Concrete Materials, in: Self Healing Materials, Springer Series in Materials Science. Springer, Dordrecht, pp. 161–193. https://doi.org/10.1007/978-1-4020-6250-6_8

Li, V.C., Yang, E.-H., 2007b. Self healing in concrete materials, in: Self Healing Materials. Springer, pp. 161–193.

Li, W., Zhou, X., Li, N., 2015. Research on the Effect of Fly Ash Content on the Tensile Properties of PVA-ECC.

Liu, H., Zhang, Q., Gu, C., Su, H., Li, V.C., 2016. Influence of micro-cracking on the permeability of engineered cementitious composites. Cem. Concr. Compos. 72, 104–113. https://doi.org/10.1016/j.cemconcomp.2016.05.016

Luquot, L., Abdoulghafour, H., Gouze, P., 2013. Hydro-dynamically controlled alteration of fractured Portland cements flowed by CO_2-rich brine. Int. J. Greenh. Gas Control 16, 167–179. https://doi.org/10.1016/j.ijggc.2013.04.002

Lye, C.-Q., Dhir, R.K., Ghataora, G.S., 2015. Carbonation resistance of fly ash concrete. Mag. Concr. Res. 67, 1150–1178. https://doi.org/10.1680/macr.15.00204

Mason, H.E., Frane, D., W. L., W., S. D. C., D., Z., C., S., C., 2013. Chemical and Mechanical Properties of Wellbore Cement Altered by CO_2-Rich Brine Using a Multianalytical Approach 2013, 1745–1752. https://doi.org/10.1021/es3039906

Matteo, E.N., Huet, B., Jové-Colón, C.F., Scherer, G.W., 2018. Experimental and modeling study of calcium carbonate precipitation and its effects on the degradation of oil well cement during carbonated brine exposure. Cem. Concr. Res. 113, 1–12. https://doi.org/10.1016/j.cemconres.2018.03.016

Matteo, E.N., Scherer, G.W., 2012. Experimental study of the diffusion-controlled acid degradation of Class H Portland cement. Int. J. Greenh. Gas Control 7, 181–191. https://doi.org/10.1016/j.ijggc.2011.07.012

McGrail, B.P., Schaef, H.T., Ho, A.M., Chien, Y. -j., Dooley, J.J., Davidson, C.L., 2006. Potential for carbon dioxide sequestration in flood basalts. J Geophys Res 111. https://doi.org/10.1029/2005JB004169

Michaux, M., Nelson, E.B., Vidick, B., 1990. 2 Chemistry and Characterization of Portland Cement, in: Nelson, E.B. (Ed.), Developments in Petroleum Science, Well Cementing. Elsevier, pp. 2–1. https://doi.org/10.1016/S0376-7361(09)70300-0

Morris, W., Criado, M.A., Robles, J., Bianchi, G., 2003. Design of High Toughness Cement for Effective Long Lasting Well Isolations. Presented at the SPE Latin American and Caribbean Petroleum Engineering Conference, Society of Petroleum Engineers. https://doi.org/10.2118/81001-MS

Nelson, E.B., Baret, J.-F., Michaux, M., 1990. 3 Cement Additives and Mechanisms of Action, in: Nelson, E.B. (Ed.), Developments in Petroleum Science, Well Cementing. Elsevier, pp. 3–1. https://doi.org/10.1016/S0376-7361(09)70301-2

Neves Junior, A., Toledo Filho, R.D., Fairbairn, E. de M.R., Dweck, J., 2013. CO2 sequestration by high initial strength Portland cement pastes. J. Therm. Anal. Calorim. 113, 1577–1584. https://doi.org/10.1007/s10973-013-3117-0

Neville, A.M., 2011. Properties of concrete, 5th ed. ed. Pearson, Harlow, England ; New York.

Pham, S.T., Prince, W., 2014. The Carbonation of Calcium-Silicate-Hydrate C-S-H in Cement Mortar Studied Using Thermal Analysis and Gas Pycnometer: Determination of the Quantity of Calcium Carbonate Produced and the Increase in Molar Volume. Adv Mater 931, 411–415. https://doi.org/10.4028/www.scientific.net/AMR.931-932.411

Reddy, B.R., Liang, F., Fitzgerald, R., 2010. Self-Healing Cements That Heal Without Dependence on Fluid Contact: A Laboratory Study. SPE Drill. Complet. 25, 309–313. https://doi.org/10.2118/121555-PA

Redon, C., Li, V.C., Wu, C., Hoshiro, H., Saito, T., Ogawa, A., 2001. Measuring and modifying interface properties of PVA fibers in ECC matrix. J. Mater. Civ. Eng. 13, 399–406.

Rimmelé, G., Barlet-Gouédard, V., Porcherie, O., Goffé, B., Brunet, F., 2008. Heterogeneous porosity distribution in Portland cement exposed to CO2-rich fluids. Cem. Concr. Res. 38, 1038–1048. https://doi.org/10.1016/j.cemconres.2008.03.022

Sahmaran, M., Li, M., Li, V.C., 2007. Transport properties of engineered cementitious composites under chloride exposure. ACI Mater 104, 604–611.

Sakulich, A.R., Li, V.C., 2011. Nanoscale characterization of engineered cementitious composites (ECC). Cem 41, 169–175. https://doi.org/10.1016/j.cemconres.2010.11.001

Schaef, H.T., McGrail, B.P., 2009. Dissolution of Columbia River Basalt under mildly acidic conditions as a function of temperature: Experimental results relevant to the geological sequestration of carbon dioxide. Appl Geochem 24, 980–987. https://doi.org/10.1016/j.apgeochem.2009.02.025

Spycher, N., Pruess, K., 2005. CO_2-H_2O mixtures in the geological sequestration of CO_2. II. Partitioning in chloride brines at 12–100°C and up to 600 bar. Geochim. Cosmochim. Acta 69, 3309–3320. https://doi.org/10.1016/j.gca.2005.01.015

Stutzman, P.E., 2001. Scanning electron microscopy in concrete petrography. Natl Inst 2.

Thiery, M., Dangla, P., Villain, G., Platret, G., 2005. A prediction model for concrete carbonation based on coupled CO_2-H_2O-ions transfers and chemical reactions, in: Proc. of 10 Th DBMC. Conference on Durability of Building Materials and Components, pp. 1–8.

Tosun-Felekoğlu, K., Felekoğlu, B., Ranade, R., Lee, B.Y., Li, V.C., 2014. The role of flaw size and fiber distribution on tensile ductility of PVA-ECC. Compos Part B Eng 56, 536–545. https://doi.org/10.1016/j.compositesb.2013.08.089

Tsang, Y.W., Witherspoon, P.A., 1981. Hydromechanical behavior of a deformable rock fracture subject to normal stress. J. Geophys. Res. Solid Earth 86, 9287–9298. https://doi.org/10.1029/JB086iB10p09287

Verbeck, G., 1958. Carbonation of Hydrated Portland Cement, in: Committee C-1, Committee C-9 (Eds.), Cement and Concrete. ASTM International, 100 Barr Harbor Drive, PO Box C700, West Conshohocken, PA 19428-2959, pp. 17-17–20. https://doi.org/10.1520/STP39460S

Walsh, S.D.C., Frane, W.L.D., Mason, H.E., Carroll, S.A., 2013. Permeability of Wellbore-Cement Fractures Following Degradation by Carbonated Brine. Rock Mech Rock Eng 46, 455–464. https://doi.org/10.1007/s00603-012-0336-9

Watson, T.L., Bachu, S., 2009. Evaluation of the Potential for Gas and CO_2 Leakage Along Wellbores. SPE Drill 24, 115–126. https://doi.org/10.2118/106817-PA

Yang, E.-H., Yang, Y., Li, V.C., 2007. Use of High Volumes of Fly Ash to Improve ECC Mechanical Properties and Material Greenness. ACI Mater. J. Farmington Hills 104, 620–628.

Yang, Sahmaran, M., Yang, Y., Li, V.C., 2009. Rheological Control in Production of Engineered Cementitious Composites. ACI Mater. J. Farmington Hills 106, 357–366.

Yang, Y., Lepech, M.D., Yang, E. -h., Li, V.C., 2009. Autogenous healing of engineered cementitious composites under wet–dry cycles. Cem 39, 382–390. https://doi.org/10.1016/j.cemconres.2009.01.013

Yao, X., Hua, S., 2007. Design of Novel Composite Agent for Improving the Toughness of Oil-Well Cement Sheath. Presented at the International Symposium on Oilfield Chemistry, Society of Petroleum Engineers. https://doi.org/10.2118/106010-MS

Zhang, L., Dzombak, D.A., Nakles, D.V., Hawthorne, S.B., Miller, D.J., Kutchko, B.G., Lopano, C.L., Strazisar, B.R., 2014. Rate of H_2S and CO_2 attack on pozzolan-amended Class H well cement under geologic sequestration conditions. Int. J. Greenh. Gas Control 27, 299–308. https://doi.org/10.1016/j.ijggc.2014.02.013

Zhang, L., Dzombak, D.A., Nakles, D.V., Hawthorne, S.B., Miller, D.J., Kutchko, B.G., Lopano, C.L., Strazisar, B.R., 2013. Characterization of pozzolan-amended wellbore cement exposed to CO_2 and H_2S gas mixtures under geologic carbon storage conditions. Int. J. Greenh. Gas Control 19, 358–368. https://doi.org/10.1016/j.ijggc.2013.09.004

Zhang, P., Li, Q.-F., 2013. Combined effect of polypropylene fiber and silica fume on workability and carbonation resistance of concrete composite containing fly ash. Proc. Inst. Mech. Eng. Part J. Mater. Des. Appl. 227, 250–258. https://doi.org/10.1177/1464420712458198

Zimmerman, R.W., Bodvarsson, G.S., 1996. Hydraulic conductivity of rock fractures. Transp. Porous Media 23, 1–30. https://doi.org/10.1007/BF00145263

CHAPTER 3

Mechanical Integrity of Engineered Cementitious Composite Exposed to CO_2 under GCS Temperature and Pressure Conditions

Reprinted from: Jubilee T. Adeoye , Duo Zhang , Victor C. Li , and Brian R. Ellis, Novel ductile wellbore cementitious composite for geologic CO_2 storage, International Journal of Greenhouse Gas Control, 2019, https://doi.org/10.1016/j.ijggc.2019.102896.

3.1 Introduction

Geologic CO_2 storage (GCS) has been identified as a bridging technology to slow global climate change due to its ability to stabilize the atmospheric concentration of CO_2 by eliminating large streams of the greenhouse gas (IPCC and Metz, 2005). However, leakage of stored CO_2 from geologic reservoirs through damaged or abandoned wells remains a major risk adopting GCS as a long-term strategy to slow global climate change (Bachu and Celia, 2009; Chow et al., 2003; Deel, 2007; Nordbotten et al., 2009, 2005; Watson and Bachu, 2009). Wellbore pathways through which CO_2 can leak from geologic reservoirs have been well-documented and include fractured cement sheaths, damaged steel casing, and steel casing/cement interface defects and cement/formation annular gaps (Bachu and Celia, 2009; Carroll et al., 2016). In particular, leakage of CO_2 through fractured cement sheaths is a major concern as conventional wellbore cementing materials are made of Portland cement, a brittle material that can be damaged by stresses generated during CO_2 injection and cyclic thermal swings (Nelson, 1990; Roy et al., 2018).

Previous studies that investigated the long-term effect of exposing wellbore cement to CO_2 have shown that the risks of cement sheath damage increase following carbonation and the overall mechanical strength of cement will be compromised following exposure to CO_2 under GCS conditions (Barlet-Gouédard et al., 2007; Fabbri et al., 2009; Li et al., 2015). Barlet-Gouédard et al. (2007) reported a 65% and 30% loss of bulk compressive strength in Portland cement exposed to CO_2-acidified water and wet supercritical CO_2, respectively, for six weeks at temperature and pressure conditions of 90^{o}C and 28 MPa. The exposure of the cement to CO_2 also led to damage and degradation characterized by spalling and cracking. In the study carried out by Li et al. (2015) on Portland cement coupons exposed to CO_2-acidified brine at temperature and pressure conditions of 95^{o}C and 10 MPa, three-point bending test and nanoindentation analysis were carried out on the coupons to investigate the effect of CO_2 on both the overall flexural and microstructural strength of the cement. Significant reduction in the overall flexural strength and modulus of elasticity was observed in samples exposed to CO_2 in comparison to control samples exposed to nitrogen headspace under similar temperature and pressure conditions. Fabbri et al. (2009) reported deterioration of the in-situ hydro-mechanical properties of Portland cement cores after several weeks of exposure to CO_2 at temperature and pressure conditions of 90^{o}C and 28 MPa. This alteration led to an increase in the permeability of the cement cores, potentially increasing the risk of CO_2 leakage. Because the integrity of wellbore cement sheath is crucial for CO_2 storage security during GCS, there is a need to ensure that materials used in wellbore cementing can withstand the cyclic stresses induced during CO_2 injection, which are variable but can be in excess of 25 MPa (Jen et al., 2017; Rutqvist et al., 2007), and limit the extent of cement sheath damage under such conditions.

Engineered cementitious composite (ECC), a class of fiber-reinforced cementitious composites that exhibit high tensile ductility, is being proposed here as a possible candidate for wellbore cementing during GCS. ECC exhibits strain hardening behavior through forming multiple fine cracks at the microscale, typically less than 60 μm, instead of brittle failure observed in conventional wellbore cement. Studies have shown that ECC has a tensile strain capacity in the range of 2 to 5%, which is 200 to 500 times that of Portland cement and concrete (Li, 2009, 2003). Because tight cracks in conventional wellbore cement have been shown to heal autogenously when in contact with CO_2-rich fluids (Cao et al., 2015; Carroll et al., 2016; Huerta et al., 2016), in comparison to larger cracks, the ability of ECC to maintain cracks typically less than 60 μm during the stain hardening stage makes it an attractive candidate for wellbore cementing applications during GCS.

In a recent study carried out by Adeoye et al. (2019) (see also Chapter 2 of this report) on conventional M45 ECC exposed to CO_2-saturated water at P_{CO2} of 10 MPa and temperature of 50°C, an increase in microhardness was observed in all regions of the composite following reaction with CO_2. The increase in hardness was attributed to pore refinement in the ECC matrix and reworking of parent cementitious material following carbonation. Such pore refinement and reworked matrix has been reported by Cheshire et al. (2017) in cement cores recovered from an injection well in a CO_2-enhanced oil recovery field in West Texas and can improve the resistance of the material to deformation and reduce fluid permeability through the composite. Adeoye et al. (2019) also observed that the fiber/matrix interfacial transition zone (ITZ) in the conventional ECC was densified with reaction products that were identified as calcium carbonate after exposure to CO_2. Such densification of the ITZ could impact the composite's ductility, long-term strain hardening property, and multiple cracking behavior of ECC, as the denser ITZ will increase the

bonding between fibers and matrix, potentially promoting rupturing of fibers rather than pullout under tensile stress (Li et al., 2002; Li, 2003; Redon et al., 2001). To determine the suitability of ECC as substitute for conventional wellbore cementing materials in injection wells during GCS, it is important to understand how the ductility and mechanical integrity of ECC will be impacted by reaction with CO_2 under typical GCS conditions.

This work investigates the changes in the mechanical properties of an ECC material formulated for wellbore cementing applications in order to predict its long-term integrity following exposure to CO_2 under typical GCS conditions. A series of static batch experiments were carried out, simulating diffusive mass flow conditions expected in wellbore cement sheath, and a four-point flexural test was used to determine the impact of CO_2 on the ductility and crack patterns in ECC in comparison to conventional wellbore cements. The evolution of ECC microstructure was also characterized to provide insight regarding the factors that will impact the overall mechanical performance of ECC during GCS.

3.2 Materials and methods

3.2.1 Material selection

ECC material selection was carried out to achieve a slurry with flow properties that are more representative of a wellbore cement slurry in comparison to conventional M45 ECC (**see Appendix B**) (Guillot, 1990; Li, 2009; Nelson et al., 1990). Silica sand used in conventional ECC was replaced with low calcium content Class F fly ash (ASTM C618, Type F) to improve the flowability of the mix in the fresh state. The chemical composition of the fly ash used is presented in **Table 3.1**. Type III cement, which is early-strength cement, was used for the ECC mix instead of Class H wellbore cement to compensate for the negative effect of high fly ash content and water to cement ratio on early-age strength development. Type III cement is able to develop early-age

strength faster than Class H wellbore cement because of its higher surface area (5000 m^2/kg) in comparison to Class H wellbore cement (1600 m^2/kg) and higher Al-phase content (Michaux et al., 1990). REC 15 polyvinyl alcohol (PVA) fiber with length of 8 mm and 0.5% oil coating supplied by Kuraray Ltd. (Japan) was chosen over the 12 mm fiber used in standard M45 ECC because shorter fibers promote more uniform fiber dispersion in a low viscosity mix. The physical and mechanical properties of the PVA fibers are presented in **Table 3.2**. Anti-settling agent was added to prevent free-water by promoting gelation in the fresh mixture and dispersant was added for viscosity control. Samples were mixed using tap water. For the sake of brevity, this version of ECC is labeled in this paper as WECC (wellbore ECC). Reference samples representing conventional wellbore cement were prepared using Class H cement.

Table 3.1: Chemical composition of fly ash.

Chemical composition	**SiO_2**	**Al_2O_3**	**Fe_2O_3**	**SO_3**	**CaO**	**MgO**	**Na_2O**	**K_2O**	**LOI***
% (by weight)	51.8	20.6	14.8	0.8	4.1	1.0	1.3	2.4	2.80

*LOI is loss on ignition

Table 3.2: Physical and mechanical properties of PVA fibers used in WECC.

Length (mm)	**Diameter (μm)**	**Density (kg/m3)**	**Tensile strength (MPa)**	**Elongation (%)**	**Young's modulus (GPa)**
8	39	1.3	1600	7	42

3.2.2 Sample preparation

Three sets of samples were prepared with the mix proportions presented in **Table 3.3**. WECC represents the composition of ECC proposed for wellbore cementing applications during GCS. Fiber-free WECC (hereafter referred to as FFWECC) has the same composition as WECC, but the

fibers have been excluded from the mix to isolate the unique impact of the fibers on the microstructural behavior of WECC under GCS conditions. Thus, FFWECC is comparable to conventional fly ash-amended wellbore cement (Kutchko et al., 2009; Zhang et al., 2014). Class H composition is the conventional wellbore cementing material (Nelson et al., 1990). Both FFWECC and Class H served as benchmarks to evaluate the mechanical performance of WECC.

Table 3.3: Composition of materials. Water content is reported as a fraction of the total solid weight WECC: wellbore ECC; FFWECC: fiber-free WECC; Class H: conventional cement.

Sample Type	Solid Phase		Liquid Phase	Fiber vol. (%)
	Cement	Fly ash	Water	
WECC	0.5	0.5	0.45	1.1
FFWECC	0.5	0.5	0.45	0
Class H	1	0	0.38	0

Note: Additives including dispersant ($C_{11}H_5NaO_4S$)N, antifoam (AFE 1410), and anti-settling agents (ADVA 190) were added to modify slurry fresh state flow properties. Solid components are reported in wt. % of total.

For WECC, the solid components were dry-mixed at 200 rpm for 5 mins. A premixed solution containing the liquid components was then added to the mix over the course of 5 mins. Subsequently, PVA fibers were added to the slurry over a period of 2.5 mins, mixed at a constant rate of 200 rpm. The slurry was further mixed after the addition of the fibers for an additional 2.5 mins to enable uniform fiber dispersion. FFWECC was prepared using a similar approach as WECC, but the fiber addition process was excluded. For Class H cement, the cement was mixed for 3 mins followed by the addition of the premixed liquid components for 5 mins. All samples were prepared using a 6-liter countertop mixer (KitchenAid). The fresh slurries were cast in customized Plexiglas rectangular coupon molds (102 mm x 34 mm x 10 mm) shown in **Figure 3.1a** to generate several specimens for flexural testing, and in 2-inch cubic molds for compressive

test analysis. The specimens were placed in a curing chamber (Temp. = 22 ± 2°C and Rel. Humidity = 99 ± 1%) and demolded 24 hr after casting. The samples were then cured under this condition for 28 days.

3.2.3 Static batch experiments

Eight WECC/FFWECC and six Class H cement samples were placed in 600 mL batch reactors filled with 300 mL of deionized water with a resistivity greater than 18.2 MΩ-cm such that the samples were fully submerged **(Figure 3.1b)**. Pure water was used in this study to ensure that the samples were exposed to the most acidic environment under the chosen temperature and P_{CO2} conditions (Rimmelé et al., 2008; Spycher and Pruess, 2005). The temperature and P_{CO2} in the batch reactors were subsequently elevated to 50°C and 10 MPa, respectively. For WECC and FFWECC, two samples were retrieved from each reactor after 2, 7, 14, and 28 days, while Class H cement samples were retrieved after 2, 7, and 21 days. For each pair of samples retrieved from the reactor, the samples were replaced with two Teflon coupons of the same dimensions. This ensured a constant water level in the batch reactor throughout the experiment, such that the samples were completely submerged in water at all times, without needing to add additional water to the reactor. Similarly, two 2-inch cubic specimens of each sample type were exposed to CO_2-acidified water under the same temperature and pressure conditions and retrieved after 7 days of reaction.

To decouple the effect of elevated temperature and pressure conditions from the unique interactions between WECC and CO_2, a control experiment was set up in which the WECC coupons were exposed similarly to a N_2 headspace with P_{N2} of 10 MPa and temperature of 50°C. The headspace in the batch reactor was purged with nitrogen prior to starting the experiment to eliminate ambient air containing CO_2 from the reactor. After retrieving the samples from the

reactor, they were air-dried at room temperature conditions (23 ± 2°C) for 24 hr to expel surficial water before carrying out the four-point bending flexural test.

3.2.4 Four-point bending test

A four-point bending test was carried out to determine the ductility and ultimate flexural strength of the specimens, pre- and post-reaction with CO_2, using an Instron mechanical test frame equipped with Bluehill software (Instron) for actuator control and data acquisition. The sample stage was custom-made using single-piece aluminum frames for the upper and lower supports, with steel dowels used as rollers, as shown in **Figure 3.1c.**

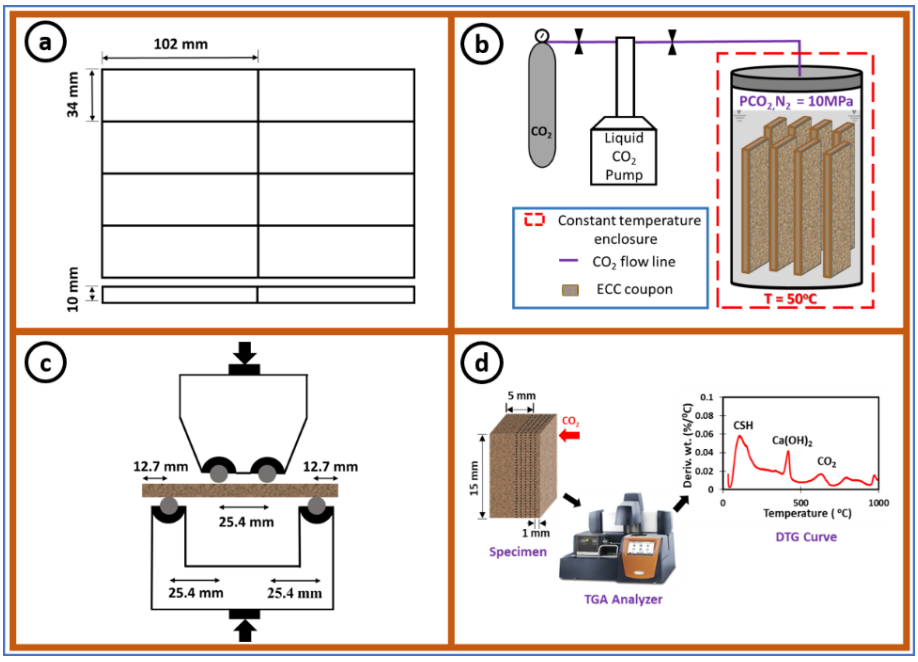

Figure 3.1: Experimental procedures for the study. **(a)** Customized mold for coupon specimens. Dimensions were chosen to maintain a coupon span to height ratio of 10:1. **(b)** Experimental setup for the batch study. Temperature and pressure were kept constant throughout the study. Coupons specimens were replaced with dummy Teflon coupons after sample retrieval. **(c)** Customized setup for the four-point bending test. Top and bottom sections of the test cell were cut out of a single piece aluminum block and steel dowels were used as rollers. **(d)** Flow diagram for TGA analysis.

The coupons were pre-loaded to 20 N and subsequently loaded at a constant displacement rate of 0.1 mm/min. The loading rate was maintained until the load dropped below 50% of the maximum load sustained by the sample. The flexural stress (σ_f) of the coupons was determined using **Eq. 3.1**:

$$\sigma_f = \frac{Fl}{bd^2} \qquad \textbf{Eq. 3.1}$$

where F is the loading force (N), l is the distance between the two supporting pins (mm), b is the width of the coupon (mm), and d is the thickness of the sample (ASTM, 2012). The modulus of rupture (σ_{fmax}) was computed based on the peak value of F.

3.2.5 Microhardness and compressive strength analyses

Microhardness analysis was carried out to determine the variation in local micromechanical strength and resistance to deformation of the different regions of the sample following acid attack.Samples were polished using a series of finer sandpaper grit sizes with a final finish achieved using a P2400-grit sandpaper and the test was carried out using a Vickers hardness tester (LECO). The altered and unaltered regions of the coupons were segmented into different zones, with more data points obtained from the edge of the sample in contact with CO_2-acidified water (Adeoye et al., 2019; Zhang et al., 2014). This ensured a higher resolution of the microhardness measured along the most altered region of the core. The test used a loading of 500 g and a dwell time of 10 seconds. The microhardness of each zone was reported as a hardness value (HV) for a 500 g load based on the average hardness of 12 indents, with higher HV indicating greater resistance of the material to deformation (Dieter and Bacon, 1986).

Compressive strength analysis was carried out on the carbonated and unaltered 2-inch cubes using a Forney compression machine (Forney). The initial load of 5 N was applied to the load cell and a constant loading rate of 3 N/s was applied until the peak load was attained. The test was stopped after the load dropped to 75% of the peak load. The compressive strength of the samples was then determined using **Eq. 3.2**:

$$F_m = \frac{P}{A} \qquad \textbf{Eq. 3.2}$$

Where F_m is the compressive strength in MPa, P is the total maximum load in N, and A is the area of loaded surface mm^2 (ASTM, 2016).

3.2.6 Extent of carbonation alteration

To determine the extent of alteration and carbonation of the samples following reaction with CO_2, each coupon was sectioned using a saw and the sectioned surface was stained with phenolphthalein pH indicator to determine the carbonated and uncarbonated regions based on the variation in the pH along the reaction front. The depth of the altered zone was estimated by taking the average of 10 measurements from the edge of the coupon to the edge of the altered zone (i.e., region of reduced pH).

To further compare the structural change and material loss along the edge of the sample following reaction with CO_2 in WECC and FFWECC, optical microscopy was carried out on the polished surface of the sectioned specimens using a Nikon LV100ND optical microscope (Nikon Instruments Inc.) equipped with a 5x magnification lens.

3.2.7 Mercury intrusion porosimetry

Quantitative changes in the porosity and pore size distribution of the specimens were determined using mercury intrusion porosimetry (MIP). Samples were cut into approximately 30

mm^3 sections and dewatered via solvent replacement by soaking in isopropanol for 7 days (Feldman, 1987; Gallé, 2001). Specimens were subsequently vacuum-dried in a desiccator at ambient temperature conditions for 72 hr. The samples were then analyzed in 5 cm^3 penetrometers using a MicroActive AutoPore V 9600 mercury intrusion porosimeter (Micromeritics Instrument Corporation) with maximum injection pressure of 421 MPa.

3.2.8 Thermogravimetric analysis

Thermogravimetric analysis (TGA) was used to quantify the hydrated products in WECC and FFWECC samples at different depths along the reaction front after exposure to CO_2-acidified water. 15 mm x 5 mm x 10 mm sections of the coupons were obtained and each sample was sanded at 1 mm intervals along the reaction front toward the center of the coupon as illustrated in **Figure 3.1d**. The first 1 mm section represents the section of the sample in direct contact with CO_2-acidified water. Samples were analyzed using a thermogravimetric analyzer (TA Instruments, SDT 650). 20 mg of each specimen was placed in a 90 μl aluminum crucible and the temperature was ramped up to 35ºC at a rate of 1ºC/ min, and held constant for 60 min to eliminate free-water (Neves Junior et al., 2019). The temperature was subsequently ramped up to 1000ºC at a rate of 10ºC per minute.

3.3 Results and discussion

3.3.1 Long-term alteration of WECC

Figure 3.2a presents the depth of carbonation at different time points for WECC and FFWECC, obtained by staining the cross-section of the specimens with phenolphthalein pH indicator before and after exposure to CO_2. The clear and pink regions of the stained surfaces represent the altered and unaltered sections of the coupons, respectively (RILEM, 1984; Verbeck, 1958; Zhang and Shao, 2016). The result indicates that the average depth of carbonation for WECC

and FFWECC after two days of reaction was 1.42 ± 0.17 mm and 1.41 ± 0.15 mm, respectively. Both WECC and FFWECC samples were fully carbonated after 28 days of reaction. The fact that the carbonation depths were comparable for both WECC and FFWECC throughout the tests suggests that the presence of fibers did not promote deeper penetration of CO_2 into the ECC matrix and will therefore not enhance the extent of carbonation under GCS conditions.

Figure 3.2b plots alteration depth as a function of the square root of time, which describes the extent of carbonation according to Fick's second law of diffusion and is typically used to estimate the rate of carbonation of cement in systems under constant concentration boundary conditions (Neville, 2011). The results show that the early time alteration of the WECC and FFWECC follow linear trends with $R_{WECC} = 0.98$ and $R_{FFWECC} = 0.99$ **(Figure 3.2b)**. Based on this correlation, CO_2 penetration through WECC and FFWECC at different time points was shown to be a diffusive process according to:

$$Y_{WECC} = 1.065x \qquad \textbf{Eq. 3.3}$$

$$Y_{FFWECC} = 1.056x \qquad \textbf{Eq. 3.4}$$

where $Y_{WECC,}$ Y_{FFWECC} are the depths of alteration in mm for ECC and FFWECC, respectively, and x is the square root of time in $days^{1/2}$. Based on **Eq. 3.3** and **Eq. 3.4**, the estimated extent of carbonation for the WECC and FFWECC samples after 28 days of exposure to CO_2-acidified water will be 5.63 and 5.58 mm, respectively. This is consistent with the observation in the 28-day samples that showed that the 10 mm thick samples had been fully carbonated after 28 days, as the carbonation progressed from all sides of the rectangular specimens. In contrast to the WECC and FFWECC samples in which significant carbonation was observed after reaction with CO_2, the Class H cement samples showed minimal carbonation that was limited to the edge of the coupons after 28 days of exposure to CO_2. This is attributed to the denser microstructure of Class H cement

due to the absence of fly ash and lower water content in comparison to the WECC and FFWECC mixes (Kutchko et al., 2009; Lye et al., 2015; Zhang and Li, 2013).

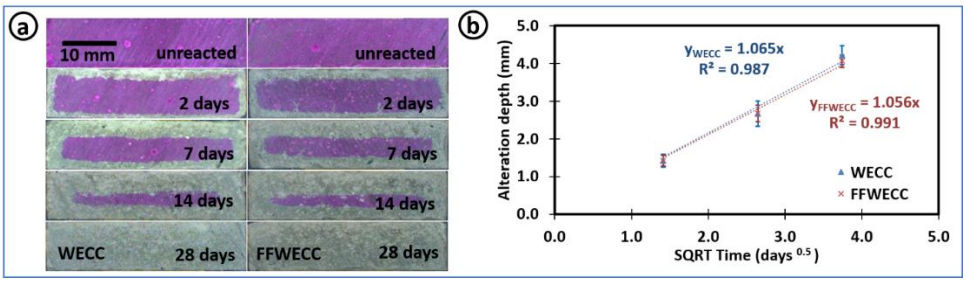

Figure 3.2: **(a)**. Alteration front of reacted and unreacted WECC and FFWECC specimens using phenolphthalein pH indicator. Pink and clear regions are the uncarbonated and carbonated regions of the samples, respectively. **(b)** The combined plot of the alteration depth vs. square root (SQRT) of time for WECC and FFWECC using phenolphthalein pH indicator. Equations Y_{WECC} and Y_{FFWECC} describe the extent of carbonation for WECC and FFWECC, respectively, as a function of time using phenolphthalein pH indicator. Error bars represent the standard deviation of 10 measurements of the altered depth from the edge of the coupon to the leading edge of the alteration zone. The goodness of the linear fit of the alteration depth vs. SQRT of time indicates that CO_2 transport in WECC and FFWECC is a diffusion-controlled process.

3.3.2 Effect of carbonation on mechanical integrity of WECC

The four-point bending tests carried out on WECC specimens showed that the unreacted sample exhibited multiple microcracking behavior and significant ductility. The reaction of WECC specimens with CO_2 impacted the ductility of ECC negatively, while the ductility of control samples exposed to N_2 headspace under the same temperature and pressure conditions remained relatively unaltered over the same period.

Figure 3.3a shows the stress-deflection curves as a function of time for WECC samples exposed to N_2 headspace. The unreacted WECC and all control samples exposed to N_2 headspace for 2, 7, 14, and 28 days showed deflection in the range of 2.2 to 2.5 mm at the maximum flexural stress and exhibited multiple cracking at the bottom surface of the coupons. The samples also showed a gradual decrease in stress relative to deflection, subsequent to achieving maximum

flexural strength, which is typical in strain hardening ECC (Mohamed and Li, 1994) rather than a sudden drop to zero observed in brittle wellbore cement after achieving maximum flexural strength.

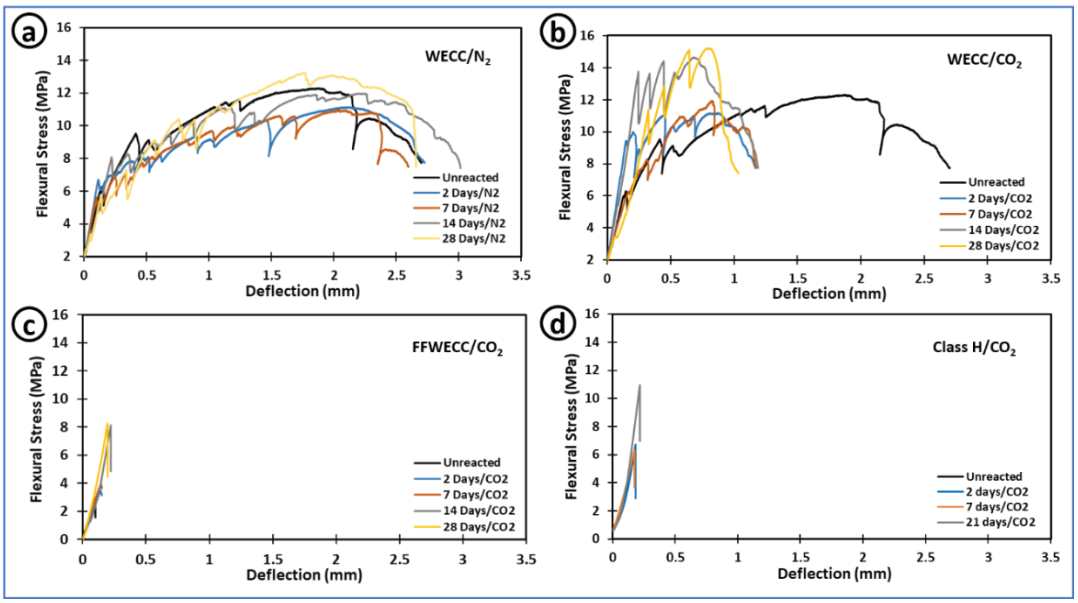

Figure 3.3: Four-point flexural stress-deflection curves for **(a)** unaltered and control WECC coupons exposed to N_2 headspace, **(b)** unaltered and carbonated WECC coupons **(c)** unaltered and carbonated FFWECC coupons **(d)** unaltered and carbonated Class H coupons, under GCS conditions of 50°C and 10 MPa.

Figure 3.3b shows the stress-deflection curves for WECC control samples exposed to CO_2-acidified water. In contrast to control samples exposed to N_2 headspace, carbonated WECC showed a significant decline in the total deflection of the specimens, with deflections in the range of 0.5 to 0.8 mm at the ultimate flexural stress. This deflection is approximately one-third of the deflection of control samples exposed to N_2 headspace. The carbonated samples also exhibited a rapid increase in stress relative to deflection characterized by the increase in the initial slope of the stress-deflection curve as the extent of carbonation increased. The significant decrease in ductility of WECC and rapid initial increase in stress relative to deflection after carbonation may be explained by stiffening and strengthening of the specimen by the combined effects of densification of the

microstructure of WECC matrix, as reported by Wu et al. (2018), and densification of the fiber-matrix interfacial transition zone (ITZ) reported by Adeoye et al. (2019) following carbonation. In particular, the densified ITZ increases the interfacial bonding between the fiber and the matrix such that the fibers are unable to pull out easily from the matrix under flexural stress, leading to fiber rupture and subsequent embrittlement of the composite.

Figure 3.3c and Figure 3.3d show the stress deflection curves of FFWECC and Class H cement samples, respectively. In contrast to WECC, which exhibited strain hardening and ductility, FFWECC and Class H samples exhibited brittle failure prior to and after exposure to CO_2. Similar to WECC, we observed an increase in the ultimate flexural strength of FFWECC and Class H wellbore cement with increased extent of carbonation. The modulus of rupture increased from 2.9 to 8.2 MPa and 6.2 to 10.9 MPa after 28 and 21 days of reaction, for FFWECC and Class H cement, respectively.

Table 3.4: Ultimate flexural strength (modulus of rupture), for specimens as a function of time.

	σ_{fmax} **unreacted (MPa)**	σ_{fmax} **2 days (MPa)**	σ_{fmax} **7 days (MPa)**	σ_{fmax} **14 days (MPa)**	σ_{fmax} **21 days (MPa)**	σ_{fmax} **28 day (MPa)**
$WECC_{CO2}$	12.3	11.2	11.9	14.6	NA	15.2
$WECC_{N2}$	12.3	11.1	10.9	11.9	NA	13.2
$FFWECC_{CO2}$	2.9	3.5	3.9	8.1	NA	8.2
Class H_{CO2}	6.2	6.7	6.3	NA	10.9	NA

Table 3.4 presents the ultimate flexural strength, known as the modulus of rupture, for each of the materials. It was observed that the ultimate flexural strength for WECC was consistently higher than that of FFWECC and Class H irrespective of the extent of carbonation of the material. Hence, while the carbonation reaction decreased the ductility of WECC, WECC continued to exhibit

superior ductile performance in comparison to conventional wellbore cementing materials under typical GCS conditions. In addition, the superior ductility and multiple cracking behavior of the unaltered WECC (**Figure 3.3a**) and WECC exposed to N_2 headspace (**Figure 3.3b**) suggest that ECC can potentially be employed for wellbore cementing in other deep geologic environments such as in oil and gas wells, in the absence of CO_2, without deterioration of its long- term strain hardening properties.

3.3.3 Microhardness and material integrity

Figure 3.4a and Figure 3.4b present hardness values for WECC and FFWECC specimens, respectively, pre- and post-reaction with CO_2. The results indicate that the resistance of WECC to deformation was not compromised following reaction with CO_2-acidified water in comparison to FFWECC. The average hardness of the WECC composite prior to carbonation was 37.9 ± 2.5 HV/500g. A general increase in hardness, both at the carbonated edge and uncarbonated core of the sample, was observed following reaction with CO_2. The fact that the uncarbonated region exhibited an increase in hardness can be explained by the pore refinement due to continuous cement hydration under high temperature and pressure conditions (Adeoye et al., 2019; Kutchko et al., 2009; Zhang et al., 2014). For the carbonated region, the highest hardness value was observed in the 0.5 to 1.0 mm section of the specimen, which indicates that the most substantial pore refinement due to carbonation occurred in this region. Although the WECC sample had been fully carbonated after 28 days of reaction, the sample showed higher microhardness in comparison to the unaltered material, indicating that reaction with CO_2 did not negatively alter its resistance to deformation. For FFWECC samples, the average hardness of the material prior to reaction was 37.6 ± 3.0 HV/500g, which was similar to the hardness of the unreacted WECC.

Similar to WECC, a general increase in the hardness of the material was observed at the core and edge of the FFWECC sample compared to the unreacted material following exposure to CO_2. While the WECC samples showed the highest hardness at the 0.5 to 1.0 mm zone of the coupon, the highest hardness values were measured in the 1.0 to 3.0 mm section of FFWECC coupons. At 28 days of exposure, the hardness of the FFWECC specimen was significantly lower at the edge of the coupon than the hardness of the samples exposed to CO_2 for 14 days. This is likely due to deterioration of material at the edge of the sample after prolonged exposure to the CO_2-acidified water. The fact that this sharp retrogression in hardness was not observed in WECC samples containing fibers suggests that the presence of fibers in WECC helped to maintain the structural stability of the material under the GCS conditions and may help maintain the integrity of the wellbore cement sheath following acid attack.

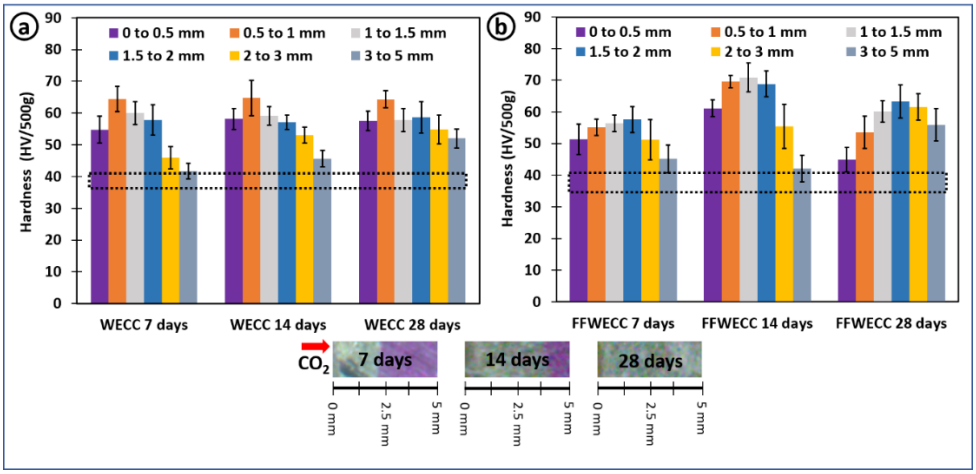

Figure 3.4: Time-dependent evolution of microhardness for (a) WECC and (b) FFWECC samples, respectively, following exposure to CO_2-acidified water at 50°C and 10 MPa P_{CO2} for 7, 14, and 28 days. The dotted lines in **Figure 3.4a** and **Figure 3.4b** represent the ranges of average hardness for uncarbonated WECC and FFWECC samples. Picture inserts at the bottom of the Figure indicate the extent of post-reaction alteration depth associated with both WECC and FFWECC samples revealed by phenolphthalein pH indicator.

Figure 3.5a and Figure 3.5b show optical images of the edge along the transverse section of the unaltered FFWECC coupon and FFWECC coupon after 28 days of exposure to CO_2-acidified water, respectively, while **Figure 3.5c** and **Figure 3.5d** show optical images of the edge of the unreacted WECC coupon and WECC coupon after 28 days of exposure to CO_2-acidified water. Although minimal material loss was observed at the edge of WECC samples after 28 days of reaction **(Figure 3.5d)** in comparison to the unreacted sample (**Figure 3.5c**), there was significant material loss at the edge of the FFWECC specimens in comparison to the unreacted FFWECC sample. This is consistent with the surface microhardness result that showed a significant decrease in the hardness of the FFWECC samples after 28 days of reaction, supporting the hypothesis that the presence of the fibers promoted the long-term structural stability of the composite which will help ensure the integrity of the cement sheath and promote secure storage during GCS.

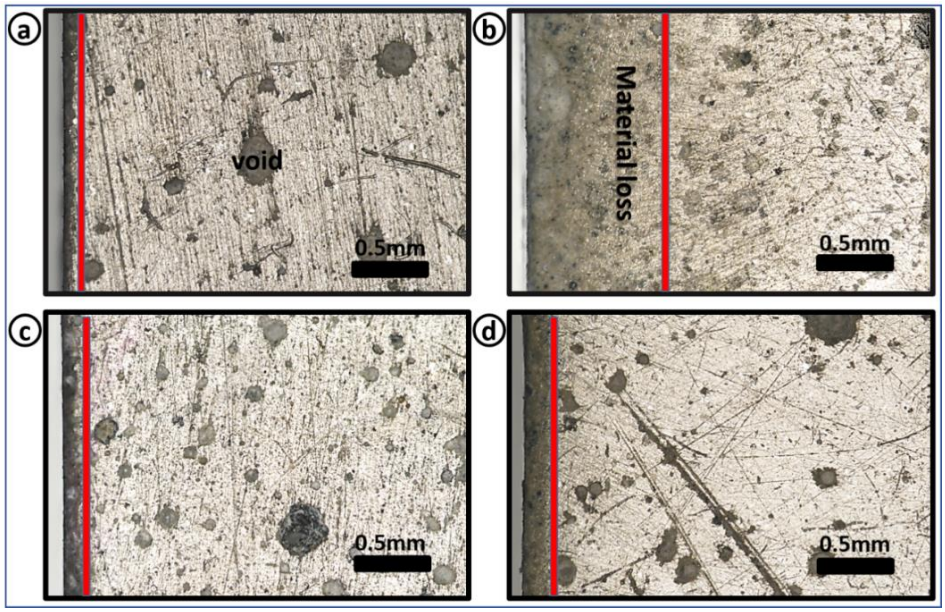

Figure 3.5: Optical image of **(a)** unaltered FFWECC coupon **(b)** FFWECC coupon after exposure to CO_2-acidified water **(c)** unaltered WECC coupon, and **(d)** WECC coupon after exposure to CO_2-acidified water, at temperature and pressure conditions of 50^{o}C and 10 MPa.

3.3.4 Evolution of compressive strength

Table 3.5 presents the average compressive strength for WECC, FFWECC, and Class H samples at different time points and exposure conditions. In wellbore cementing, the development of early age compressive strength of the cement ensures both structural support for the casing and zonal isolation of borehole intervals (Labibzadeh et al., 2010). The recommended compressive strength of wellbore cement after 24 hr is 3.5 MPa (500 psi) (Labibzadeh et al., 2010; Ridha et al., 2013). Meeting this target 24 hr compressive strength is crucial for wellbore cement design in order to limit the wait-on-cement time, i.e. the time between drilling operations, while ensuring the integrity of the cement job.

Table 3.5: Compressive strength for WECC, FFWECC, and Class H sample carbonation at early-age, late-age, and post carbonation.

Sample	24 hr unreacted	7 days unreacted	7 days carbonated	% post carbonation change
WECC	9.1	30.0	39.2	30.6
FFWECC	8.0	26.2	28.2	7.8
Class H	13.3	47.9	51.5	7.5

The results in **Table 3.5** indicate that the compressive strengths of WECC and FFWECC were comparable after 24 hr of curing, although the compressive strength of the WECC was slightly higher (9.1 MPa) than FFWECC (8.1 MPa). Class H cement showed considerably higher compressive strength (13.3 MPa) than both WECC and FFWECC. After 28 days of curing, the compressive strength of all sample types increased significantly as expected, with WECC, FFWECC, and Class H having compressive strengths of 30, 26.2, and 47.9 MPa, respectively. The fact that the 24-hr and 28-day compressive strengths of WECC and FFWECC samples were consistently lower than that of Class H cement is due to the high volume of fly ash in WECC and

FFWECC, up to 50% replacement by mass. Such high-volume substitution of cement with fly ash has been shown to reduce the overall compressive strength of Portland cement (Harison et al., 2014; Lam et al., 1998). Additionally, the WECC and FFWECC specimens contained a higher proportion of water (45% water:solid) in comparison to Class H specimens (38% water:solid).

Following carbonation of the specimens for 7 days, further increase in the compressive strength of the samples was observed indicating that carbonation under the temperature and pressure conditions tested did not compromise the compressive strength of the specimens. The increase in compressive strength can be linked to the further hydration and pore refinement of the cementitious materials under higher GCS temperatures and pressures. While the FFWCC and Class H showed approximately 8% increase in average compressive strength following carbonation, WECC showed a 30% increase in compressive strength. The difference between the increase in compressive strength for FFWECC and WECC can be linked to the strengthening of the WECC composite due to the densification of the fiber-matrix interface following carbonation, which improves the bonding between the fiber and the matrix and consequently the overall strength of the composite (Adeoye et al., 2019).

It is instructive to note that in addition to exhibiting a higher compressive strength performance in comparison to conventional fly ash-amended wellbore cement, this study has shown that WECC exhibits superior flexural strength and ductility in comparison to FFWECC, furthering it potential as a candidate for wellbore cementing applications.

3.3.5 Evolution of WECC pore structure

The pore structure of wellbore cement can influence the transport of fluids through the uncracked material and thus impact its resistance to CO_2 attack. To illustrate the evolution of WECC's pore structure in response to exposure to CO_2-acidified water, the pore size distribution

curves obtained using MIP are plotted in **Figure 3.6a and Figure 3.6b** for WECC and FFWECC samples, respectively. As shown in **Figure 3.6a**, the total intruded volume in WECC increased from 0.16 mL/g to 0.19 mL/g following 28 days of carbonation, whereas the total intruded volume for the control samples exposed to N_2 headspace remained relatively unchanged at 0.15 mL/g. In the absence of fibers, however, the conventional fly ash-amended wellbore cementing material (FFWECC) showed comparable intruded volumes of approximately 0.14 mL/g for the unaltered and carbonated samples (see **Figure 3.6b**). The total intruded volume for the control FFWECC sample exposed to N_2 headspace also remained constant at 0.14 mL/g after 28 days.

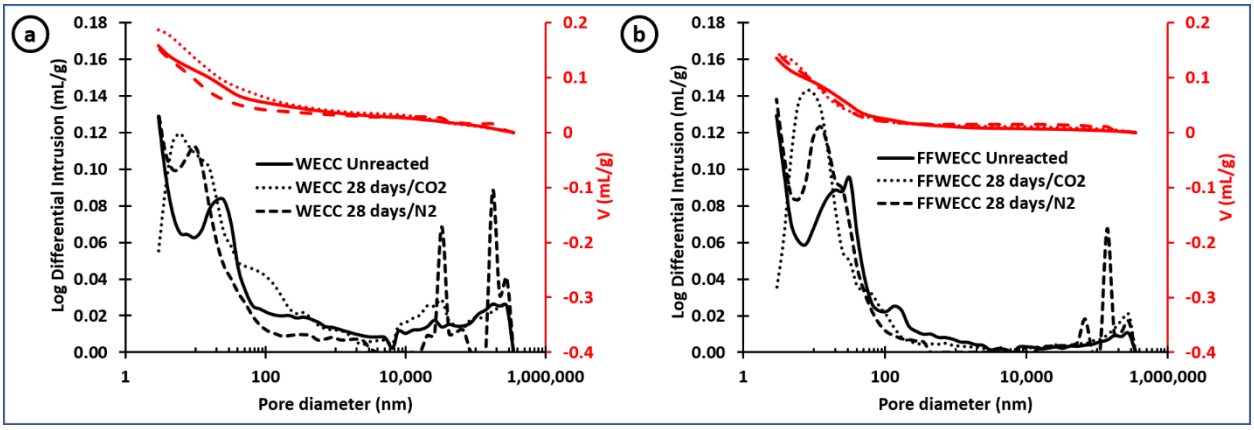

Figure 3.6: Cumulative and differential pore size distribution for unreacted and altered **(a)** WECC and **(b)** FFWECC follow exposure to CO_2-acidified water and N_2 headspace for 28 days at temperature and pressure conditions of 50°C and 10 MPa. The "critical diameter" corresponding pore diameter at the inflection point on the intrusion volume vs. pore diameter curve.

In **Figure 3.6**, the "critical diameter" can be visually identified as the pore diameter at the maximum inflection point on the intrusion volume vs. pore diameter curve (Aligizaki, 2005; Halamickova et al., 1995; Zhang and Shao, 2018). The critical diameter is interpreted as the smallest diameter of the subset of the pores that creates a connected path through the composite matrix (Berodier and Scrivener, 2015; Halamickova et al., 1995; Nishiyama and Yokoyama, 2017;

Zhang and Shao, 2018), and represents the primary connected pores controlling the fluid transport behavior of the composite.

The critical pore diameter decreased from approximately 30 nm in the unreacted specimens, for both WECC (**Figure 3.6a**) and FFWECC (**Figure 3.6b**), to < 20 nm for the control samples exposed to N_2 headspace at a temperature and pressure of 50^{o}C and 10 MPa. This decrease is likely due to continuous hydration and pore refinement under high temperature and pressure conditions. Similarly, carbonation of the samples due to exposure to CO_2-acidified water further decreased the critical pore diameter below 10 nm for both WECC (**Figure 3.6a**) and FFWECC (**Figure 3.6b**) samples. The observation that the post-carbonation critical pore diameters were comparable between the WECC and FFWECC samples indicates that the incorporation of fibers at 1.1% volume will not increase permeation of fluids through uncracked WECC.

To further understand the evolution of pore size based on the intruded volumes and differential pore size distribution curves, the total pore volume was divided into four groups based on pore diameters: voids (>100 nm), large capillary pores (50-100 nm), medium capillary pores (10-50 nm), and gel pores (<10 nm) (Aligizaki, 2005; Zhang and Shao, 2018). The normalized volume fraction of each group with respect to the total pore volume is shown in **Figure 3.7a and Figure 3.7b** for WECC and FFWECC, respectively. It was observed that the volume fraction of voids (pore diameter >100 nm) doubled when PVA fibers were added to the matrix at 1.1% volume in unreacted samples (i.e., for unreacted WECC vs. unreacted FFWECC), carbonated samples, and samples exposed to N_2-headspace. In WECC samples, voids made up 34%, 33%, and 26% of the pore fraction for unreacted samples, carbonated samples, and samples exposed to N_2 headspace, respectively, while the volume fraction of voids in the FFWECC samples exposed to similar conditions was 18%, 14%, and 13%, respectively (**Figure 3.7b**). This indicates that the presence

of the PVA fibers coarsened the pore structure, particularly following exposure to CO_2-acidified water where the volume fraction of voids increased by over 100%.

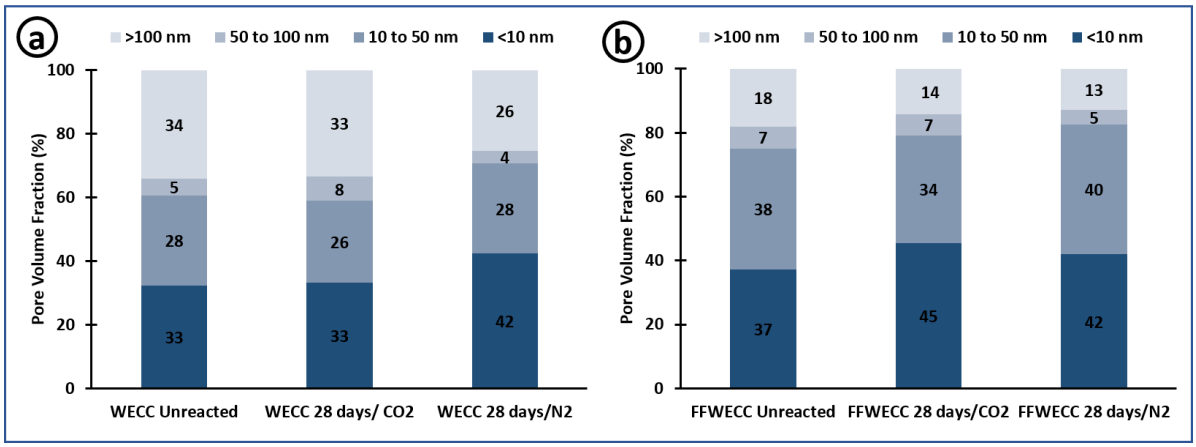

Figure 3.7: Normalized pore volume fraction distribution for unreacted and altered **(a)** WECC and **(b)** FFWECC follow exposure to CO_2-acidified water and N_2 headspace for 28 days at temperature and pressure conditions of 50°C and 10 MPa.

The coarsening of the pore structure following the addition of the PVA fibers can be explained by the existence of the fiber-matrix ITZ in WECC. Analogous to the ITZ between the aggregate and cement paste in conventional concrete, a coarser pore structure is potentially created in the matrix adjacent to fibers due to the "wall effect" that accounts for the increases in the total pore volume and void fractions when the PVA fibers are incorporated. The volume of mercury that intruded along the ITZ is interpreted as the volume for the pore size corresponding to the percolation pressure for the ITZ width. Thus, the presence of the PVA fibers leads to an increase in the fraction of voids in WECC.

Despite the increase in the fraction of voids observed in WECC samples compared to FFWECC samples, it is interesting that the critical diameter of WECC was similar to that of FFWECC samples. This suggests that the coarsening of WECC porosity due to the presence of the

ITZ is unlikely to impact the material permeability, potentially due to isolated distribution and absence of interconnectedness of the ITZ compared to the pores in the matrix. Nevertheless, further investigation is needed to understand the pore structure in WECC using direct observation techniques, such as high-resolution scanning electron microscopy coupled with backscatter electron spectroscopy and x-ray scattering, to examine how this physical change of the pore structure will impact the permeability of WECC to CO_2-rich fluids under CGS conditions.

3.3.6 Evolution of chemical composition

Figure 3.8a and **Figure 3.8b** present the derivative of thermogravimetric analysis (DTG) curves for specimens obtained at different depths along the thickness of WECC and FFWECC coupons following exposure to CO_2-acidified water for 7 days. As presented in the literature, dehydration of calcium silicate hydrate (C-S-H) occurs from 40 to 200^{o}C, dehydroxylation of portlandite ($Ca(OH)_2$) from 380 to 450^{o}C, and decarbonization of calcium carbonate ($CaCO_3$) occurs from 450 to 750^{o}C (Neves Junior et al., 2019, 2015; Sato et al., 2007). Material depths (measured from the outside edge of the sample) of 1 mm and 2 mm represent the fully carbonated zone, the 4 mm and 5 mm sections represent the unaltered zone, while the 3 mm section is the partially carbonated zone, for both WECC and FFWECC samples (see **Figure 3.1d** for schematic). The unaltered 4 mm and 5 mm sections showed comparable trends, with near overlapping DTG curves and similar magnitude for C-S-H, $Ca(OH)_2$, and $CaCO_3$. The 1 mm and 2 mm sections were depleted in $Ca(OH)_2$ but showed a significant increase in the intensity of the $CaCO_3$ peaks as compared to the unaltered sections and the transition zone, indicating the conversion of $Ca(OH)_2$ to $CaCO_3$. Similarly, the intensity of the C-S-H peak decreased progressively from the 1 mm to 5mm section due to partial carbonation of C-S-H.

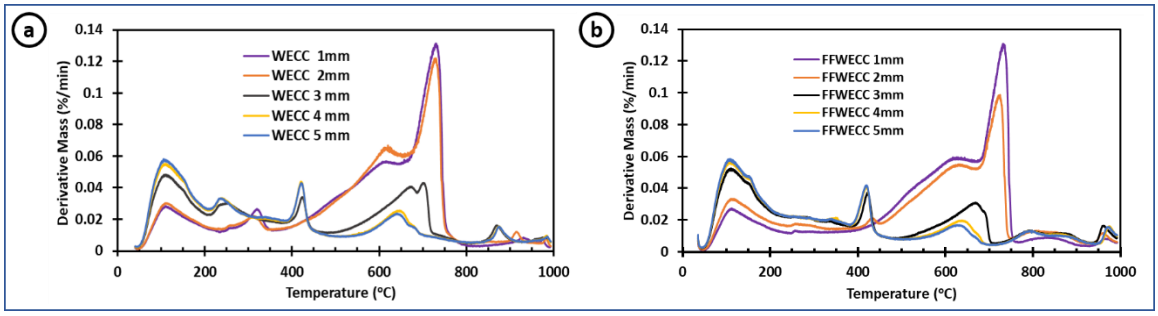

Figure 3.8: DTG curves for **(a).** WECC and (**b).** FFWECC specimens at different depths in the carbonated coupons. The result indicates a decrease in the extent of carbonation of the samples with depth and a significantly higher extent of carbonation at the 1 to 2 mm section of the sample in comparison to the 3 to 5 mm sections. The trend and extent of carbonation for WECC and FFWECC specimens are similar. Note that the 1 mm section is the surface of the sample exposed to the solution while the 5 mm section represents the mid-section of the exposed sample.

For the WECC samples, an additional peak was observed between 225 and 350^{o}C (**Figure 3.8a**). This peak corresponds to the decomposition of the PVA fibers (Panaitescu et al., 2011; Peng et al., 2017; Zhou et al., 2012), which explains its absence in the FFWECC specimens. A progressive shift in the onset of thermal decomposition of PVA fibers can be clearly observed following carbonation, suggesting that the shift is a consequence of the interaction of the fibers with $CaCO_3$. This may be explained by the nucleation of $CaCO_3$ on the fibers following carbonation, as reported by Adeoye et al., (2019), which possibly led to the thermal instability of the fibers. Such shifts in the onset of thermal decomposition, relative to unmodified materials, have been reported in studies on coated fibers and fibers treated with $CaCO_3$ (Al-Sabagh et al., 2018; Bandyopadhyay-Ghosh et al., 2015; Deshmukh et al., 2010; Noor Zuhaira and Rahmah, 2013).

Figure 3.9 presents the normalized percentage of $CaCO_3$ and $Ca(OH)_2$ relative to the total mass loss as a function of temperature at different depths for the WECC and FFWECC specimens. It can be seen that the $CaCO_3$ content in the specimens decreased from 41% and 42% in the most carbonated section to 5% and 7.5% in the unaltered zone for FFWECC and WECC, respectively.

Similarly, the $Ca(OH)_2$ content increased from 0% in the fully carbonated zone to 8.9% in the unaltered zone for both FFWECC and WECC samples. The most significant change in $Ca(OH)_2$ and $CaCO_3$ content occurred between the 2 mm and 3 mm sections. This mirrors the boundary of the carbonation front as determined by use of the phenolphthalein solution (**Figure 3.2**), demonstrating that the pH indicator captured the depth of the alteration front well. The absence of sharp spikes or dips in the $CaCO_3$ content along the altered zone supports previous studies, which showed that exposure to CO_2-acidified water does not result in distinct reaction zones in fly ash-amended cementitious materials, whereas it does in neat Portland cement (Adeoye et al., 2019; Crow et al., 2010; Zhang et al., 2014).

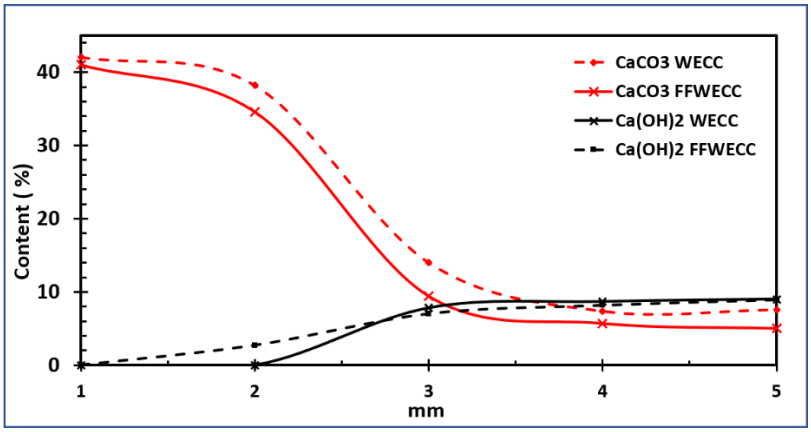

Figure 3.9: Evolution of $CaCO_3$ and $Ca(OH)_2$ content in WECC and FFWECC coupons along the reaction front.

3.4 Conclusion

In this study, a novel strain hardening engineered cementitious composite (WECC) designed for wellbore applications was exposed to CO_2-acidified water at temperature and pressure conditions of 50^{o}C and 10 MPa to investigate the effect of carbonation reactions on its overall mechanical integrity during GCS operations. WECC is proposed here for use in primary cementing of wellbores during GCS because it exhibits tensile ductility superior to conventional wellbore

cement and has the potential to prevent damage to the cement sheath caused by stresses from casing expansion/contraction due to thermal swings during CO_2 injection. The results showed that although the tensile ductility of WECC will decrease following exposure to CO_2-acidified water, it will continue to maintain superior ductility in comparison to conventional wellbore cements under similar conditions. The incorporation of PVA fibers in WECC was found to prevent retrogression of the material hardness, which was not the case for fiber-free conventional fly ash-amended wellbore cement. It was also found that the fibers did not promote deeper depth of CO_2 penetration, as WECC exhibited similar depths of carbonation to that of conventional fly ash-amended wellbore cement at the different time points investigated. Porosity and pore size distribution analysis using MIP showed that while the incorporation of fibers increased the proportion of voids in WECC, the overall trend in porosity and critical pore diameter evolution in WECC was similar to fly ash-amended wellbore cement. This suggests that that the PVA fibers in WECC will not change its permeability significantly in comparison to fly ash-amended wellbore cement. Overall, the high durability exhibited by the novel fiber-reinforced WECC after exposure to CO_2-acidified water may make this material a viable candidate for wellbore cementing applications that aim to prevent cracking of the cement sheath and mitigate upward leakage of stored fluids such as supercritical CO_2.

3.5 References

Adeoye, J.T., Beversluis, C., Murphy, A., Li, V.C., Ellis, B.R., 2019. Physical and chemical alterations in engineered cementitious composite under geologic CO_2 storage conditions. Int. J. Greenh. Gas Control 83, 282–292. https://doi.org/10.1016/j.ijggc.2019.01.025

Aligizaki, K.K., 2005. Pore Structure of Cement-Based Materials : Testing, Interpretation and Requirements. CRC Press. https://doi.org/10.1201/9781482271959

Al-Sabagh, A.M., Abdou, M.I., Migahed, M.A., Fadl, A.M., El-Shahat, M.F., 2018. Influence of surface modified nanoilmenite/amorphous silica composite particles on the thermal stability of cold galvanizing coating. Egypt. J. Pet. 27, 137–144. https://doi.org/10.1016/j.ejpe.2017.02.002

ASTM, 2016. Test Method for Compressive Strength of Hydraulic Cement Mortars (Using 2-in. or [50-mm] Cube Specimens). ASTM International. https://doi.org/10.1520/C0109_C0109M-16A

ASTM, 2012. C1609/C1609M-12. Test Method for Flexural Performance of Fiber-Reinforced Concrete (Using Beam With Third-Point Loading). ASTM International. https://doi.org/10.1520/C1609_C1609M-12

Bachu, S., Celia, M.A., 2009. Assessing the potential for CO2 leakage, particularly through wells, from geological storage sites, in: Geophysical Monograph Series. Am. Geophys. Union Wash. C Pp 203–216.

Bandyopadhyay-Ghosh, S., Ghosh, S.B., Sain, M., 2015. 19 - The use of biobased nanofibres in composites, in: Faruk, O., Sain, Mohini (Eds.), Biofiber Reinforcements in Composite Materials. Woodhead Publishing, pp. 571–647. https://doi.org/10.1533/9781782421276.5.571

Barlet-Gouédard, V., Rimmelé, G., Goffé, B., Porcherie, O., 2007. Well Technologies for CO_2 Geological Storage: CO_2-Resistant Cement. Oil Gas Sci. Technol. - Rev. IFP 62, 325–334. https://doi.org/10.2516/ogst:2007027

Berodier, E., Scrivener, K., 2015. Evolution of pore structure in blended systems. Cem. Concr. Res. 73, 25–35. https://doi.org/10.1016/j.cemconres.2015.02.025

Cao, P., Karpyn, Z.T., Li, L., 2015. Self-healing of cement fractures under dynamic flow of CO_2-rich brine. Water Resour Res 51, 4684–4701. https://doi.org/10.1002/2014WR016162

Carroll, S., Carey, J.W., Dzombak, D., Huerta, N.J., Li, L., Richard, T., Um, W., Walsh, S.D.C., Zhang, L., 2016. Review: Role of chemistry, mechanics, and transport on well integrity in CO_2 storage environments. Int J Greenh Gas Control 49, 149–160. https://doi.org/10.1016/j.ijggc.2016.01.010

Cheshire, M.C., Stack, A.G., Carey, J.W., Anovitz, L.M., Prisk, T.R., Ilavsky, J., 2017. Wellbore Cement Porosity Evolution in Response to Mineral Alteration during CO_2 Flooding. Environ. Sci. Technol. 51, 692–698. https://doi.org/10.1021/acs.est.6b03290

Chow, J.C., Watson, J.G., Herzog, A., Benson, S.M., Hidy, G.M., Gunter, W.D., Penkala, S.J., White, C.M., 2003. Separation and Capture of CO_2 from Large Stationary Sources and Sequestration in Geological Formations. J. Air Waste Manag Assoc 53, 1172–1182. https://doi.org/10.1080/10473289.2003.10466274

Crow, W., Carey, J.W., Gasda, S., Brian Williams, D., Celia, M., 2010. Wellbore integrity analysis of a natural CO_2 producer. Int. J. Greenh. Gas Control, The Ninth International Conference on Greenhouse Gas Control Technologies 4, 186–197. https://doi.org/10.1016/j.ijggc.2009.10.010

Deel, D., 2007. Carbon Sequestration Technology Roadmap and Program Plan 2007 48.

Deshmukh, G.S., Pathak, S.U., Peshwe, D.R., Ekhe, J.D., 2010. Effect of uncoated calcium carbonate and stearic acid coated calcium carbonate on mechanical, thermal and structural properties of poly(butylene terephthalate) (PBT)/calcium carbonate composites. Bull. Mater. Sci. 33, 277–284. https://doi.org/10.1007/s12034-010-0043-7

Dieter, G.E., Bacon, D.J., 1986. Mechanical metallurgy. McGraw-hill New York.

Fabbri, A., Corvisier, J., Schubnel, A., Brunet, F., Goffé, B., Rimmele, G., Barlet-Gouédard, V., 2009. Effect of carbonation on the hydro-mechanical properties of Portland cements. Cem 39, 1156–1163. https://doi.org/10.1016/j.cemconres.2009.07.028

Feldman, R.F., 1987. Diffusion measurements in cement paste by water replacement using Propan-2-OL. Cem. Concr. Res. 17, 602–612. https://doi.org/10.1016/0008-8846(87)90133-5

Gallé, C., 2001. Effect of drying on cement-based materials pore structure as identified by mercury intrusion porosimetry: A comparative study between oven-, vacuum-, and freeze-drying. Cem. Concr. Res. 31, 1467–1477. https://doi.org/10.1016/S0008-8846(01)00594-4

Guillot, D., 1990. 4 Rheology of Well Cement Slurries, in: Nelson, E.B. (Ed.), Developments in Petroleum Science, Well Cementing. Elsevier, pp. 4–1. https://doi.org/10.1016/S0376-7361(09)70302-4

Halamickova, P., Detwiler, R.J., Bentz, D.P., Garboczi, E.J., 1995. Water permeability and chloride ion diffusion in portland cement mortars: Relationship to sand content and critical pore diameter. Cem. Concr. Res. 25, 790–802. https://doi.org/10.1016/0008-8846(95)00069-O

Harison, A., Srivastava, V., Herbert, A., 2014. Effect of Fly Ash on Compressive Strength of Portland Pozzolona Cement Concrete 2, 4.

Huerta, N.J., Hesse, M.A., Bryant, S.L., Strazisar, B.R., Lopano, C., 2016. Reactive transport of CO_2-saturated water in a cement fracture: Application to wellbore leakage during geologic CO2 storage. Int J Greenh Gas Control 44, 276–289. https://doi.org/10.1016/j.ijggc.2015.02.006

IPCC, Metz, B. (Eds.), 2005. IPCC special report on carbon dioxide capture and storage. Cambridge University Press, for the Intergovernmental Panel on Climate Change, Cambridge.

Jen, C.-P., Li, C., Zhang, K., 2017. Effects of Injection Pressure on Geological CO_2 Storage in the Northwest Taiwan Basin. Aerosol Air Qual. Res. 17, 1033–1042. https://doi.org/10.4209/aaqr.2016.12.0526

Kutchko, B.G., Strazisar, B.R., Huerta, N., Lowry, G.V., Dzombak, D.A., Thaulow, N., 2009. CO_2 Reaction with Hydrated Class H Well Cement under Geologic Sequestration Conditions: Effects of Flyash Admixtures. Env. Sci 43, 3947–3952. https://doi.org/10.1021/es803007e

Labibzadeh, M., Zahabizadeh, B., Khajehdezfuly, A., 2010. Early-age compressive strength assessment of oil well class G cement due to borehole pressure and temperature changes 10.

Lam, L., Wong, Y.L., Poon, C.S., 1998. Effect of Fly Ash and Silica Fume on Compressive and Fracture Behaviors of Concrete. Cem. Concr. Res. 28, 271–283. https://doi.org/10.1016/S0008-8846(97)00269-X

Li, Q., Lim, Y.M., Flores, K.M., Kranjc, K., Jun, Y.-S., 2015. Chemical Reactions of Portland Cement with Aqueous CO_2 and Their Impacts on Cement's Mechanical Properties under Geologic CO_2 Sequestration Conditions. Env. Sci Technol 49, 6335–6343. https://doi.org/10.1021/es5063488

Li, V., Wu, C., Wang, S., Ogawa, A., Saito, T., 2002. Interface Tailoring for Strain-Hardening Polyvinyl Alcohol-Engineered Cementitious Composite (PVA-ECC). ACI Mater. J. 99. https://doi.org/10.14359/12325

Li, V.C., 2009. Engineered Cementitious Composites (ECC) – material, structural and durability performance, in: Concrete Construction Engineering Handbook. CRC Press, Boca Raton.

Li, V.C., 2003. On engineered cementitious composites (ECC). J Adv 1, 215–230.

Lye, C.-Q., Dhir, R.K., Ghataora, G.S., 2015. Carbonation resistance of fly ash concrete. Mag. Concr. Res. 67, 1150–1178. https://doi.org/10.1680/macr.15.00204

Michaux, M., Nelson, E.B., Vidick, B., 1990. 2 Chemistry and Characterization of Portland Cement, in: Nelson, E.B. (Ed.), Developments in Petroleum Science, Well Cementing. Elsevier, pp. 2–1. https://doi.org/10.1016/S0376-7361(09)70300-0

Mohamed, M., Li, V.C., 1994. Flexural/Tensile-Strength Ratio in Engineered Cementitious Composites. J. Mater. Civ. Eng. 6, 513–528. https://doi.org/10.1061/(ASCE)0899-1561(1994)6:4(513)

Nelson, E.B., 1990. Well Cementing. Newnes.

Nelson, E.B., Baret, J.-F., Michaux, M., 1990. 3 Cement Additives and Mechanisms of Action, in: Nelson, E.B. (Ed.), Developments in Petroleum Science, Well Cementing. Elsevier, pp. 3–1. https://doi.org/10.1016/S0376-7361(09)70301-2

Neves Junior, A., Dweck, J., Filho, R.D.T., Ellis, B., Li, V., 2019. Determination of CO_2 capture during accelerated carbonation of engineered cementitious composite pastes by thermogravimetry. J. Therm. Anal. Calorim. https://doi.org/10.1007/s10973-019-08210-y

Neville, A.M., 2011. Properties of concrete, 5th ed. ed. Pearson, Harlow, England ; New York.

Nishiyama, N., Yokoyama, T., 2017. Permeability of porous media: Role of the critical pore size. J. Geophys. Res. Solid Earth 122, 6955–6971. https://doi.org/10.1002/2016JB013793

Noor Zuhaira, A.A., Rahmah, M., 2013. Effect of Calcium Carbonate on Thermal Properties of $CaCO_3$/Kenaf/HDPE and $CaCO_3$/Rice Husk/HDPE Composites. Adv. Mater. Res. 812, 175–180. https://doi.org/10.4028/www.scientific.net/AMR.812.175

Nordbotten, J.M., Celia, M.A., Bachu, S., Dahle, H.K., 2005. Semianalytical Solution for CO_2 Leakage through an Abandoned Well. Environ. Sci. Technol. 39, 602–611. https://doi.org/10.1021/es035338i

Nordbotten, J.M., Kavetski, D., Celia, M.A., Bachu, S., 2009. Model for CO_2 Leakage Including Multiple Geological Layers and Multiple Leaky Wells. Environ. Sci. Technol. 43, 743–749. https://doi.org/10.1021/es801135v

Panaitescu, D., Frone, A., Ghiurea, M., Spataru, C., Radovici, C., Iorga, M., 2011. Properties of Polymer Composites with Cellulose Microfibrils, in: Advances in Composite Materials: Ecodesign and Analysis. BoD – Books on Demand.

Peng, S., Zhou, M., Liu, F., Zhang, C., Liu, X., Liu, J., Zou, L., Chen, J., 2017. Flame-retardant polyvinyl alcohol membrane with high transparency based on a reactive phosphorus-containing compound. R. Soc. Open Sci. 4, 170512. https://doi.org/10.1098/rsos.170512

Redon, C., Li, V.C., Wu, C., Hoshiro, H., Saito, T., Ogawa, A., 2001. Measuring and Modifying Interface Properties of PVA Fibers in ECC Matrix. J. Mater. Civ. Eng. 13, 399–406. https://doi.org/10.1061/(ASCE)0899-1561(2001)13:6(399)

Ridha, S., Irawan, S., Ariwahjoedi, B., 2013. Strength prediction of Class G oilwell cement during early ages by electrical conductivity. J. Pet. Explor. Prod. Technol. 3, 303–311. https://doi.org/10.1007/s13202-013-0075-9

RILEM, 1984. CPC-18 Measurement of hardened concrete carbonation depth.

Rimmelé, G., Barlet-Gouédard, V., Porcherie, O., Goffé, B., Brunet, F., 2008. Heterogeneous porosity distribution in Portland cement exposed to CO2-rich fluids. Cem. Concr. Res. 38, 1038–1048. https://doi.org/10.1016/j.cemconres.2008.03.022

Roy, P., Morris, J.P., Walsh, S.D.C., Iyer, J., Carroll, S., 2018. Effect of thermal stress on wellbore integrity during CO_2 injection. Int. J. Greenh. Gas Control 77, 14–26. https://doi.org/10.1016/j.ijggc.2018.07.012

Rutqvist, J., Birkholzer, J., Cappa, F., Tsang, C.-F., 2007. Estimating maximum sustainable injection pressure during geological sequestration of CO_2 using coupled fluid flow and geomechanical fault-slip analysis. Energy Convers. Manag. 48, 1798–1807. https://doi.org/10.1016/j.enconman.2007.01.021

Sato, T., Beaudoin, J.J., Ramachandran, V.S., Mitchell, L.D., Tumidajski, P.J., 2007. Thermal decomposition of nanoparticulate $Ca(OH)_2$-anomalous effects. Adv. Cem. Res. 19, 1–7. https://doi.org/10.1680/adcr.2007.19.1.1

Spycher, N., Pruess, K., 2005. CO_2-H_2O mixtures in the geological sequestration of CO_2. II. Partitioning in chloride brines at 12–100°C and up to 600 bar. Geochim. Cosmochim. Acta 69, 3309–3320. https://doi.org/10.1016/j.gca.2005.01.015

Verbeck, G., 1958. Carbonation of Hydrated Portland Cement, in: Committee C-1, Committee C-9 (Eds.), Cement and Concrete. ASTM International, 100 Barr Harbor Drive, PO Box C700, West Conshohocken, PA 19428-2959, pp. 17-17–20. https://doi.org/10.1520/STP39460S

Watson, T.L., Bachu, S., 2009. Evaluation of the Potential for Gas and CO_2 Leakage Along Wellbores. SPE Drill 24, 115–126. https://doi.org/10.2118/106817-PA

Wu, H.-L., Zhang, D., Ellis, B.R., Li, V.C., 2018. Development of reactive MgO-based Engineered Cementitious Composite (ECC) through accelerated carbonation curing. Constr. Build. Mater. 191, 23–31. https://doi.org/10.1016/j.conbuildmat.2018.09.196

Zhang, D., Shao, Y., 2018. Surface scaling of CO_2-cured concrete exposed to freeze-thaw cycles. J. CO_2 Util. 27, 137–144. https://doi.org/10.1016/j.jcou.2018.07.012

Zhang, D., Shao, Y., 2016. Early age carbonation curing for precast reinforced concretes. Constr. Build. Mater. 113, 134–143. https://doi.org/10.1016/j.conbuildmat.2016.03.048

Zhang, L., Dzombak, D.A., Nakles, D.V., Hawthorne, S.B., Miller, D.J., Kutchko, B.G., Lopano, C.L., Strazisar, B.R., 2014. Rate of H2S and CO_2 attack on pozzolan-amended Class H well cement under geologic sequestration conditions. Int. J. Greenh. Gas Control 27, 299–308. https://doi.org/10.1016/j.ijggc.2014.02.013

Zhang, P., Li, Q.-F., 2013. Combined effect of polypropylene fiber and silica fume on workability and carbonation resistance of concrete composite containing fly ash. Proc. Inst. Mech. Eng. Part J. Mater. Des. Appl. 227, 250–258. https://doi.org/10.1177/1464420712458198

Zhou, K., Jiang, S., Bao, C., Song, L., Wang, B., Tang, G., Hu, Y., Gui, Z., 2012. Preparation of poly(vinyl alcohol) nanocomposites with molybdenum disulfide (MoS 2): structural characteristics and markedly enhanced properties. RSC Adv. 2, 11695–11703. https://doi.org/10.1039/C2RA21719H

CHAPTER 4

Crack Self-Healing in Engineered Cementitious Composite During Geologic Carbon Storage

4.1 Introduction

Geologic carbon storage (GCS) is a potent technology to slow global climate change, but the success of GCS as a carbon mitigation strategy may be compromised by the leakage of CO_2 from storage reservoirs through damaged wellbore cement sheath. In particular, fracture damage of the cement sheath is a major concern as such fractures can act as leakage pathways for CO_2, compromising the long-term storage security of CO_2. A wellbore cement sheath is susceptible to fracture damage due to cyclic stresses generated by varying temperatures and pressures in the wellbore during CO_2 injection operations, natural variations in pressure due to tectonic stresses and seismicity, reaction-induced damage from carbonation of the cement, and damage introduced in the cement sheath during wellbore completion operations (Carroll et al., 2016). Because these stresses are unavoidable during GCS operations, there is a need to understand the potential of fractured cement sheath to self-heal, which could ensure safe and secure storage of CO_2.

Prior studies investigating fracture self-healing in cementitious materials show that the mechanisms for fracture healing include fracture bridging due to hydration of unreacted cement, precipitation of calcium carbonate in the fracture aperture, and swelling of C–S–H and amorphous silica (Edvardsen, 1999; Ramm and Biscoping, 1998; Reinhardt and Jooss, 2003). Self-healing can also occur due to clogging of the aperture with solid impurities in a flowing stream of fluid under advective flow conditions, or through erosion of asperities on the surface of the fracture followed

by smoothing of planar fracture surfaces and subsequent mechanical closure under confining stresses (Carroll et al., 2016; Huerta et al., 2009). In particular, fracture healing due to precipitation of calcium carbonate has been identified as a dominant mechanism for crack healing in conventional wellbore cement sheath during GCS because of the abundance of calcium and carbonate aqueous species in the wellbore cement sheath region.

Prior studies carried out to investigate fracture healing due to mineral precipitation in wellbore cement have evaluated the likelihood of leakage through such fractures and outlined the conditions favorable for self-healing. In a study carried out by Liteanu and Spiers (2011) on chisel-fractured Class A Portland cement cores exposed to a stream of high-purity CO_2 at a temperature of 80^oC and pressure of 10MPa, it was found that 80% of the fracture aperture self-healed after three months due to calcium carbonate precipitation in the cracks, which also led to a noticeable decrease in permeability. In cores retrieved from a 30-year old CO_2- enhanced oil recovery site in West Texas, Carey et al. (2007) reported self-healing of fractures in the core retrieved, which was attributed to filling of the fracture with calcium carbonate. Although the origin of the fractures (i.e. during wellbore completion or CO_2-flooding operation) could not be established, self-healing of the fracture reportedly led to a decrease in the transmissivity of the material. Kjøller et al. (2016) also carried out a CO_2-brine water alternating gas (CO_2-WAG) flow-through experiment on fractured Class G cement. Using pre- and post-reaction micro-computed tomography (µCT) analysis, they showed that the set of fractures traversing the bulk cement had self-healed due to calcium carbonate precipitation, which also reduced the permeability of the core from 200 µD to 100 µD and the pore volume from 0.8% to about 0.5 % over the course of the core-flooding experiment.

Although mineral carbonation is beneficial for autogenous healing in wellbore cement, carbonation promoting self-healing can be limited by factors such as residence time of the fluid in the fracture, fracture aperture width, and the pH of the fluid within the fracture (Cao et al., 2015; Carroll et al., 2016; Huerta et al., 2016). Bachu and Celia (2009) reported that reaction products are continuously eroded in systems with short residence times, inhibiting the capacity of the fracture to heal. Brunet et al. (2016) developed a reactive transport model to determine the impact of fracture aperture and residence time on fracture closure/opening. In numerical experiments of CO_2 flooding, they showed that a strong correlation exists between the fracture width, residence time, and fracture closure. At longer residence times, the slow replenishment of the fluid promoted the precipitation of minerals in the fracture while at shorter residence times, fractures were likely to degrade due to more rapid dissolution. By incorporating prior experimental data from studies carried out by Huerta et al. (2016) and Luquot et al. (2013) into a numerical model, Brunet et al. (2016) showed that self-healing will occur if the residence time of the fluid is at least 30 min for cracks with hydraulic aperture less than 90μm (Brunet et al., 2016; Carroll et al., 2016).

Given the dependence of crack self-healing on crack width, where tighter cracks more readily undergo self-healing, limiting the crack width of damaged wellbore cement sheath to a favorable range for self-healing could further ensure safe and secure storage of CO_2 during GCS. Because such crack width control and prediction is not possible in conventional wellbore cement due to the brittle nature of hardened Portland cement, designing new wellbore cementing materials that can ensure tight crack width when damaged, prevent brittle failure, and consequently promote self-healing will further limit CO_2 leakage during GCS.

Engineered cementitious composites (ECC) are a class of fiber-reinforced cementitious composites with strain hardening behavior and superior tensile ductility in comparison to

conventional wellbore cement (Li, 2009, 2003). ECC exhibits tensile strain capacity of 2 to 5%, which is about 200 to 500 times that of conventional cement mortar and is being proposed here as a substitute for conventional wellbore cement. When subjected to tensile stress, multiple microcracks with crack width less than 60μm are generated and are bridged by microfibers that can act as nucleation sites for self-healing products (Herbert and Li, 2013; Kan et al., 2010; Li and Herbert, 2012). Such controlled tight crack width, which is not possible in conventional wellbore cement, makes ECC unique in comparison to conventional wellbore cement and a prime candidate for self-healing wellbore cementing material.

In **Chapter 3** where ECC was exposed to CO_2-acidified solutions under GCS temperature and pressure conditions, it was observed that ECC continued to maintain significantly higher ductility than conventional wellbore cement after several weeks of exposure to CO_2-acidified water. Additionally, the carbonation of the ECC coupons led to an increase in the flexural strength of the material due to the densification of the fiber/matrix interface. We also found that the ECC showed greater resistance to deformation and material loss following its reaction with CO_2 in comparison to typical fly ash-amended wellbore cement composition. Additionally, the overall transport through the material decreased due to continued pore refinement from pozzolanic reactions and precipitation of calcium carbonate within the pores and the fiber-matrix ITZ. While prior studies including Li and Herbert (2012), Li and Yang (2007), and Yang et al. (2009) have shown that conventional ECC undergoes autogenous self-healing following multiple wetting and drying cycles, it is important to investigate the possibility for such crack healing in ECC utilized for wellbore cementing during GCS. Furthermore, since CO_2 injection wells will be exposed to multiple injection cycles during their operating life, which will lead to cyclic stresses in the wellbore cement sheath, it is important to know if damaged ECC can undergo cyclic self-healing.

The implications of self-healing on the overall mechanical integrity and permeability of the ECC cement sheath will be a key factor for ensuring the secure storage of CO_2 in such reservoirs.

In this chapter, the potential for self-healing in ECC proposed for wellbore cementing applications during GCS was investigated. Specimens were pre-stressed to generate microcracks in the samples and were subsequently exposed to multiple CO_2-rich environments to examine the potential for self-healing of these microcracks. Crack healing was explored by tracking crack patterns in the specimens using an optical microscope, and permeability changes in the specimens were evaluated using a constant head permeability test. This work further provides insight into the performance of ECC as a substitute wellbore cementing material for newly constructed wells during GCS.

4.2 Materials and Methods

4.2.1 Material selection

Table 4.1 presents the composition of the material used in this study based on the proportions of the constituents relative to the total weight of the solid components. Materials were selected to produce a composite that exhibits multiple microcracking behavior and steady-state crack width below 100 μm during the strain-hardening phase. This is vital as prior work has shown that cracks must be below 150 μm to self-heal, and preferably below 50 μm for complete self-healing (Li and Yang, 2007; Yang et al., 2009). Samples were prepared using Type III ordinary Portland cement and Class F fly ash with chemical composition presented in **Table 3.1**. Because the high water content of the mix can have a negative impact on the quality of the wellbore cement and potentially lead to inconsistencies in the mechanical behavior of the specimens, a low proportion of silica fume was incorporated into the ECC mix to reduce free-water. In contrast to the ECC composition presented in **Chapter 3** that utilized PVA fibers with 0.5% oil coating, fibers with 1.2% oil coating

were used in this study as increased fiber coating can limit the densification of the fiber/matrix interfacial bond properties following carbonation. Antifoam and antisettling agent amounting to 0.4% of the solid weight of the mixture were added to reduce foam formation and water loss, respectively. Dispersant and super plasticizer were also added at 0.5% weight of the solid components to control the rheology of the slurry in the fresh state. Class H cement was prepared as described in **Chapter 3**.

Table 4.1: Composition of materials used for sample preparation. Water content is reported as a fraction of the total solid weight.

Sample Type	Solid Phase			Liquid phase	Fiber vol. (%)
	Cement	Fly ash	Silica fume	Water	
ECC	0.4	0.5	0.1	0.40	1.5
Class H	1.0	-	-	0.38	-

Note: Additives including dispersant, antifoam, antisettling agents, and high range water reducer were added to ECC to modify slurry fresh state flow properties.

4.2.2 Sample Preparation

Solid components were dry-mixed in a countertop force-based Hobert mixer (KitchenAid) for 5 minutes and the pre-mixed liquid components (i.e. water, water reducer, antifoam, and super plasticizer) were added to the solid components and mixed for additional 5 minutes. After achieving a consistent mix, PVA fibers were added to the slurry at a steady rate for 1.5 minutes, and the slurry was further homogenized for an additional 1.5 minutes. The fresh slurry was cast in dogbone molds (**Figure 4.1a**) coated with WD-40 liquid to ensure damage-free demolding of the specimens. Following casting, the specimens were placed in a curing chamber (Temp. = 22 ± 2^{o}C and Rel. Humidity = 99 ± 1%) and demolded after 24 hours. The demolded specimens were subsequently placed in the curing chamber for 28 days.

4.2.3 Uniaxial tensile strength assessment

A uniaxial tensile test was carried out on the dogbone-shaped samples, using the Japan Society of Civil Engineers (JSCE) high-performance fiber-reinforced cementitious composite testing method (JSCE, 2008), to generate microcracks in the dogbone specimens and determine their tensile strengths and tensile strain capacities. The test was done using an Instron mechanical test frame equipped with data acquisition software (Instron–Bluehill) and the samples were hoisted via wedging in the test frame holders as shown in **Figure 4.1b**. Two linear variable displacement transducers (LVDT) were attached to the sample holder to capture the total deformation in the system over a strain gauge length of ~70 mm, and the alignment of the specimens in both vertical and horizontal directions was ensured using a level. The samples were subsequently loaded at a rate of 0.5 mm/min until a tensile strain percentage of 1% was achieved. 1% strain capacity was chosen as a reasonable pre-strain condition to generate multiple micro-cracks for characterization while preventing excessive damage to the material. It should be noted that 1% tensile strain is comparable to about 100 times the strain capacity of conventional wellbore cement and thus is significantly larger than the design tensile strain capacity for wellbore cement. The samples were then unloaded and retrieved for further testing.

To determine the crack count of each specimen, an infinity X-C21 microscope camera with a resolution of 1µm (Lumenera Corporation) was used to count the total visible cracks along the top, center, and bottom sections of the 70 mm strain gauge length of each dogbone specimen. The specimen crack count was then estimated by taking the maxima of the number of cracks along the three linear sections drawn along the strain gauge length for each specimen. While this approach may underestimate the total crack count in the sample, as several cracks do not span the whole width of the specimen, defining the crack count as the maximum crack count along the three linear

sections prevents double counting of cracks. The crack density of the specimens was then calculated as a function of the number of cracks along the 70 mm strain gauge length of the specimens divided by the strain gauge length (cracks/mm). The average crack width was also determined by measuring the widths of several cracks along the mid-section of the cracked specimen and taking the average.

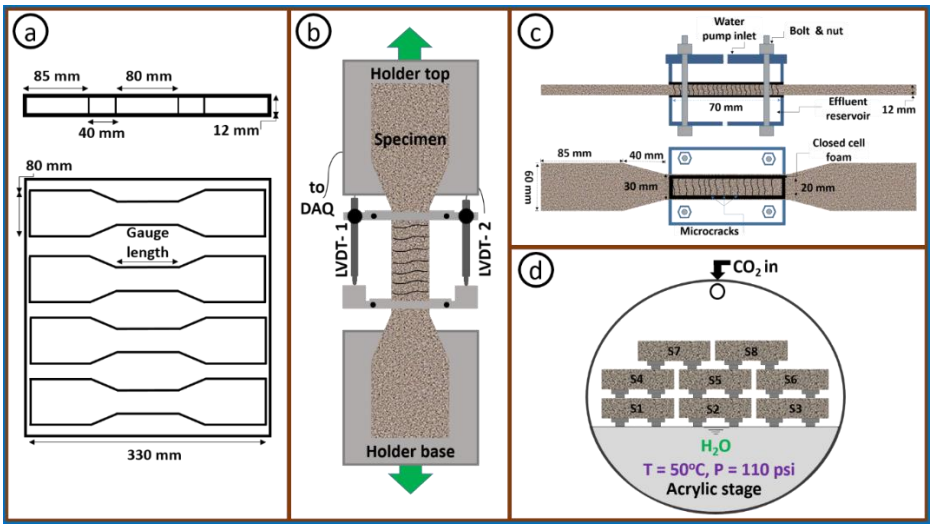

Figure 4.1: **(a)** Aluminum molds used to prepare the dogbone specimens showing the dimensions of the different sections, **(b)** Dogbone molds under uniaxial tensile load. Linear variable displacement transducers (LVDT) were used to capture the linear extension of the specimen relative to tensile stress, **(c)** Customized test cell for permeability measurement along the mid-section of the specimen. The top section presents the front view of the cell while the lower section is the top view, and **(d)** Front view of the carbonation keg showing the arrangement of several dogbone specimens in the keg.

4.2.4 Permeability test

Post-crack and post-self-healing permeability of the cracked 70 mm section of each dogbone specimen were determined via a constant head permeability test using customized test cells designed from clear 0.5-inch thick acrylic plates, as shown in **Figure 4.1c**. Specimens were prepared by sealing off the vertical sides using removable adhesive tapes to ensure unidirectional flow of water through the cracks. The upper and lower contact surfaces of the permeability test cell with the specimens were fitted with 1/8-inch thick single-sided closed cell foam strips to

enhance the water seal at the coupon/permeability cell contact surface. The samples were subsequently secured between the upper and lower halves of the test cells using hexagonal nuts on both sides of the cell. A constant head permeability test was used in this study instead of a falling head permeability test because the constant pressure head mirrors the hydrostatic condition near the wellbore in geologic formations and enables faster measurements of specimen permeability. The pressure in the upstream section of the cell was raised to 0.08 MPa (12 psi), which corresponds to ~8.4 m of hydraulic head relative to atmospheric pressure, and was held constant for 300 s. Water flowing through the cracked specimen over the period of 300 s was collected at the bottom of the cell and measured to determine the volumetric flow rate. The permeability coefficient (K_f) and absolute permeability (k) of each specimen were calculated using **Eq. 4.1** and **Eq. 4.2**, respectively:

$$K_f = \frac{VL}{A\, h_0\, t_f} \qquad \textbf{Eq. 4. 1}$$

$$k = \frac{K_f \eta}{\rho g} \qquad \textbf{Eq. 4. 2}$$

where k_f is the coefficient of permeability (m/s), k is the absolute permeability (m^2), V is the volume of water that passed through the specimen thickness test (m^3), L is the thickness of the specimen in the direction of flow (m), A is the cross-sectional area of the specimen subjected to flow (m^2), h_o is the constant hydraulic head (m), t_f is the total time of flow (s), η is the dynamic viscosity of water (kg/m.s), ρ is the density of water (kg/m^3), and g is the acceleration due to gravity (m/s^2) (Freeze and Cherry, 1979; Lepech and Li, 2009; Wang et al., 1997). The cross-sectional area of flow for each sample was 22 mm x 70 mm (1.54×10^{-4} m^2) and the thickness of each specimen was 12 mm (1.2×10^{-2} m).

4.2.5 Carbonation experiments

Two sets of carbonation experiments were carried out in this study. First, low-pressure experiments using 5-gallon carbonation kegs **(Figure 4.1d)** were conducted to investigate the potential for crack healing in ECC and the impact of such healing on its mechanical integrity and permeability. The pressure condition for the low-pressure studies (0.75 MPa) was selected based on pressure limitations of the carbonation vessels. The second set of experiments was a combination of high-pressure and low-pressure experiments conducted in two 600 mL static batch reactors. The objective of the study was to determine the differences between crack-healing behaviors and permeability alteration trends in the high-pressure environment relative to the low-pressure system. The high-pressure environment simulates wellbore cement sheaths exposed to CO_2-acidified water and supercritical CO_2. The test conditions for each experiment are specified in **Table 4.2** and the schematic representations of the cement sheath locations these experiments represent are presented in **Appendix Figure C5.**

In the low-pressure experiments, pre-stressed dogbone specimens were exposed to four different environments in 5-gallon carbonation kegs. The experiments were carried out at temperature and pressure of 50^{o}C and 0.75 MPa (110 psi), respectively, and specimens were retrieved after 28 and 56 days for further analysis. In the first vessel (SH-CO2-H2O), several dogbone specimens were submerged horizontally in DI water, achieving a water-to-solid ratio of ~3:1. This exposure condition represents cement in constant contact with CO_2-acidified water near the downhole region of the well. For the second test condition (SH-CO2-G), ECC dogbone specimens were stacked on an acrylic platform with the specimens separated using plastic studs. The bottom of the keg was then filled with DI water such that the water did not come into contact with the specimens, and the temperature and pressure were elevated to 0.75 MPa and 50^{o}C,

respectively. This exposure condition simulates the environment near the caprock where the wellbore cement sheath may be exposed to wet CO_2 gas. For the third test condition (SH-CO2-GNaCl), the samples were exposed to CO_2 under similar conditions as SH-CO2-G but the vessel was filled with 1 M NaCl solution instead of DI Water. Control experiment were also set up in which pre-stressed dogbone specimens were exposed to place in the curing chamber for the duration of the carbonation experiments. These control specimens were not carbonated.

After 28 days of reaction, samples were retrieved from the reactors to evaluate crack closure and permeability evolution in order to understand the effectiveness of the self-healing process. Two specimens were then re-strained to 0.5% tensile strain, simulating ECC subjected to cyclic stress during GCS. The re-strained samples were exposed to CO_2 in the carbonation kegs for an additional 28 days to promote further self-healing. The specimens were subsequently retrieved for further optical microscopy and permeability analysis, and strained to failure to determine their residual tensile strain capacity and tensile strength.

For the high-pressure experiments, a cracked coupon specimen with dimensions of 80 mm x 30 mm x 12.7 mm was placed in the reactor and fully submerged in DI water to achieve a water: solid ratio of 8:1. A second coupon was also placed in the headspace in the reactor. Subsequently, the temperature and CO_2 pressure (P_{CO2}) were elevated to 50^{o}C and 10 MPa (~1450 psi), respectively. In the second batch reactor, specimens were placed similarly in both CO_2-acidified water and CO_2 gas. However, the reactor pressure was only elevated to 0.75 MPa (~110 psi) to serve as control for the high-pressure batch experiments and to compare with the low-pressure experiments conducted in the carbonation kegs. The specimens were exposed to the CO_2-rich environment for 4 weeks and subsequently analyzed to investigate the extent of crack healing and permeability alteration under each of the test conditions.

Table 4.2: Experimental conditions for low-pressure and high-pressure experiments. Note that all carbonation experiments were carried out at temperature of 50°C.

	Exposure condition	Fluid	Pressure (MPa)	Duration (days)
Low pressure experiments using pre-stressed ECC dogbone specimens				
SH-CO2-H2O	CO_2-acidified water	DI water	0.75	56
SH-CO2-G	CO_2-gas headspace	DI water	0.75	28,56
SH-CO2-GNaCl	CO_2-gas headspace	1M NaCl solution	0.75	8
SH-Control	Curing chamber	Moisture	-	56
High-pressure and low-pressure experiments using ECC coupons				
HP-CO2-H2O	CO_2-acidified water		10	28
HP-CO2-G	Wet supercritical CO_2		10	28
LP-CO2-H2O	CO_2-acidified water		0.75	28
LP-CO2-G	Wet CO_2 gas		0.75	28

4.3 Results and Discussion

4.3.1 Crack characteristics and mechanical properties

Table 4.3 presents the crack properties of specimens pre-stressed to 1% tensile strain prior to reaction with CO_2. The average crack count was 18 with a standard deviation of 3, which represents a crack density of 0.26 cracks/mm. Previous studies by Liu et al. (2016) and Zhang et al. (2019) have reported crack counts for conventional ECC Mix within two standard deviations of the average crack count reported here for conventional ECC subjected to 1% tensile strain. Because the conventional ECC mix (Li, 2009, 2003) is compositionally different from the ECC mix here, largely because of higher fiber volume and incorporation of silica sand in conventional ECC, a direct comparison cannot be made between the conventional ECC and the mix used in this study.

However, the ability to achieve multiple microcracking behaviors in the specimens indicates that the material performs similarly to conventional ECC.

Table 4.3: Crack characteristics of specimens following direct tensile stress at 1% tensile strain.

	Avg. Cr.	**STDV Cr.**	**Max. Cr.**	**Min. Cr.**	**Modal Cr.**
Crack Count	18	3	22	10	19
Width (μm)	16	2	95	3	6

At 1% tensile strain, the average residual crack width and modal crack width were 16 mm and 6 mm, respectively, which is within the range of crack widths that have been shown to undergo self-healing in previous studies carried out using conventional wellbore cement (Brunet et al., 2016; Carroll et al., 2016) and can promote self-healing of the specimens when exposed to CO_2. For specimens strained to failure prior to carbonation, the average crack count along the 70-mm strain gauge length was 42 cracks, which represents a crack density of 0.6 cracks/mm. The average residual crack width was 16 μm, which is similar to the crack width of specimens following uniaxial tensile loading to 1% tensile strain after 28 days of curing in a 99% RH chamber.

Figure 4.2 presents the initial stress-strain relationship for the ECC and Class H cement under uniaxial tensile loading after 28 days of curing in a 99% RH chamber. The tensile strain capacity of ECC was ~3.1%, which is 310 times that of conventional Class H cement (tensile strain capacity of 0.01%). While previous studies have described ECC with greater tensile strain capacity than the samples tested here (Wu et al., 2018; Zhang et al., 2017), the fact that the fiber volume was limited to 1.5% contributed to the lower tensile strain capacity in comparison to the conventional mix. The ultimate tensile strength of ECC was 3.4 MPa while that of the Class H mortar was 0.9 MPa, demonstrating that the ECC material exhibits both superior tensile strength and tensile strain capacity relative to conventional wellbore cement. Because Class H cement exhibited brittle failure

with a single crack in the specimen, which cannot be evaluated for self-healing using our approach or in comparison to ECC, no further analysis was carried out for crack healing in Class H cement. The 24-hr compressive strength of the ECC material was 10.1 MPa, which exceeds the API recommended minimum compressive strength of 3.5 MPa for wellbore cementing applications. The 28-day compressive strength of the specimen was 34.4 MPa.

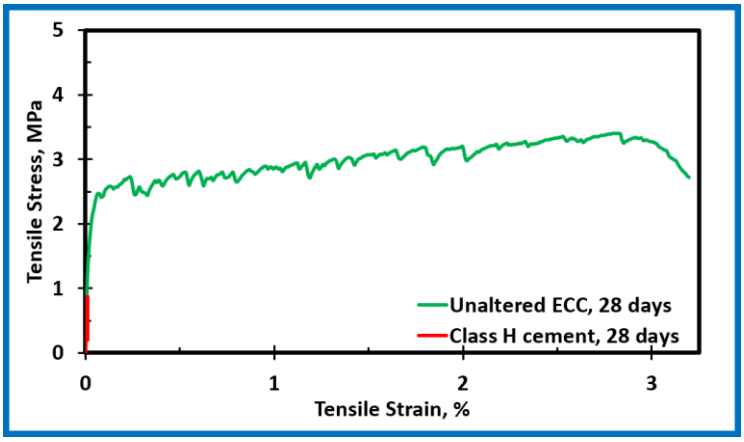

Figure 4.2: Tensile stress-strain curve for ECC specimen and conventional Class H wellbore cement after 28 days of curing.

4.3.2 Crack healing in carbonated ECC

Crack characterization carried out to investigate the potential for self-healing in ECC following exposure to CO_2 under various environmental conditions showed that self-healing will occur, but cracks with similar characteristics exposed to the same conditions may exhibit differing extents of healing in the short term. For specimens exposed to CO_2-acidified solutions at 50^{o}C and 0.75 MPa (SH-CO2-H2O), surficial crack closure was not observed after 28 days of reaction, so the specimens were re-exposed to CO_2 for an additional 28 days to determine if longer contact time could promote crack healing. After 56 days, external crack closure was observed in several sections of the specimens, although some cracks did not show surficial self-healing. **Figure 4.3a** and

Figure 4.3b present optical images of the section of a cracked specimen before and after 56 days of exposure to CO_2-acidified water. A crack with a width of 17 µm, which is approximately the average crack width at 1% strain, was clearly filled due to self-healing (**Figure 4.3b**). **Appendix Figure C.6a and Appendix Figure C.6b** also presents a self-healed crack with initial aperture of ~32 µm, which corresponds to twice the size of the average crack aperture at 1% strain, indicating that cracks below 30 µm can self-heal when exposed to CO_2-acidified solution under the test conditions. In addition to the cracks that exhibited self-healing, several unhealed cracks with similar widths as the self-healed cracks were observed on the surface of the specimens (**Appendix Figure C.7a and Appendix Figure C.7b**). Because the specimens were exposed to the same environmental conditions as the self-healed cracks, the reason for varying extents of healing in similar cracks is not fully understood. However, it is likely due to the fact that some cracks achieve faster closure earlier than others due to local variations in the structural characteristics of the cracks and the chemical composition near the crack vicinity. Additionally, the fact that the reactor was not stirred may have led to greater extent of buffering and higher pH conditions in sections of the reactor, promoting surficial self-healing of some cracks.

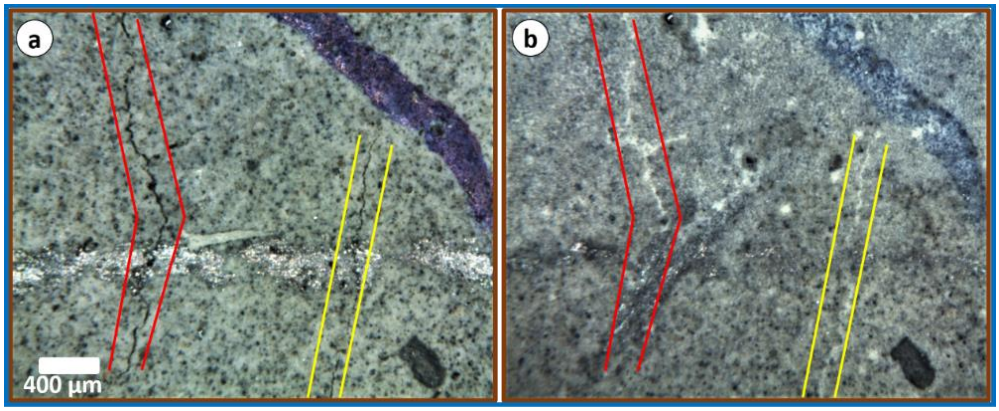

Figure 4.3: Optical image showing microcracks **(a).** prior to reaction and **(b).** after self-healing following exposure to CO_2-acidified water at temperature of 50°C and pressure of 0.75 MPa. The red and yellow brackets highlight cracks pre-carbonation and post-self-healing.

Figure 4.4 shows the pre-reaction and post-reaction optical images of the cracked section of specimens exposed to water-saturated CO_2 headspace (SH-CO2-G). After 28 days of carbonation, crack healing was observed in several sections of the specimens as the crack aperture appeared to be filled with newly formed material **(Figure 4.4b).** However, the healing process was not efficient, as multiple cracks of the same size did not self-heal over the same period. After exposing the specimens to CO_2 for an additional 28 days**,** further crack healing was observed in comparison to the 28-day healing extent (**Figure 4.4b)**. This suggests that the healing process is progressive and time-dependent, where the extent of crack healing increases with continued exposure. Since specimens in the water-saturated CO_2 headspace were exposed to a more uniform chemical condition relative to the specimens in CO_2-acidified water in which transport limitations likely existed under static batch conditions, the variation in the extent of healing of similar cracks is not likely impacted by inter-specimen exposure conditions and environmental chemical gradients. In contrast to specimens exposed to CO_2-acidified water, where a distinct white precipitate was observed in several healed cracks, specimens exposed to the CO_2 headspace showed either partial or complete closure of cracks without the prominent white precipitate. The difference in the appearance of the healing products is likely due to the mode of formation of the healing products under such conditions. In the samples exposed to CO_2-acidified solution, it is likely that there was initial dissolution of the calcium-rich matrix, due to the acidic conditions of the acidified water, followed by precipitation of calcium carbonate in the microcracks. However, for specimens exposed to the CO_2 headspace, the calcium carbonate likely precipitated in place over time with minimal transport of the aqueous species.

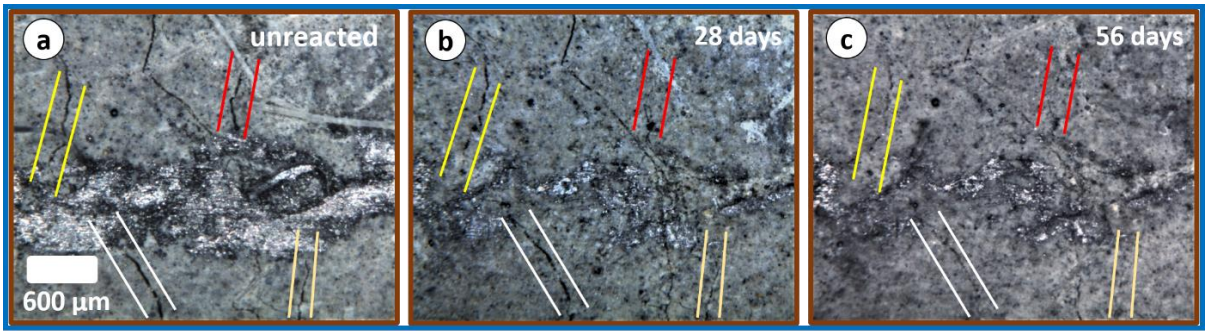

Figure 4.4: **(a)** Optical image of uncracked ECC before exposure to CO_2, **(b)** Cracked specimen after exposure to water-saturated CO_2 headspace for 28 days with evidence of crack healing , and (C) Cracked specimen after 56 days with further crack healing in comparison to the 28 day crack healing. Brackets of similar colors highlight cracks at different time points.

Similar to specimens exposed to CO_2 headspace in the presence of deionized water, specimens exposed to water-saturated CO_2 headspace in the presence of 1M NaCl solution (SH-CO2-G_{NaCl}) did not exhibit significant surficial crack healing in all cracks after 8 days, except for minimal attenuation of some microcracks. However, the pH indicator test showed that the specimens had been fully carbonated after 8 days of reaction. This further supports the hypothesis that carbonation of ECC is not the dominant driving mechanism for crack healing as complete crack healing was not observed although the specimens were fully carbonated. Alternatively, ECC carbonation may be a contributor to crack healing but is a gradual process that requires a longer timeframe to promote noticeable self-healing. Because the experiment was terminated after 8 days of CO_2 exposure, as the 1M NaCL solution negatively impacted the integrity of the thin-walled pressure vessel, we were unable to evaluate the long-term potential for self-healing under this condition.

For pre-stressed uncarbonated control specimens that were continuously cured at 99% RH for 56 days, self-healing was observed in several cracks. The maximum crack width that healed was ~32 µm (**Appendix Figure C.8a, Appendix Figure C.8b, and Appendix Figure C.8c)**, which is similar to the maximum crack width that exhibited self-healing after exposure to CO_2-acidified water. Similar to the sample exposed to the wet CO_2 environment, the material in the bridged crack

had the same texture and hue as the surrounding cementitious material, which suggests that the newly formed material occurred due to continuous hydration of the composite and swelling of the C-S-H in a high-RH environment. This is because the cementitious composite intrinsically contains “micro-reservoirs” of unhydrated cement particles that are widely dispersed in the matrix and available for self-healing due to the addition of fly-ash as a pozzolan in ECC (Li and Yang, 2007). The appearance of crack bridging under the three test and control conditions highlighted in this study indicates that crack-healing will progress autogenously in ECC provided there is continuous interaction with an aqueous environment, as is expected in wellbore cement sheaths under GCS conditions.

4.3.3 Long-term permeability alteration in ECC

Table 4.4 presents the permeability of the pre-carbonated specimens at 1% tensile strain and post-exposure to CO_2 under the different environmental conditions tested in this study. Although complete surficial crack closure was not observed in all the specimens, as discussed in **Section 4.4.2**, significant permeability decrease occurred under all exposure conditions after several weeks of reaction. This suggests that the absence of surficial crack closure does not prove the absence of self-healing in ECC.

For specimens exposed to CO_2-acidified water (SH-CO2-H2O), the initial permeability of the specimens ranged from 1.2 mD to 4.2 mD at 1% strain. Because surficial crack closure was not observed in most of the cracks after 28 days of reaction, the permeability of the specimens was not tested at this point. After 56 days, the permeability of the specimens could not be determined under the initial test conditions because flow did not occur through the healed section of the specimens, even after further testing for 6 hrs using the same hydraulic head as the initial test condition. This suggests that while the cracked specimens did not exhibit complete surficial healing, the interior

of the cracks had undergone significant alteration and healing that prevented the flow of water. The apparent preferential internal healing of the cracks can be explained by increased buffering in the interior of the samples compared to the exterior, which favors precipitation of calcium carbonate and formation of other healing products (Cao et al., 2015).

Table 4.4: Permeability of cracked dogbone specimens measured at different time points and under various exposure conditions. See footnote for specimen descriptions.

Specimen	$K_{o\text{-}1\%}$ (mD)	$K_{28\ days}$ (mD)	$\Delta k_{28\ days}$ (%)	$K'_{28\ days\text{-}0.5\%}$ (mD)	$K_{56\ days}$ (mD)	$\Delta k_{56\ days}$ (%)
SH-CO2-H2O						
1	2.1	-	-	-	Impermeable	-
2	3.0	-	-	-	Impermeable	-
3	4.2	-	-	-	Impermeable	-
4	1.2	-	-	-	Impermeable	-
SH-CO2-G						
1	15.8	2.1	-86.7	7.9	1.8	-77
2	3.7	2.1	-43.2	5.6	2.3	-59
3	18.5	8.8	-52.4	-	5.9	-33
4	10.6	4.8	-54.7	-	2.9	-40
SH-CO2-G_{NaCl}*						
1	3.8	2.5	-34.2	-	-	-
2	1.3	0.6	-53.8	-	-	-
3	4.1	1.7	-58.5	-	-	-
4	8.4	7.3	-13.1	-	-	-
Un Carbonated**						
1	2.9	2.8	-4.0	-	-	-
2	7.9	7.6	-3.7	-	-	-
3	17.6	8.5	-51.7	-	3.5	-59
4	24.9	14.7	-41.2	-	12.6	-46

Specimen description: See Table 4.2 for sample descriptions. $K_{o\text{-}1\%}$ is the permeability at 1% tensile strain, $K_{28\ days}$ is the permeability after 28 days of carbonation, $K'_{28\ days\text{-}0.5\%}$ is the permeability of carbonated sample restrained to .5% tensile strain, and $K_{56\ days}$ is the permeability of the samples after 56 days of carbonation. $\Delta k_{28\ days}$ is the percentage change in permeability after 28 days of carbonation relative to $K_{o\text{-}1\%}$. $\Delta k_{56\ days}$ is the percentage change in permeability relative to the permeability after 28 days of carbonation.
*Permeability was measured after 8 days because the experiment was terminated.

For samples exposed to CO_2 headspace (SH-CO2-G), a decrease in the permeability of the specimens was observed following carbonation. However, the extent of permeability decrease was

less significant than the decrease observed in specimens exposed to CO_2-acidified water as the final permeability was measurable using the initial test conditions. The difference in the initial permeability of the specimens, which ranged from 3.7 mD to 18.5 mD, in comparison to the initial permeability of the specimens exposed to CO_2-acidified water is due to the inter-sample variations in maximum crack width and crack count. Prior study has shown that the permeability of cracked ECC increases linearly with crack count and cubically with crack width (Liu et al., 2016). After 28 days of carbonation, the permeability of the SH-CO2-G specimens decreased significantly (up to 87%). After further exposure to CO_2 for 56 days, an additional decrease in permeability was observed even though the specimens had been fully carbonated after the initial 28 days based on the pH indicator analysis. This further decrease in permeability that mirrors the continuous attenuation of cracks discussed in **Section 4.4.2**. shows that crack healing in ECC is a continuous process and the extent of healing is time-dependent. Similarly, specimens re-exposed to CO_2 for 28 days after being re-stressed to 0.5% tensile strain following the initial 28-day carbonation cycle demonstrated permeability decrease up to 77% (relative to the permeability at 0.5% tensile strain). Because the primary mechanism of permeability decrease is through crack closure and healing, this result suggests that a wellbore cement sheath completed using ECC can exhibit cyclic crack healing following exposure to cyclic downhole stresses during GCS.

For the specimens exposed to CO_2 headspace in 1M NaCl solution (SH-CO2-G_{NaCl}), the initial permeability ranged from1.3 mD to 8.4 mD. Although the specimens were reacted for only 8 days, the permeability decreased by up to 60% during the exposure period. Thus, while permeability changes in ECC are progressive, significant changes can occur over a short period of time. Because the experiment was terminated after 8 days, further permeability analysis was not feasible. For control specimens exposed to 99% RH for 28 and 56 days, some specimens showed modest change

in permeability (3-4%) while others showed significant permeability alteration comparable to the carbonated specimens **(Table 4.4)**.

The fact that specimens exposed to CO_2 headspace were fully carbonated after 28 days but showed significant permeability decrease following further reaction for 28 days, while uncarbonated control specimens decreased in permeability after 28 and 56 days, confirms the hypothesis that the process of permeability alteration and crack healing in the ECC specimens is not primarily driven by carbonation. Other mechanisms of crack healing that impacted the permeability include further hydration of the composite and swelling of the C-S-H in a moist environment (Edvardsen, 1999; Ramm and Biscoping, 1998; Reinhardt and Jooss, 2003; Yang et al., 2009), which contributed to the crack closure observed in the uncarbonated control specimens.

4.3.4 Evolution of tensile performance

To investigate the long-term tensile performance of ECC following exposure to CO_2 under different conditions, the relationship between tensile stress and tensile strain was tracked for the specimens pre- and post-carbonation using uniaxial tensile tests. As discussed in **Section 4.4.1,** the tensile strain capacity and tensile strengths of the unaltered ECC specimen prior to reaction with CO_2 were 3.1% and 3.4 MPa, respectively. After reaction with CO_2 under different exposure conditions, the results indicate that the tensile strength and tensile strain capacity of ECC was altered noticeably, but the extent of alteration is dependent on the exposure condition (**Table 4.5)**.

Figure 4.5a presents the uniaxial tensile stress-strain curves for uncarbonated ECC (SH-Controls) at 1% tensile strain after 28 days of curing and at failure after further curing for 56 days.

Table 4.5: Mechanical properties of carbonated and uncarbonated ECC specimens measured at different time points and exposure conditions. Acronyms and terms are defined in the footnote.

	T. St., pre, 1% (MPa)	**T. St., 28 days, 0.5% (MPa)**	**T. St., 56 days (MPa)**	**ΔT. St., 8 days, 0.5% (%)**	**ΔT. St., 56 days (%)**	**T. Strain at failure (%)**
SH-CO2-H2O						
S1	3.2	-	4.3	-	35	2.6
S2	2.7	-	3.8	-	41	2.4
SH-CO2-G						
S1	2.6	3.8	4.2	47	62	1.7
S2	2.9	3.8	4.4	31	50	1.3
SH-CO2-G_{NACL}*						
S1	3.0	-	3.8	-	28	1.6
S2	3.5	-	3.9	-	13	1.7
SH-Control-Uncarbonated						
S1	2.9	-	3.6	-	21	2.2
S2	2.9	-	3.3	-	15	2.8
SH-Control-Monotonic						
S1	-	-	-	-	3.4	3.1

Specimen description: See Table 4.2 for sample descriptions. T. St. and ΔT. St. represent the tensile strength and change in tensile strength of the specimens at different time points. *****Experiment was terminated after 8 days due to reactor leakage.

At 1% strain, the specimens showed an average tensile strength of ~2.9 MPa. After curing for 56 days, the average tensile strength increased to 3.4 MPa at failure. This is comparable to the strength of the unaltered ECC material under monotonic stress (**Figure 4.2)**, indicating that the intrinsic tensile strength of the material was not significantly affected by the initial pre-stressing of the specimen to 1% tensile strain. While the re-stressed SH-Controls 1 and 2 specimens achieved similar tensile strength as the unaltered material under monotonic load, the average tensile strain capacity of the pre-stressed specimens after re-stressing to failure (after 56 days) was 2.5%, which is considerably lower than the strain capacity measured in the specimen under monotonic load (3.1%). This suggests that the intrinsic tensile strain capacity had been altered due to either the initial preloading condition or further hydration of the composite for 56 days. Similarly, the tensile stiffness, which is the initial slope of the linear portion of the stress-strain curve and a measure of

the resistance of the composite to deformation under tensile load, reduced when the specimens were reloaded to failure **(Figure 4.2a)**. Such alteration in tensile stiffness has been reported in previous studies by Zhang et al. (2017) and Li and Yang, (2007) and is due to the re-opening of the initial cracks that were generated when the specimen was pre-stressed to 1% strain.

For specimens exposed to CO_2-acidified water following pre-stress to 1% tensile strain (SH-CO_2-H2O), the initial (pre-carbonation) tensile strength and stiffness were similar to the uncarbonated control specimens **(Figure 4.5b)**. After carbonation for 56 days, the specimens showed ~38% increase in tensile strength compared to the pre-carbonation strength at 1% strain. In contrast to the uncarbonated pre-strained specimens that showed similar ultimate tensile strength to the specimen that was stressed monotonically to failure, the tensile strength of the carbonated specimen increased by ~17% relative to the control specimen under monotonic stress.

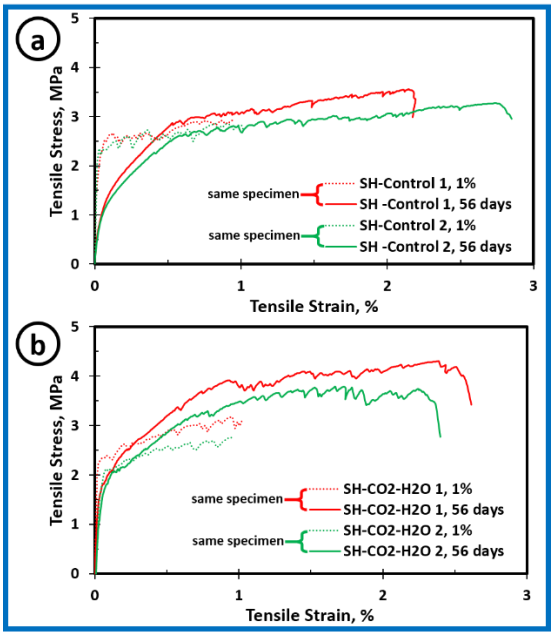

Figure 4.5: Tensile stress vs. tensile strain curves for **(a)** Control ECC specimens strained to 1% tensile strain and failure, after initial 28 days of curing and after additional 56 days of curing **(b)** ECC specimens strained to 1% tensile strain and failure after initial 28 days of curing and 56 days reaction in CO_2-acidified water at temperature of 50^{o}C and P_{co2} of 0.75 MPa, respectively.

This significant alteration in tensile strength of the material is due to the densification of the composite matrix resulting from carbonation and further hydration, as discussed extensively in **Chapter 3.** After carbonation, the SH-CO_2-H2O specimen showed a residual tensile strain capacity of 2.5 %, which is 250 times the tensile strain capacity of conventional wellbore cement and represents a 17% decrease in tensile strain capacity relative to the monotonically stressed specimen. Because the average tensile strain capacity of the carbonated SH-CO2-H2O specimens was similar to the average strain capacity of the uncarbonated pre-stressed ECC (SH-Control)at failure, carbonation of the pre-stressed dogbone specimens did not appear to negatively alter the strain capacity of the material under the test conditions.

Compared to the uncarbonated specimens that showed marked decreases in tensile stiffness when reloaded to failure after 56 days of further curing, the tensile stiffness of the SH-CO2-H2O specimens recovered significantly after carbonation in CO_2-acidified water. Such recovery of tensile stiffness has been reported in a prior study by Zhang et al. (2017) and has been attributed to healing of the microcracks, which further supports the conclusion that the material underwent internal self-healing following its exposure to CO_2-acidified water despite a lack of surficial crack healing in all cracks. Furthermore, the fact that the tensile strength of the material increased significantly and ECC showed minimal change in tensile strain capacity after reacting with CO_2-acidified water suggests that the mechanical performance of pre-stressed ECC will not be compromised when applied for wellbore cementing in CO_2 injection operations.

Figure 4.6a shows the tensile stress-strain curves for uncarbonated ECC dogbone specimens stressed consecutively to 1% tensile strain, 0.5% tensile strain, and failure (SH-Stiffness). The specimens were re-stressed to 0.5% strain to simulate a wellbore cement sheath undergoing cyclic stress due to CO_2 injection. At 1% tensile strain, the specimen had a tensile strength of 2.6 MPa.

When the specimen was unloaded and re-stressed to 0.5% tensile strain, the tensile strength was 2.4 MPa, which is ~7% below the tensile strength at the initial 1% strain. When stressed to failure, the ultimate tensile strength was 2.9 MPa, which is a 12% increase in tensile strength relative to the strength at 1% strain. In contrast to the SH-Control and SH-CO2-H2O, which exhibited partial restoration of tensile stiffness, the tensile stiffness of the uncarbonated specimen at failure decreased further in comparison to tensile stiffness when re-stressed to 0.5% tensile strain. The incremental decrease in stiffness was due to further opening of the cracks due to cycling of tensile stress. However, the fact that the SH-Stiffness specimen exhibited tensile strain behavior similar to the unaltered ECC suggests that the pre-stress condition did not negatively impact its intrinsic tensile strain capacity.

Figure 4.6b shows the tensile stress-strain curves for specimens pre-stressed to 1% tensile strain and subsequently exposed to water-saturated CO_2 headspace for 28 days and 56 days. At 1% tensile strain, the uncarbonated specimens showed similar stiffness and average tensile strength to the control specimens. When the specimens were stressed to 0.5% strain following 28 days of carbonation, a 39% increase in tensile strength was observed relative to the strength at 1% strain. This is comparable to the ultimate tensile strength of the specimens exposed to CO_2-acidified water and significantly higher than the tensile strength of the uncarbonated specimen at 0.5% strain. After exposing the specimens to CO_2 for an additional 28 days, a 12% increase in tensile strength was observed. The fact that the specimens exposed to water-saturated CO_2 showed a greater extent of change in tensile strength in comparison to the specimens exposed to CO_2-acidified water suggests that a more complete carbonation and densification of the material occurred. This was confirmed by the phenolphthalein pH test, which showed that the SH-CO2-G specimens were fully carbonated after 28 and 56 days while the specimens exposed to CO_2-acidified water were only

partially carbonated after 56 days (**Appendix Figure C.9**). In comparison to the samples exposed to CO_2-acidified water that showed near-complete restoration of tensile stiffness, the tensile stiffness of the specimens exposed to the wet CO_2 gas was only partially restored after 28 and 56 days, which can be explained by less efficient healing of the cracks as discussed in **Section 4.3.2 and 4.4.3.** While CO_2-acidified water did not significantly impact the 56-day residual tensile strain capacity relative to the controls, as SH-CO2-H2O specimens exhibited similar residual tensile strain capacity as the control specimens after 56 days, exposure to water-saturated CO_2 markedly decreased the residual tensile strain capacity from 3.1% to 1.5%. This likely results from more rapid carbonation rates and densification of the matrix and fiber/matrix interface following exposure of the specimen to wet CO_2 gas. This suggests that while exposure to wet CO_2 gas (e.g. near caprocks) would likely improve the tensile strength performance of ECC, it would also lead to more rapid and extensive carbonation that could produce greater changes in the tensile strain performance of the material compared to specimens in the downhole region exposed to CO_2-acidified water. For specimens exposed to water-saturated CO_2 in the presence of 1M NaCl solution (SH-CO2 GNaCl), post-carbonation characteristics of the stress-strain curve were similar to that of samples exposed to CO_2 gas in the presence of DI water (**Figure 4.7**).

This was expected as the exposure condition is comparable to specimens exposed to wet CO_2 gas in the presence of DI water, except that the DI water was substituted with the 1M NaCl solution in the pressure vessel. Because the specimens were not in direct contact with the 1M NaCl solution, the interaction of the specimens with the solution was primarily with the water vapor that would have been desalted before interacting with the specimens. Similar to specimens with pure DI water, a noticeable increase in tensile strength was observed. The average tensile strength was 3.9 MPa after 8 days, which is a 20% increase over the initial strength. Additionally, partial restoration of

the tensile stiffness of the specimen was observed after 8 days and the average tensile strain capacity of the specimen was reduced to ~ 1.5%. Although the experiment had to be terminated after 8 days due to leaks in the reactor, full carbonation had occurred after 8 days, which is more rapid than the carbonation of the specimens exposed to CO_2-acidified water that showed only partial carbonation after 56 days. This fast and rapid carbonation of specimens exposed to CO_2 gas likely contributed to the reduced tensile strain capacity of the specimens in comparison to specimens exposed to CO_2-acidified water.

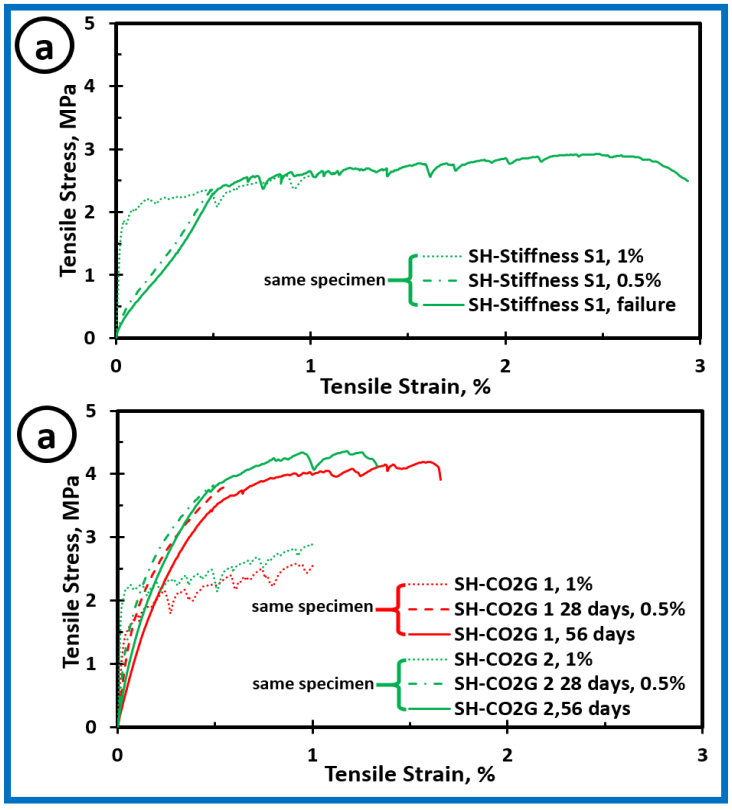

Figure 4.6: Tensile stress vs. strain curves for **(a)** Uncarbonated ECC dogbone specimen stressed consecutively to 1% tensile strain, 0.5% tensile strain, and failure and **(b)** ECC dogbone specimens stressed to 1% tensile strain pre-carbonation and to 0.5% tensile strain and failure after carbonation for 28 and 56 days.

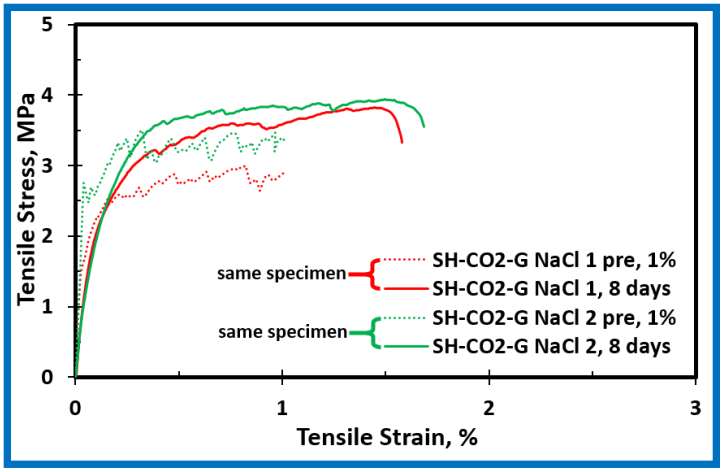

Figure 4.7: Tensile stress vs. strain curves for two ECC dogbone specimens at 1% tensile strain and following exposure to wet CO_2 gas in the presence of 1M NaCL solution.

4.3.5 Influence of CO_2 partial pressure on self-healing and permeability alteration

Table 4.6 presents the results of the high-pressure static batch experiments (**Section 4.3.5**), conducted to evaluate the extent of self-healing and permeability alteration in ECC exposed to a representative GCS condition of 10 MPa P_{CO2}, relative to the low-pressure condition of 0.75 MPa. The results showed that specimens exposed to the high-pressure environment exhibited similar permeability alteration behavior as specimens in the low-pressure environment after 28 days of reaction, but the extent of carbonation was greater in the high-pressure environment.

Table 4.6: Permeability of specimens before and after exposure to CO2 under high-pressure and low-pressure conditions. Tests were carried out for 28 days on coupon specimens using 600-mL batch reactors.

Exposure condition	$k_{o\text{-}1\%}$ (mD)	$k_{28\ days}$ (mD)	Δk_1 (%)	Carb. depth (mm)
High pressure experiment at T = 50°C, P_{co2} = 10 MPa				
HP-CO2-H2O	4.1	impermeable	-	full
HP-CO2-G	30.3	15.5	-49	full
Low pressure experiment at T=50°C, P_{co2} = 0.75 MPa				
LP-CO2-H2O	14.8	0.1	-99	5.0
LP-CO2-G	2.6	0.2	-92	3.5

Note: $K_{o\text{-}1\%}$ is the permeability at 1% tensile strain, $K_{28\ days}$ is the permeability after 28 days of carbonation, and $\Delta k_{28\ days}$ is the percentage change in permeability, relative to $K_{o\text{-}1\%}$, after 28 days.

For the specimens exposed to CO_2-acidified water (HP-CO2-H2O) at 10 MPa, the initial permeability was 4.1 mD. After 28 days, the permeability could not be determined because flow did not occur though the healed specimen under the initial test conditions. After 6 hours of further testing, flow was not achieved, which indicates that the cracks had sealed significantly. For the specimen exposed to wet supercritical CO_2 at 10 MPa (HP-CO2-G), a 49% decrease in permeability was measured, which is less than the extent of permeability alteration in the specimens exposed to CO_2-acidified water. This indicates that crack healing will be more favorable in the downhole region where the cement sheath is in contact with CO_2-acidified water. For the specimen exposed to CO_2-acidified water at 0.75 MPa P_{CO2} (LP-CO2-H2O), the permeability decreased by 99% after 28 days, while permeability decreased by 92% in the specimens exposed to CO_2 headspace (LP-CO2-G) under the same pressure and temperature conditions. Because the initial permeability of the LP-CO2-H2O specimen was ~5.5 times greater than the permeability of the LP-CO2-G specimen, but its final permeability was lower that of the LP-CO2-H2O specimen under the same temperature and pressure condition, it is clear that the CO_2-acidified water environment more significantly altered the permeability of the coupons under high pressure versus low pressure conditions. These observations further support the permeability and crack healing characterization results presented in **Section 4.4.2** and **Section 4.4.3**, which showed that self-healing was more effective in specimens exposed to CO_2-acidified water in comparison to specimens exposed to wet CO_2 gas. Similar to cracked dogbone specimens that showed multiple locations with self-healed cracks under low-pressure conditions, several healed cracks were observed in coupons exposed to CO_2-acidified water and wet supercritical CO_2 at 50^{o}C and 10 MPa, confirming that the observed permeability change was due to self-healing of cracks in the specimens.

Because the specimens exposed to CO_2-acidified water at 10 MPa P_{CO2} showed higher extents of carbonation after 28 days compared to the specimens at P_{CO2} of 0.75 MPa (**Table 4.6**), the long-term residual tensile strain capacity of ECC may be impacted more significantly under actual GCS pressure conditions than the results of the low-pressure experiments indicate in **Figure 4.5b**. This is because a greater extent of carbonation will lead to larger alterations in the tensile ductility and strain capacity of ECC, which has also been reported in prior studies carried out by Wu et al. (2018) on ECC during carbonation curing. However, given that the fully carbonated specimens exposed to the CO_2 headspace showed a tensile strain capacity of ~1.6%, which is 160 times the tensile strength of the conventional wellbore cement, we expect that the carbonated ECC material will continue to exhibit superior tensile properties compared to the conventional wellbore cement.

4.4 Conclusion

ECC is being proposed for wellbore cementing during GCS because of its superior tensile properties, tight microcracking behavior, and ability to undergo autogenous self-healing when damaged, in comparison to conventional wellbore cement. However, its self-healing performance and the implications for long-term permeability and tensile strain capacity under GCS conditions had not yet been demonstrated. This study set out to address this question under GCS conditions using pre-stressed ECC specimens.

After several weeks of reaction, cracks were found to self-heal under all exposure conditions tested, with cracks ~32µm wide exhibiting full healing after 56 days of reaction. Although not all cracks of similar aperture size self-healed when exposed to the same environmental conditions, a greater extent of healing was observed with increased exposure time, indicating that self-healing of cracks is progressive. The fact that crack closure occurred in the control specimens exposed to 99% RH environment showed that autogenous healing in ECC is not limited to carbonation, and

self-healing will progress through other mechanisms such as continuous hydration and swelling of C-S-H in a humid environment. While permeability reductions occurred in all tested specimens, consistent with the crack healing observed under all exposure conditions, the most significant permeability decrease and crack healing occurred in ECC exposed to CO_2-acidified water under both low-pressure and high-pressure conditions. This demonstrates that crack healing in ECC will be more favorable in the downhole section of the wellbore where CO_2 injection occurs.

As expected, the tensile strain capacity of ECC was impacted by carbonation. The fully-carbonated specimens exposed to wet CO_2 gas had a tensile strain capacity of ~1.6%, compared to a strain capacity of ~3.1% for the unaltered specimen. The residual strain capacity of ECC exposed to CO_2-acidified water was 2.5% over the same period. Because the specimens exposed to CO_2-acidified water showed the most significant crack healing, exhibited by the largest permeability reduction, and showed the least alteration in tensile strain capacity and ductility, we conclude that the most beneficial application of ECC for wellbore cementing during GCS wells will be derived near the downhole region where the cement sheath is in contact with CO_2-acidified water.

4.5 References

Bachu, S., Celia, M.A., 2009. Assessing the potential for CO2 leakage, particularly through wells, from geological storage sites, in: Geophysical Monograph Series. Am. Geophys. Union Wash. C Pp 203–216.

Brunet, J. -p. L., Li, L., Karpyn, Z.T., Huerta, N.J., 2016. Fracture opening or self-sealing: Critical residence time as a unifying parameter for cement–CO2–brine interactions. Int J Greenh Gas Control 47, 25–37. https://doi.org/10.1016/j.ijggc.2016.01.024

Cao, P., Karpyn, Z.T., Li, L., 2015. Self-healing of cement fractures under dynamic flow of CO2-rich brine. Water Resour. Res. 51, 4684–4701. https://doi.org/10.1002/2014WR016162

Carey, J.W., Wigand, M., Chipera, S.J., WoldeGabriel, G., Pawar, R., Lichtner, P.C., Wehner, S.C., Raines, M.A., Guthrie Jr., G.D., 2007. Analysis and performance of oil well cement with 30 years of CO2 exposure from the SACROC Unit, West Texas, USA. Int. J. Greenh. Gas Control, 8th International Conference on Greenhouse Gas Control TechnologiesGHGT-8 1, 75–85. https://doi.org/10.1016/S1750-5836(06)00004-1

Carroll, S., Carey, J.W., Dzombak, D., Huerta, N.J., Li, L., Richard, T., Um, W., Walsh, S.D.C., Zhang, L., 2016. Review: Role of chemistry, mechanics, and transport on well integrity in CO2 storage environments. Int J Greenh Gas Control 49, 149–160. https://doi.org/10.1016/j.ijggc.2016.01.010

Edvardsen, C., 1999. Water Permeability and Autogenous Healing of Cracks in Concrete. MJ 96, 448–454. https://doi.org/10.14359/645

Freeze, R.A., Cherry, J.A., 1979. Groundwater. Prentice Hall, Englewood Cliffs, NJ.

Herbert, E.N., Li, V.C., 2013. Self-Healing of Microcracks in Engineered Cementitious Composites (ECC) Under a Natural Environment. Materials 6, 2831–2845. https://doi.org/10.3390/ma6072831

Huerta, N.J., Bryant, S.L., Strazisar, B.R., Kutchko, B.G., Conrad, L.C., 2009. The influence of confining stress and chemical alteration on conductive pathways within wellbore cement. Energy Procedia 1, 3571–3578.

Huerta, N.J., Hesse, M.A., Bryant, S.L., Strazisar, B.R., Lopano, C., 2016. Reactive transport of CO2-saturated water in a cement fracture: Application to wellbore leakage during geologic CO2 storage. Int. J. Greenh. Gas Control 44, 276–289. https://doi.org/10.1016/j.ijggc.2015.02.006

JSCE, 2008. Recommendations for Design and Construction of High Performance Fiber Reinforced Cement Composites with Multiple Fine Cracks (HPFRCC).

Kan, Shi, H. -s., Sakulich, A.R., Li, V.C., 2010. Self-Healing Characterization of Engineered Cementitious Composite Materials. ACI Mater 107, 617–624.

Kjøller, C., Sigalas, L., Frykman, P., Bjørge, R., Torsæter, M., 2016. Cement Self-Healing as a Result of CO2 Leakage. Energy Procedia, The 8th Trondheim Conference on CO2 Capture, Transport and Storage 86, 342–351. https://doi.org/10.1016/j.egypro.2016.01.035

Lepech, M.D., Li, V.C., 2009. Water permeability of engineered cementitious composites. Cem. Concr. Compos. 31, 744–753. https://doi.org/10.1016/j.cemconcomp.2009.07.002

Li, V.C., 2009. Engineered Cementitious Composites (ECC) – material, structural and durability performance, in: Concrete Construction Engineering Handbook. CRC Press, Boca Raton.

Li, V.C., 2003. On engineered cementitious composites (ECC). J Adv 1, 215–230.

Li, V.C., Herbert, E., 2012. Robust Self-Healing Concrete for Sustainable Infrastructure. J. Adv. Concr. Technol. 10, 207–218. https://doi.org/10.3151/jact.10.207

Li, V.C., Yang, E.-H., 2007. Self Healing in Concrete Materials, in: Self Healing Materials, Springer Series in Materials Science. Springer, Dordrecht, pp. 161–193. https://doi.org/10.1007/978-1-4020-6250-6_8

Liteanu, E., Spiers, C.J., 2011. Fracture healing and transport properties of wellbore cement in the presence of supercritical CO2. Chem. Geol. 281, 195–210. https://doi.org/10.1016/j.chemgeo.2010.12.008

Liu, H., Zhang, Q., Gu, C., Su, H., Li, V.C., 2016. Influence of micro-cracking on the permeability of engineered cementitious composites. Cem. Concr. Compos. 72, 104–113. https://doi.org/10.1016/j.cemconcomp.2016.05.016

Luquot, L., Abdoulghafour, H., Gouze, P., 2013. Hydro-dynamically controlled alteration of fractured Portland cements flowed by CO2-rich brine. Int. J. Greenh. Gas Control 16, 167–179. https://doi.org/10.1016/j.ijggc.2013.04.002

Ramm, W., Biscoping, M., 1998. Autogenous healing and reinforcement corrosion of water-penetrated separation cracks in reinforced concrete. Nucl. Eng. Des. 179, 191–200. https://doi.org/10.1016/S0029-5493(97)00266-5

Reinhardt, H.-W., Jooss, M., 2003. Permeability and self-healing of cracked concrete as a function of temperature and crack width. Cem. Concr. Res. 33, 981–985. https://doi.org/10.1016/S0008-8846(02)01099-2

Wang, K., Jansen, D.C., Shah, S.P., Karr, A.F., 1997. Permeability study of cracked concrete. Cem. Concr. Res. 27, 381–393. https://doi.org/10.1016/S0008-8846(97)00031-8

Wu, H.-L., Zhang, D., Ellis, B.R., Li, V.C., 2018. Development of reactive MgO-based Engineered Cementitious Composite (ECC) through accelerated carbonation curing. Constr. Build. Mater. 191, 23–31. https://doi.org/10.1016/j.conbuildmat.2018.09.196

Yang, Y., Lepech, M.D., Yang, E. -h., Li, V.C., 2009. Autogenous healing of engineered cementitious composites under wet–dry cycles. Cem 39, 382–390. https://doi.org/10.1016/j.cemconres.2009.01.013

Zhang, Z., Qian, S., Liu, H., Li, V.C., 2017. Ductile Concrete Material with Self-Healing Capacity for Jointless Concrete Pavement Use. Transp. Res. Rec. J. Transp. Res. Board 2640, 78–83. https://doi.org/10.3141/2640-09

Zhang, Z., Zhang, Q., Li, V.C., 2019. Multiple-scale investigations on self-healing induced mechanical property recovery of ECC. Cem. Concr. Compos. 103, 293–302. https://doi.org/10.1016/j.cemconcomp.2019.05.014

CHAPTER 5

Conclusion and Future Work

5.1 Conclusion

Geologic carbon storage is a promising technology to reduce anthropogenic CO_2 emissions and combat global climate change, but CO_2 leakage through a compromised wellbore cement sheath can impact the long-term success of GCS. Because of the weak tensile properties of conventional wellbore cement, cement sheath damage can occur at various stages during the lifetime of the well, particularly during CO_2 injection. Such damage may be controlled by using novel cementing materials that offer superior tensile performance in comparison to conventional wellbore cement. This dissertation focused on investigating the use of Engineered Cementitious Composite (ECC), a novel fiber-reinforced cementitious material, with superior tensile properties, as a substitute to conventional wellbore cement.

In **Chapter 2**, the unique physical and chemical alteration of conventional wellbore cement under GCS conditions was investigated using static batch experiments. Characterization of the ECC material following exposure to CO_2-acidified water at different time points indicates that the primary alteration mechanism in ECC is carbonation driven, *i.e.* conversion of the calcium-rich parent material to calcium carbonate. The degree of carbonation of ECC was found to be a diffusive process and its extent can be predicted using Fick's law of diffusion. In contrast to neat Class H cement that exhibits multiple alteration zones with sharp variations in chemical gradients and mechanical characteristics along the altered front, a consistent alteration pattern with gradual

change in mechanical hardness as the depth of carbonation and duration of exposure increased was observed in ECC. Microhardness of the unaltered core of the reacted specimen increased with time due to continued pore refinement resulting from pozzolanic reactions at higher temperatures and pressures. These indicate that continuous evolution of ECC's mechanical properties can be expected under GCS conditions.

X-ray computed tomographic analysis revealed that PVA fibers in ECC will have a positive impact on the storage security of ECC-completed wellbore cement sheaths through reduced long-term permeation of CO_2. This is because PVA fibers bridging the composite's macropores serve as nucleation sites for precipitation of calcium carbonate following reaction with CO_2. Such precipitation can be expected to promote a reduction in the size of macropores that otherwise will not attenuate after carbonation. Such attenuation will decrease the permeability of the cement sheath, which positively impacts long-term storage security. Characterization of the fiber/matrix interfacial transition zone (ITZ), using scanning electron microscopy, following exposure to CO_2, showed that the reaction of ECC with CO_2 would lead to the densification of the ITZ. Densification of the ITZ after CO_2 exposure, which was observed in several locations in the carbonated specimens, could have a negative impact on the engineered ductility and tensile strain capacity of the ECC. This is because a densified ITZ creates a stronger bond between the fiber and the matrix that exceeds the engineered bond properties, potentially causing the fiber to break when the composite is stressed under tension. Such sudden fiber damage will lead to a more brittle composite material compared to the unaltered uncarbonated material.

In **Chapter 3**, a rheologically re-engineered ECC mix (WECC) optimized for wellbore cementing was developed. The effect of carbonation reactions on the overall mechanical integrity of WECC was investigated using customized WECC coupons exposed to CO_2-acidified solutions

at GCS temperature and pressure conditions over a period of 4 weeks. Post reaction bending test analysis showed that the ductility of WECC decreased significantly following exposure to CO_2 but the ductility decrease was not more significant at longer durations of exposure. This change in ductility is consistent with findings in **Chapter 2** that showed that the fiber/matrix ITZ would be densified following carbonation of the material. Conversely, carbonation of ECC increased its compressive strength and ultimate flexural strength at longer durations of exposure. This is because the combined effect of the densification of the fiber/matrix ITZ and pore filling of the WECC leads to an increase in the first crack strength and its ability to continue to bear additional load. While carbonation of WECC reduced its ductility, in comparison to the unaltered material, the overall long-term mechanical integrity and mechanical performance were consistently superior to the performance of conventional cementing materials under all test conditions. Additionally, when compared to conventional wellbore cement, WECC exhibits superior structural integrity after exposure to CO_2-acidified water because microfibers mitigated the material loss observed in conventional wellbore cement by binding the matrix together. Superior mechanical resistance to deformation in WECC in comparison to conventional fly ash-amended material mirrored this superior long-term physical integrity and structural stability.

Qualitative analysis of the depth of carbonation in WECC at multiple time points showed that WECC exhibits similar depths of alteration as conventional fly ash-amended wellbore cement. Similarly, mercury intrusion porosimetry analysis carried out to evaluate the fluid flow characteristics of ECC material suggests that ECC exhibits similar transport behavior as conventional fly ash-amended cement, which suggests that the incorporation of microfibers will not negatively impact the transport properties of WECC significantly relative to conventional fly ash-amended wellbore cement. When coupled with the superior mechanical performance of ECC

over conventional wellbore cement, the fact that no negative impact of fibers in ECC was observed suggests that substituting conventional fly ash-amended wellbore cement with ECC will lead to a significant increase in the mechanical integrity of the wellbore cement sheath.

In **Chapter 4**, crack healing was demonstrated to occur in ECC following exposure to CO_2. Pre-stressed dogbone specimens were exposed to CO_2-acidified water and wet CO_2 gas under low-pressure and high-pressure conditions for several weeks and the evolution of the crack apertures was tracked using optical microscopy. Crack healing was observed in specimens under all exposure conditions tested but not all cracks with similar characteristics and exposure conditions exhibited crack healing. Greater extent of crack closure was observed as the exposure duration increased, which suggests that crack healing in ECC is a time-dependent process. The fact that crack closure was not consistent in cracks with similar aperture size is likely due to local variations in matrix composition and crack aperture characteristics. The maximum crack with full self-healing after 56 days was 32μm, which was twice the average crack width of 16 μm in the ECC formulation used at 1% tensile strain. Carbonation was found not to be the dominant mechanism for crack self-healing as uncarbonated specimens exposed to moisture showed similar self-healing characteristics as carbonated specimen, and fully carbonated specimens exposed to CO_2-gas did exhibit more significant crack closure in comparison to partially carbonated samples.

Although full surficial crack healing was not observed in many specimens, permeability decrease occurred consistently in all the specimens following exposure to CO_2. The fact that surficial crack closure did not occur uniformly but permeability decrease was observed in all specimens is attributed to preferential internal crack healing relative to surficial healing, due to lower pH conditions in the interior of the specimens relative to the relative to the sample surface. The most significant permeability decrease occurred in the specimens exposed to CO_2-acidified

water. For all conditions investigated, a decrease in the residual tensile strain capacity of the specimens was observed, which is consistent with observation in **Chapter 3**, which showed that carbonation leads to a decrease in the ductility of ECC. ECC specimens exposed to CO_2-acidified water had the lowest decrease in ductility and strain capacity, which suggests that the beneficial mechanical properties of ECC will be preserved when applied for cementing in the downhole environments relative to other regions where the cement sheath is exposed to streams of CO_2 gas.

5.2 Future Work

The benefits of adopting ECC for wellbore cementing during GCS have been highlighted in this dissertation, but further studies are needed to realize field application of ECC. Although ECC's composition is similar to conventional fly ash-amended wellbore cement, a slurry's unique flow properties required for pumping during wellbore completion operations might affect the distribution of the fibers in the low viscosity matrix. This is because the plastic viscosity of wellbore cement slurry is typically one order of magnitude below the viscosity of conventional ECC and uniform fiber dispersion is difficult to achieve in such low viscosity slurries. Poor fiber dispersion can negatively impact the ability to achieve reproducible tensile ductility, strain hardening behavior, crack width control, and crack self-healing across slurry batches.

Potential strategies to ensure uniform fiber dispersion include source-dispersion of the fibers to eliminate high energy mixing requirements, which can cause fiber clumping during slurry preparation. Additives that can potentially promote alignment of fibers and prevent clumping in a low viscosity mix without compromising the fiber/matrix interfacial bond, such as low-viscosity polyethelene glycol, can be investigated. Strategies such as reduction of fiber volume, as adopted in the ECC mix presented in **Chapter 3**, can also be considered to reduce fiber clumping. However,

fiber volume reduction will limit the overall tensile strain capacity and ductility performance of ECC as tensile performance is dependent on fiber volume.

This study investigated the impact of CO_2 on the properties of various ECC compositions and evaluated their suitability for wellbore cementing during GCS. While ECC consistently showed superior mechanical performance in comparison to conventional wellbore cement formulations, its performance has been benchmarked against conventional wellbore cement that has not been designed to withstand the unique environmental conditions during GCS. Future work should evaluate reasonable tensile strength requirements for wellbore cementing applications and optimize ECC specifically for such operating conditions. Furthermore, future work can investigate the use of carbonation inhibitors to prevent the changes in the engineered fiber/matrix ITZ, and preserve the ductility and tensile strain capacity of the composite after long-term exposure to CO_2.

APPENDICES

Appendix A
Supplementary Information for Chapter 2

A.1 Characterization of aqueous chemistry

Cation analysis (Ca, Mg, Fe, Si, Na, K, and Al) was carried out via inductively coupled plasma mass spectrometry (ICPMS; 7900 Agilent Technologies, CA) on samples acidified with HNO_3 to a pH < 2, while anion analysis was done using ion chromatography (Agilent Technologies, CA). CO_2 solubility under each experimental condition was calculated using the thermodynamic model presented by Duan and Sun [1], and equilibrium constants were adjusted to account for the system temperature (50^{o}C) and pressure (10 MPa) conditions using SUPCRT92 with the DPRONS92 database[2]. The activity coefficients of the aqueous species were estimated using the Davies equation, and the pH of the solution at each sampling point was calculated based on the measured cations and anions concentrations within the constraint of electroneutrality.

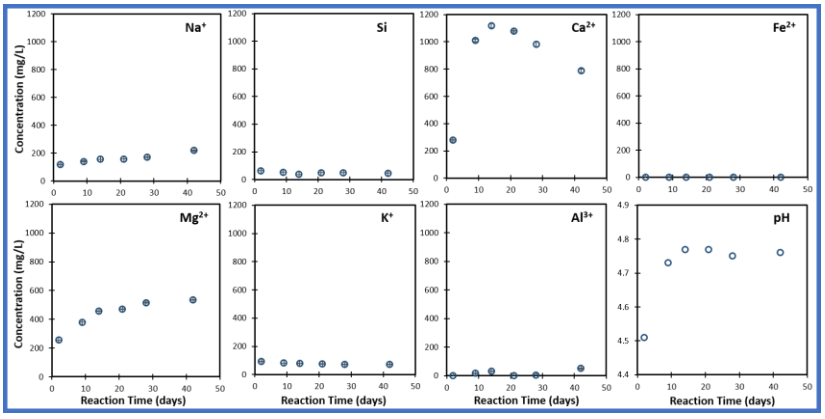

Appendix Figure A.1: Effluent chemistry and pH evolution of aqueous samples from the static batch study carried out at 50^{o}C and 10 MPa. The error bars correspond to the standard deviations of three replicate measurements.

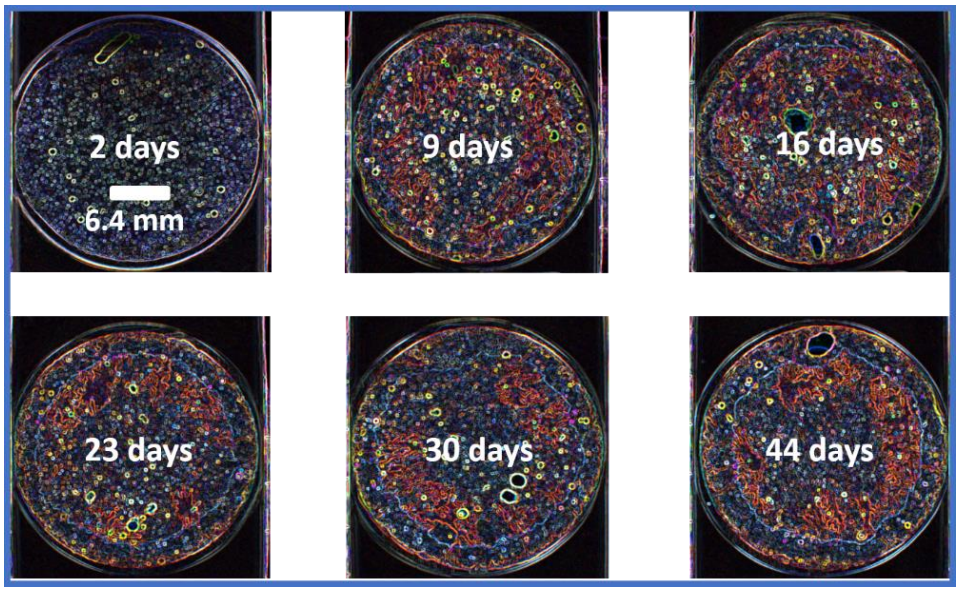

Appendix Figure A.2: Optical images of thin sections of reacted cores following the application of Sobel edge detection filter to delineate the extent of alteration. The leading edge of the alteration front is defined by the blue line.

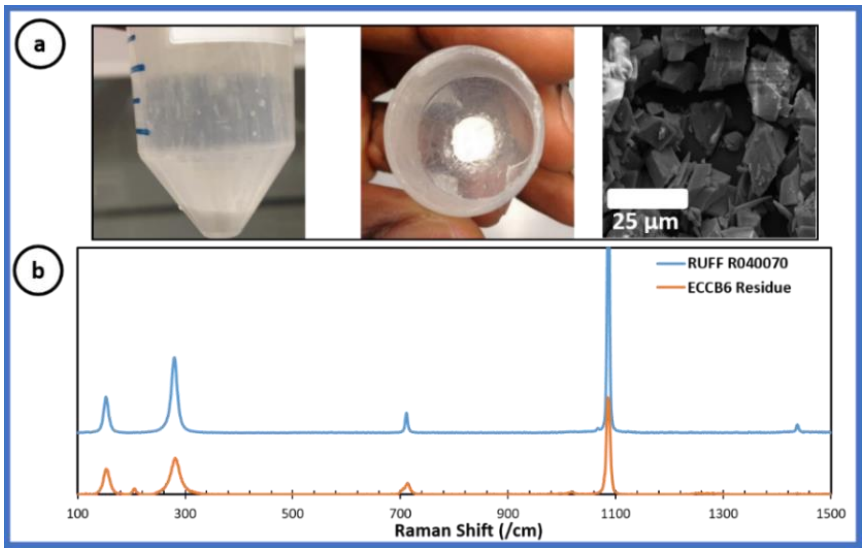

Appendix Figure A.3: **(a)** Precipitate from the aqueous sample retrieved from the batch reactor after the static batch experiment. **(b)** The Raman spectra of the precipitate shows that the material is calcite.

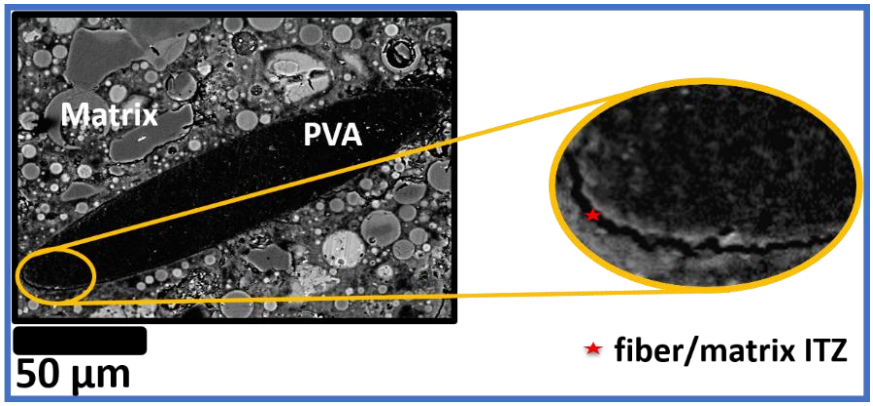

Appendix Figure A.4: BSE map showing the fiber/matrix interfacial transition zone (ITZ) in ECC prior to carbonation. The ITZ promotes fiber pullout rather than fiber rupture under tensile stress.

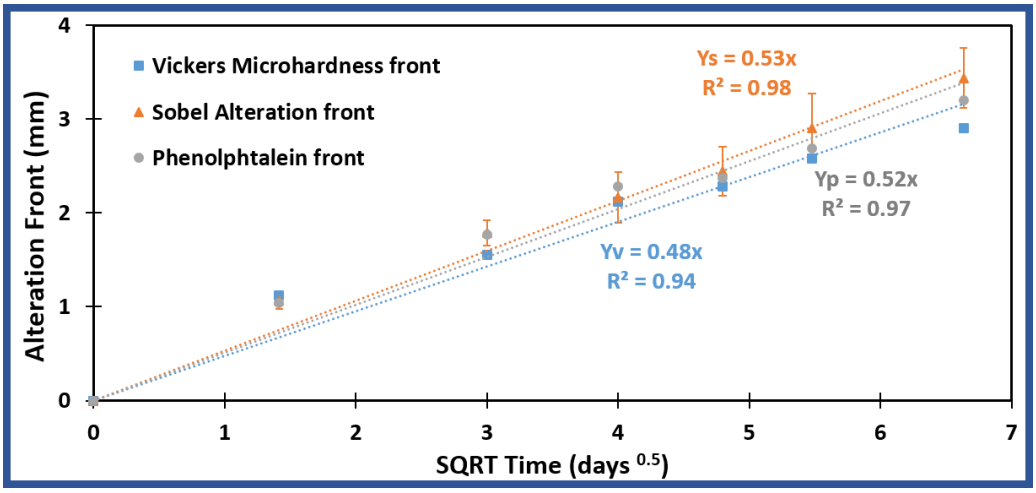

Appendix Figure A.5: Combined plot of the alteration front vs. SQRT time using Sobel edge detection, Phenolphthalein pH indicator, and Vickers microhardness. Equations Ys, Yp, and Yv describe Fick's CO_2 diffusion laws and depth of alteration in ECC as a function of time using the Sobel edge detection filter, phenolphthalein pH indicator, and Vickers microhardness, respectively. The predicted depths of penetration after 50 years of reaction using Ys, Yp, and Yv are 72 mm, 71 mm, and 64 mm, respectively.

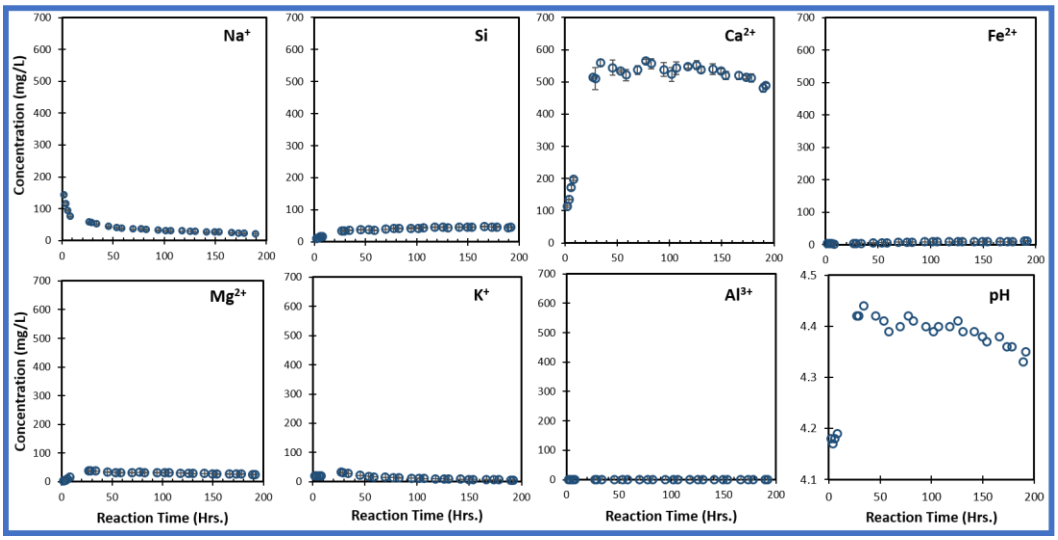

Appendix Figure A.6: Effluent chemistry and pH evolution of aqueous samples from the flow-through study carried out at 50ºC and 10 MPa. The error bars correspond to the standard deviations of three replicate measurements.

A.2 References

(1) Duan, Z.; Sun, R. An improved model calculating CO2 solubility in pure water and aqueous NaCl solutions from 273 to 533 K and from 0 to 2000 bar. *Chem. Geol.* **2003**, *193*, 257–271.

(2) Johnson, J. W.; Oelkers, E. H.; Helgeson, H. C. SUPCRT92: A software package for calculating the standard molal thermodynamic properties of minerals, gases, aqueous species, and reactions from 1 to 5000 bar and 0 to 1000 C. *Comput. Geosci.* **1992**, *18* (7), 899–947.

Appendix B

Supplementary Information for Chapter 3

B.1 Rheologic characteristics of cement

Cement slurry is characterized as a non-Newtonian fluid that exhibits flow properties described by the Bingham plastic model which states that the slurry must overcome the limiting share stress (τ) , also called the yield stress, before it can begin to flow (Ferraris and DeLarrard, 1998; Shahriar and Nehdi, 2012; Shaughnessy and Clark, 1988). Once the yield stress has been overcome and the slurry starts to flow, the share stress increase linearly relative to the share rate. The slope of the line that describes the relationship between the share stress and the share rate is referred to as the plastic viscosity of the slurry and its resistance to flow. Hence, the plastic viscosity measures ease of flow of the material after the yield stress has been overcome. Therefore, to define the rheological properties of a cementitious composite, it is important to determine both the yield stress and the plastic viscosity.

A Rheometer is typically used to directly measure the viscosity and yield stress of cement slurry. However, the presence of fibers in ECC limits the application of the method for accurate rheology determination. Prior work by Li and Li, (2013) showed that a quick accurate estimate of the plastic viscosity and yield stress of ECC can be obtained using the marsh cone flow test and the mini-slump test, respectively. In order to determine a suitable viscosity and yield stress for WECC and design a cement slurry with rheological properties that is applicable for wellbore cementing applications, a benchmark study was carried out to investigate rheology of neat Class

H wellbore cement using customized marsh cone and a mini-slump flow test apparatus presented in **Appendix Figure B.1.** The baseline study was carried out using Class H primary wellbore cement with water to cement ratio ranging from 0.3 to 0.6 of the total solid weight. Cement was prepared as disused in **Section 3.3.2**. For the benchmark study, no additives or viscosity-modifying agent were added to the slurry.

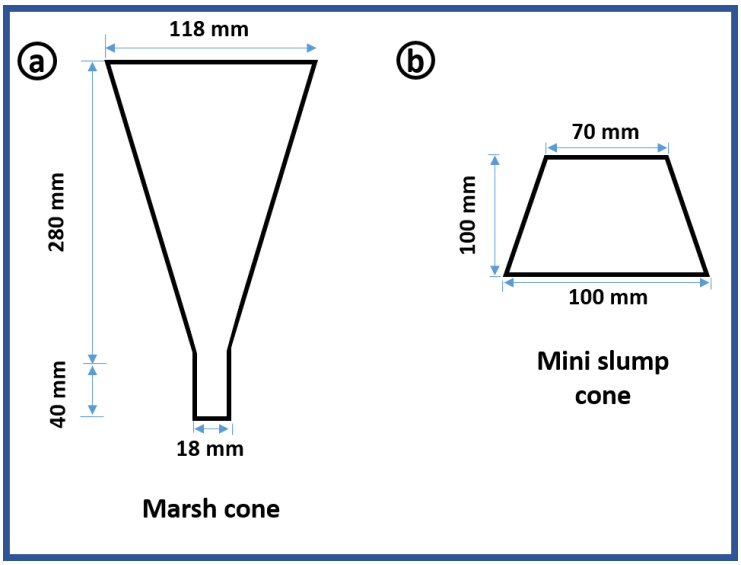

Appendix Figure B.1: Customized marsh cone funnel and standard mini-slump cone.

After mixing the slurry, a one-liter quantity of the slurry was poured into the funnel and allowed to flow into a container. The flow time of the material through the funnel was then recorded using a stopwatch. For the mini-slump test, the materials were poured into the mini-slump cone and placed on a smoot Plexiglas board on a flat surface. The cone was raised to allow the slurry to flow freely unto the surface of the Plexiglas board. The diameters of the circle were then measured and the average was recorded as the flow diameter of the slurry.

B.2 Rheology of Class H cement. FFWECC, and WECC

Appendix Table B.1 presents the flow properties of neat Class H cement at various water to cement ratios. As expected, as the water to cement ratio increased from 0.3 to 0.6, a significant increase was noticed in the mini-slump cone diameter. Images of the slump diameter are shown in **Appendix Figure B.2**. For example, an increase in the water to cement ratio from 0.38 to 0.4 increase the slump diameter by 50 mm which indicates that slight changes in the neat cement's water to cement ratio can reduce its resistance to flow significantly.

Similarly, for the marsh cone flow time, the time of flow decreased as the water content increased. At a ratio of 0.3, the flow time for the slurry exceeded 30 seconds, while at 0.6 water ratio, the flow time was 2.2 seconds. At ratio of 0.38, the flow time of the slurry was 4.2 seconds while the slump diameter is 240 mm. Because 0.38 water to cement ratio is typically used in specimen preparation for wellbore cement sheath studies (Kutchko et al., 2007; Verba et al., 2017, p. 2), we have chosen the slump diameter and flow times for neat cement slurry with water to cement ratio of 0.38 as benchmark for WECC design.

Appendix Table B.1: Mini-slump flow diameter and marsh cone flow time form neat Class H cement at different water: cement ratios.

Water: Cement	Slump diameter (mm)	Cone flow time (s)
0.3	110	>30
0.38	240	4.2
0.4	290	3.5
0.45	325	3.1
0.60	400	2.2

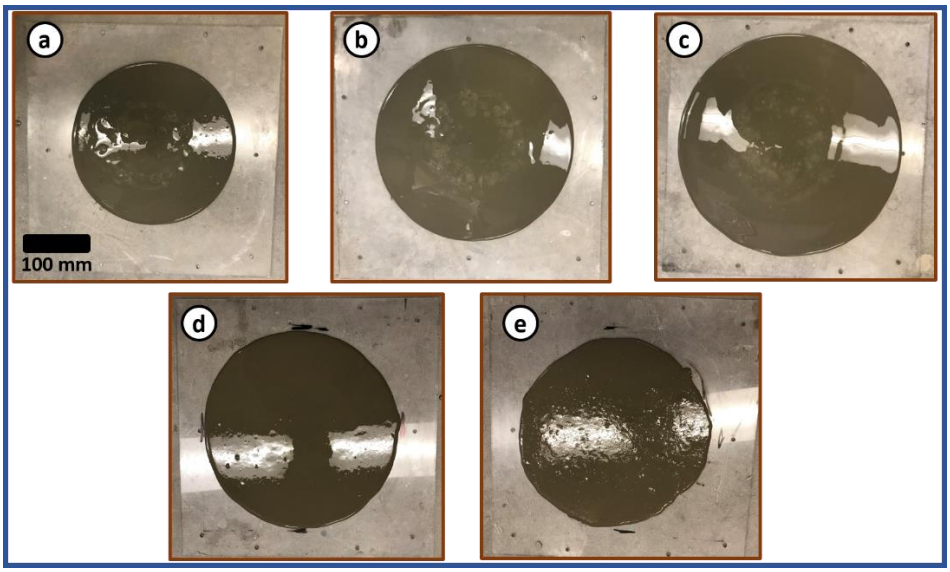

Appendix Figure B.2: Slump diameter of neat class H cement at water: cement ratios of (a) 0.38, (b) 0.40, and (c) 0.45. Tiles "d" and "e" show the slump diameters for FFWECC and WECC, respectively.

Appendix Table B.3 presents the rheology parameters for WECC and FFWECC, which shows that both WECC and FFWECC meet the desired flow time and slump diameter. Additionally, a marked reduction in the slump diameter and flow time was observed following the addition of microfibers in WECC, indicating that fibers will impact the rheology of fly ash amended wellbore cement slurry.

Appendix Table B.2: Mini-slump flow diameter and marsh cone flow time for FFWECC and WECC.

Composite type	Slump diameter (mm)	Cone flow time (s)
FFWECC	289	3.2
WECC	275	3.8

B.3 References

Ferraris, C.F., DeLarrard, F., 1998. Testing and Modeling of Fresh Concrete Rheology. NIST Interag. Intern. Rep. NISTIR - 6094. http://dx.doi.org/10.1002/https://dx.doi.org/10.6028/NIST.IR.6094

Kutchko, B.G., Strazisar, B.R., Dzombak, D.A., Lowry, G.V., Thaulow, N., 2007. Degradation of Well Cement by CO2 under Geologic Sequestration Conditions. Environ. Sci. Technol. 41, 4787–4792. https://doi.org/10.1021/es062828c

Li, M., Li, V.C., 2013. Rheology, fiber dispersion, and robust properties of Engineered Cementitious Composites. Mater. Struct. 46, 405–420. https://doi.org/10.1617/s11527-012-9909-z

Shahriar, A., Nehdi, M.L., 2012. Rheological properties of oil well cement slurries. Proc. Inst. Civ. Eng. - Constr. Mater. 165, 25–44. https://doi.org/10.1680/coma.2012.165.1.25

Shaughnessy, R., Clark, P.E., 1988. The rheological behavior of fresh cement pastes. Cem. Concr. Res. 18, 327–341. https://doi.org/10.1016/0008-8846(88)90067-1

Verba, C., Montross, S., Spaulding, R., Dalton, L., Crandall, D., Moore, J., Glosser, D., Huerta, N., Kutchko, B., 2017. Foamed Cement Interactions with CO2 (No. NETL-TRS-2-2017). National Energy Technology Lab. (NETL), Albany, OR (United States); National Energy Technology Lab. (NETL), Morgantown, WV (United States); National Energy Technology Lab. (NETL), Pittsburgh, PA, (United States). https://doi.org/10.2172/1340659

Appendix C

Supplementary Information for Chapter 4

C.1 Introduction

The properties of ECC that make it desirable for wellbore cementing during GCS have been discussed in **Chapters 1 to 3**. Because conventional M45 ECC was designed as a substitute to concrete for construction in which a plastic viscosity of the mortar ranges from 5-14 Pa.s, conventional ECC in its original state is not directly applicable for wellbore cementing during GCS. This is because such viscous slurry cannot be pumped downhole. For wellbore cementing applications, the required plastic viscosity of the slurry is about 0.3 Pa.s, which is about one order of magnitude less than the viscosity of conventional ECC. Hence, it is important to modify the rheologic properties of ECC to be adopted for wellbore cementing during GCS.

Li and Li. (2013) carried out a study to investigate the impact of ECC rheology on its mechanical properties and found a strong correlation between plastic viscosity, tensile strain capacity, and fiber dispersion. At higher viscosity, higher tensile strain capacity was achieved while at low viscosity, the strain capacity decreased greatly and was inconsistent for specimens generated from the same batch. They also found a correlation between the coefficient of fiber dispersion, i.e. the extent of uniform fiber dispersion in the matrix, and the tensile strain capacity. This is because mixes with high viscosity exhibit uniform fiber dispersion more favorably in comparison to low viscosity mixtures. The higher viscosity of the mix was also found to promote

the consistency of the tensile strain capacity of the specimens in the hardened state and their ability to show microcracking behavior. Thus, the viscosity requirement for wellbore cementing presents a challenge for the application of ECC as a wellbore cement as the viscosity of conventional ECC is significantly higher than the viscosity of wellbore cement.

Chapter 3 presented a novel wellbore engineered cementitious composite (WECC) with similar flow properties as conventional wellbore cement. To promote uniform fiber dispersion in the low-viscosity slurry during mixing, a fiber volume of 1.1% was used in WECC, which is significantly lower than conventional wellbore cement that uses a fiber volume of 2%. Uniform fiber dispersion is a state in which the fibers are evenly dispersed in the slurry and do not exhibit zones of clumping. While clumping was largely eliminated in WECC, a significant reduction in the volume of fibers from 2% to 1.1% likely limited its ductility. Because carbonation of ECC under GCS conditions has been found to reduce the ductility of ECC, it will be crucial to engineer higher ductility into the mix prior to carbonation to promote long-term intrinsic ductility of ECC following carbonation.

Although rheology similar to conventional wellbore cement was achieved in WECC presented in Chapter 3, the slurry exhibited free-water in the fresh state. Free-water is water that does not contribute to the hydration of the cement and typically settles at the top of a column when the slurry is left standing for an extended period of time. Because such free-water is undesirable and can potentially lead to negative consequences that will be discussed further, we set out to engineer free-water control into the design of the mix to prevent undesirable negative consequences during the wellbore cementing operation and during the service life of the well. In this optimization study, several mix compositions of ECC were prepared to further investigate the potential for further optimization of ECC rheology without loss of ductility. Sixteen ECC mixtures were prepared with

fiber volume ranging from 1.5% and 2.0% to investigate if such fiber volumes are realistic in ECC for wellbore cementing applications. The specimens were subsequently carbonated under typical GCS temperature and pressure conditions to investigate the evolution of the ductility and flexural strength of the material. The extent of carbonation alteration was also investigated for each specimen composition.

C.2 Materials, methods, and design considerations

C.2.1 Free-water control

Free-water is the excess water in cement that does not contribute to cement hydration. When in a static condition, free-water separates from the solid particles in the mix and settles at the top of a column. Free-water is undesirable in wellbore cement because it can lead to zones of discontinuities near the cement/casing or cement/reservoir interface that can cause annular gas leakage (Broni-Bediako et al., 2016). Additionally, free-water promotes cement sheath corrosion problems, which can create holes in the casing. Such holes will compromise the storage security of CO_2 by acting as channels for CO_2-leakage from the reservoir. Finally, free-water causes inconsistencies in the mechanical properties along the cement sheath due to variations in the densities as settling occurs.

Despite the addition of an antisettling agent to prevent free-water loss through gelation in WECC presented in **Chapter 3**, the slurry exhibited some free-water in the fresh state after the first 2 hours of casting as shown in **Appendix Figure C.1**. In this optimization study, we actively designed the cement slurry composition to control free-water through tailoring the ECC mix. In the oil and gas industry, free-water is controlled via the use of antisettling agents and addition of bentonite. Bentonite absorbs water up to 16 times its volume, preventing free-water while the

cement sets (Broni-Bediako et al., 2016; Samsuri et al., 2001). Bentonite is typically added up to 2% of cement weight. However, addition of bentonite can lead to a decrease in the compressive strength of the cement, which is undesirable (Nelson et al., 1990). Due to this limitation, we used silica fume, which improves the compressive strength of the composite and simultaneously controls free-water (Lam et al., 1998; Nelson et al., 1990). Typically amendment ratio by weight of cement for silica fume is 15% but it can be added up to 28% (Nelson et al., 1990) In this study, silica fume was added from 3 to 10% by weight of the solid components of ECC.

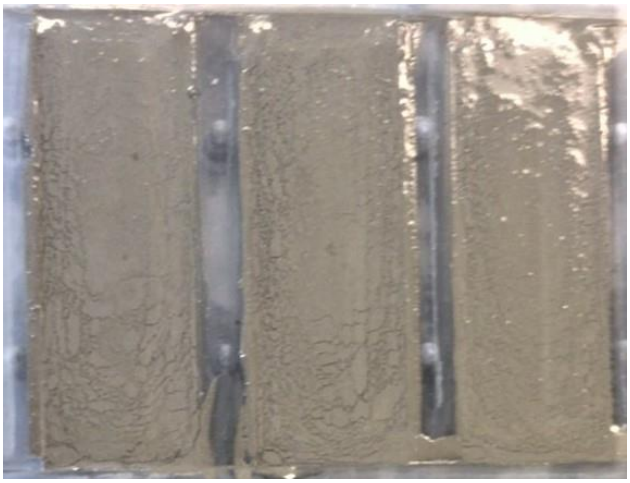

Appendix Figure C.1: Cast WECC slurry exhibits free loss after 2 hours of casting.

C.2.2 Experimental procedure

The slurries were prepared using the procedure outlined in **Section 3.3.2** with the components presented in **Appendix Table C.1**. **Appendix Table C.2** shows the compositions of the 16 specimens. The cast specimens were placed in a curing chamber at 99% RH to set and were demolded after 24 hours. The specimens were then cured for 7 days at 99% RH. The 7-day curing period was chosen for fast screening of the specimen. The specimens were subsequently exposed to CO_2-acidified water at 50^{o}C and 10 MPa for 2 days as described in **Section 3.3.2.** Three–point

flexural test was carried out on the carbonated and uncarbonated specimens using the procedure presented in **Section 3.3.4** to investigate the evolution of flexural strength and ductility. The depth of carbonation of each specimen was determined using the phenolphthalein pH indicator test, to investigate the impact of variations in mix proportions on the reactivity of the specimens.

Appendix Table C.1: ECC materials and sources.

	Product name		**Supplier**
Cement	Type III		Lafarge
Fly ash	Class F		Boral
Dispersant	(C11H5NAO4S)N	powder	Gelest
Superplasticizer	ADVA 190	Liquid	GCP
Antisettling agent	-	powder	-
Antifoam	AFE1410	Liquid	Dow Corning
Fiber	PVA	Length:12 mm; Oil coating :1.2%	Kurary, japan

C.3 Results

C.3.1 Fresh state slurry properties

Appendix Table C.3 presents the fresh state slurry properties of the ECC mixes. All the materials had slurry densities within the range of 1.7 to 1.9 g/cc, which is the range of slurry density for wellbore cementing applications (Nelson, 1990). Although the desired yield stress, inferred through the mini-slump flow diameter, was achieved for most of the specimens, the marsh cone flow time, which infers the plastic viscosity of the specimens was generally greater than the desired benchmarked range for wellbore cementing, even for compositions with mini-slump diameter greater than the benchmark diameter presented in **Appendix B**. Hence, achieving the desired yield stress range for the slurry does not guarantee that the plastic viscosity will be achieved.

Flow times and slump diameters for Mix 1 to 3 showed that an increase in the proportion of the superplasticizer decreases the flow time and increases the slump diameter of the slurry. Similarly, for Mix 15 and 16 with similar mix composition, a decrease in the proportion of superplasticizer in Mix 16 increased the flow time and decreased the slump diameter relative to Mix 15. However, the addition of superplasticizer influenced the slump diameter more significantly than the marsh cone flow time. An increase in fly ash proportion relative to the cement composition and decrease in silica fume will decrease the flow time of the slurry and increase the slump flow diameter.

The composition of the matrix and proportion of fibers also had a noticeable impact on the rheologic properties of the slurries. Increasing the fiber volume from 1.5% to 2% increased the flow time and decreased the slump diameter (see Mix 4 to Mix 11). The decrease in the proportion of silica fume led to and appreciable increase in the slump diameter but only a slight decrease in flow time (compare Mix 4 and Mix 6). An increase in fly ash proportion relative to cement and silica fume led to a significant increase in the slump diameter. Hence, the proportion of superplasticizer in the mix had to be decreased from 1.5% to 1% and 0.8%, for slurries with fly ash proportion of 0.6 (Mix 8 to Mix 13), to achieve similar rheologic properties as the mixtures with fly ash proportion of 0.4.

C.3.2 Mechanical properties of ECC mix compositions

Appendix Table C.4 presents the mechanical properties of the ECC material before and after reaction with CO_2-acidified water. The result indicates a consistent decrease in the total deflection of the specimens following carbonation for all the ECC mixes. The deflection of the specimens and thus their ductilities also increased as the fiber volume increased from 1.5 to 2% (**Appendix Figure C.2)**. Because of noticeable clumping of fibers in the mixes with 2% fiber volume, in

comparison to the specimens without the fiber, the use of fiber volume of 2% in ECC slurry for wellbore cementing during GCS is not recommended. In addition to the decrease in total deflection of the specimens, an increase in the ultimate flexural strength of the specimens was noticed post carbonation. This can be explained by the densification of the fiber/matrix ITZ and composite matrix as earlier described in **Chapter 2** and **Chapter 3**.

For the compressive strength, a clear trend was not observed after 24 hours. However, all the specimens tested showed compressive strength greater than 3.5 MPa, which is the API recommended minimum 24-hour compressive strength for wellbore cement. Additionally, greater compressive strength was observed for specimens with fly ash proportion of 0.4 relative to the mixtures with fly ash proportion of 0.4. Specimens with a larger proportion of cement in comparison to fly ash where the composition of the superplasticizer was 1.5% appeared to exhibit delayed setting. This likely affected the 24-hour compressive strength of the mixes. However, such delayed setting can be prevented by using a non-retarding superplasticizer or water reducers.

Appendix Figure C.3 shows the crack patterns for the uncarbonated and carbonated specimens. Mix 1 exhibited multiple microcracking behavior pre- and post-carbonation. Mix 2 and Mix 3 with similar composition but lower viscosity in comparison as Mix 1 exhibited larger cracks pre-carbonation and the microcracking behavior appeared to be reduced post-carbonation. This is because a reduction in the viscosity of the slurry negatively impacted the uniform fiber dispersion. Similarly, Mix 15 and Mix 16 exhibited the same trend as Mix 16, which was more viscous, showing more consistent microcracking behavior than Mix 15 with lower viscosity. This further supports previous studies that showed that fiber dispersion significantly impacts the microcracking behavior and ductility performance of ECC.

Appendix Table C.2: Composition of ECC mixes. Specimens were prepared using of 0.4% anti-settling agent, antifoam, and dispersant. Mix 15 and Mix 16 have a similar composition. However, the viscosity of Mix 16 was decreased in comparison to Mix 15 by increasing the proportion of SP, to achieve a slurry with comparable flow as conventional wellbore cement. Mix 16 was used in Chapter 4 to ensure consistency of the ECC crack pattern. Fiber volume is reported as % of total mix volume while slurry composition is a percentage of the total solid components.

	Mix 1	**Mix 2**	**Mix 3**	**Mix 4**	**Mix 5**	**Mix 6**	**Mix 7**	**Mix 8**
Cement	0.50	0.50	0.50	0.45	0.45	0.55	0.55	0.33
Fly Ash	0.40	0.4	0.40	0.40	0.40	0.40	0.4	0.60
Silica Fume	0.10	0.10	0.10	0.15	0.15	0.05	0.05	0.07
Water	0.40	0.40	0.40	0.40	0.40	0.40	0.40	0.40
SP (%)	0.5	1.0	1.5	1.5	1.5	1.5	1.5	1.0
Fiber vol. (%)	1.50	1.50	1.50	1.50	2.00	1.50	2.00	1.50
	Mix 9	**Mix 10**	**Mix 11**	**Mix 12**	**Mix 13**	**Mix 14**	**Mix 15**	**Mix 16**
Cement	0.33	0.3	0.3	0.37	0.37	1	0.4	0.4
Fly Ash	0.60	0.6	0.6	0.6	0.6	0	0.5	0.5
Silica Fume	0.07	0.1	0.1	0.03	0.03	0	0.1	0.1
Water	0.40	0.4	0.4	0.4	0.4	0.4	0.4	0.4
SP(%)	1.0	1.0	1.0	0.8	0.8	0	0.5	1.5
Fiber vol.(%)`	2.00	1.5	2.0	1.5	1.5	1.5	1.5	1.5

Appendix Table C.3: Flow properties and carbonation depth of ECC mixes.

	Mix 1	**Mix 2**	**Mix 3**	**Mix 4**	**Mix 5**	**Mix 6**	**Mix 7**	**Mix 8**
Density (g/cc)	1.8	1.8	1.8	1.8	1.7	1.8	1.9	1.8
Cone dia. (mm)	100	248	267	292	251	342	291	304
Flow time (s)	>30	25	15	10	12	11	15	7
Carb depth. (mm)	2.0	2.0	2.4	2.1	2.1	1.3	1.4	3.3
	Mix 9	**Mix 10**	**Mix 11**	**Mix 12**	**Mix 13**	**Mix 14**	**Mix 15**	**Mix 16**
Density (g/cc)	1.8	1.7	1.8	1.8	1.9	1.9	1.8	1.8
Cone dia. (mm)	215	318	254	317	289	219	270	180
Flow time (m3)	11	8	12	4.7	5.8	3.2	6	>30
Carb. Depth (mm)	3.3	4.1	4.3	2.6	2.2	0.3	2.6	2.6

Appendix Table C.4: The mechanical properties of the ECC mix compositions.

	Mix 1	**Mix 2**	**Mix 3**	**Mix 4**	**Mix 5**	**Mix 6**	**Mix 7**	**Mix 8**
Avg. def. pre (mm)	4.3	4.7	1.8	3.4	6.6	2.6	2.8	2.1
Avg. def. post (mm)	3.6	1.4	1.1	2.0	3.4	0.8	1.1	0.51
Δ def. (%)	-15	-71	-38	-41	-48	-69	-62	-75
Ult. flex. St pre (MPa)	18.1	10.3	7.9	7.8	11.0	4.4	8.8	5.4
Ult. flex. St. post (MPa)	19.6	11.5	10.5	8.1	12.9	5.2	7.5	7.5
Δ flex. St. (%)	+8	+11	+32	+4	+18	+19	-16	+38.6
24-hr comp. St.(MPa)	-	12.8	13.3	9.6	11.5	7.8	7.7	8.3
7- day comp. St. (MPa)	-	-	-	46.5	43.6	41.5	41.9	24.5
28 day comp. St. (MPa)	-	-	-	55.7	56.6	49.8	48.42	37.9
	Mix 9	**Mix 10**	**Mix 11**	**Mix 12**	**Mix 13**	**Mix 14**	**Mix 15**	**Mix 16**
Avg. def. pre (mm)	4.0	2.9	2.6	3.1	3.0	1.6	6.97	4.3
Avg. def. post (mm)	1.4	0.9	1.79	0.8	1.7	0.9	3.91	4.2
Δ def. (%)	-65	-68	-32	-76	-42	-47	-44	-29
Ult. flex. st. (MPa)	9.7	4.3	6.1	6.5	7.3	6.0	13.9	10.4
Ult. flex. st. post (MPa)	9.3	6.1	8.8	5.4	7.8	7.1	17.5	11.5
Δ flex. St. (%)	-4.3	+43	+44	-16	-7	+18	+26.2	+10.6
24-hr comp. St.(MPa)	9.3	6.3	6.1	9.7	8.9	10.2	9.7	11.3
7-day comp. St. (MPa)	23.8	17.6	19.4	21.5	21.9	27.2	-	-
28-day comp St. (MPa)	37.9	35.8	36.0	34.9	36.6	42.3	32.8	36.1

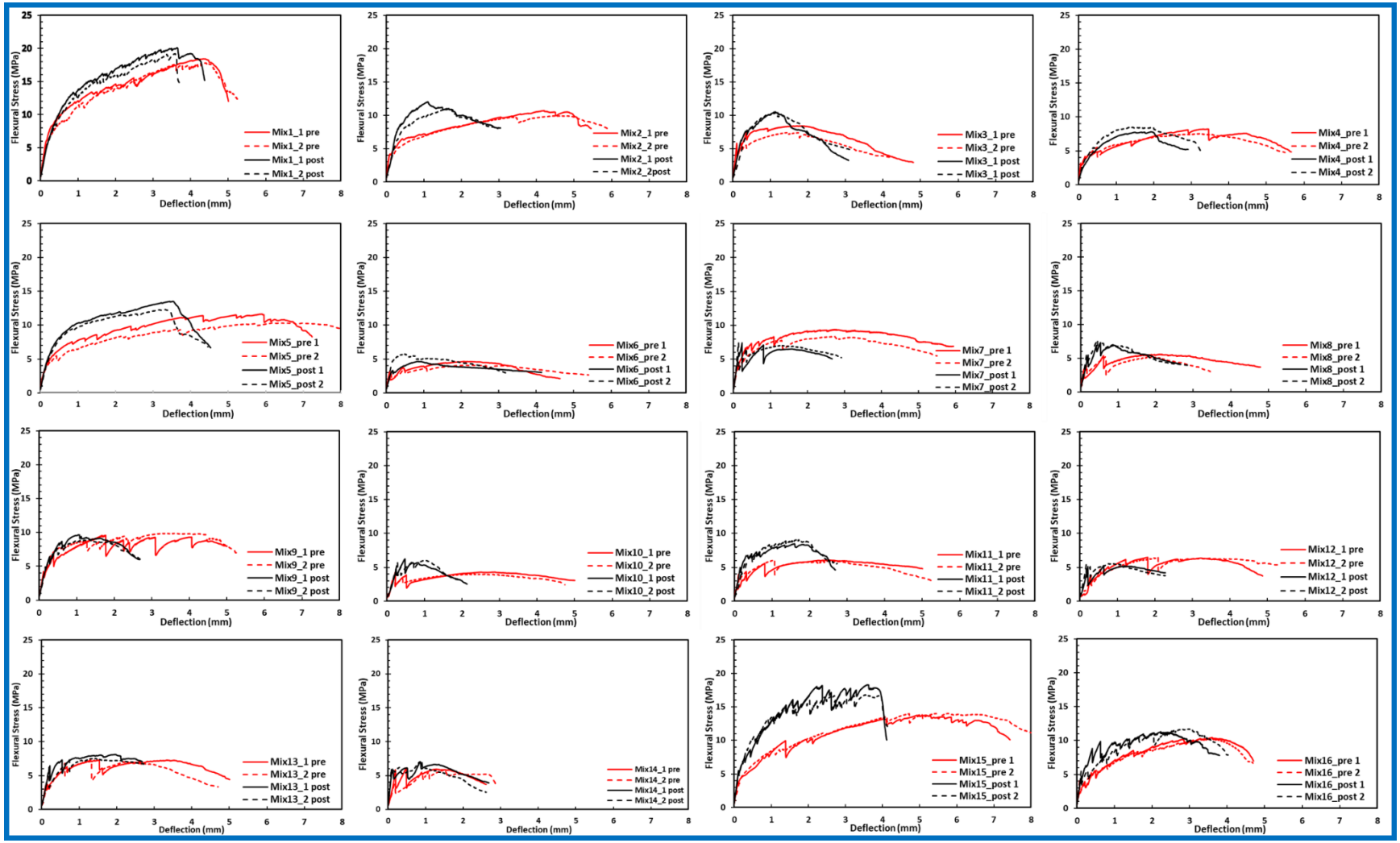

Appendix Figure C.2: Flexural stress vs. deflection curves for mixes 1 to 16.The curves show the stress-deflection curves for the uncarbonated specimens and specimens after 2 days of carbonation.

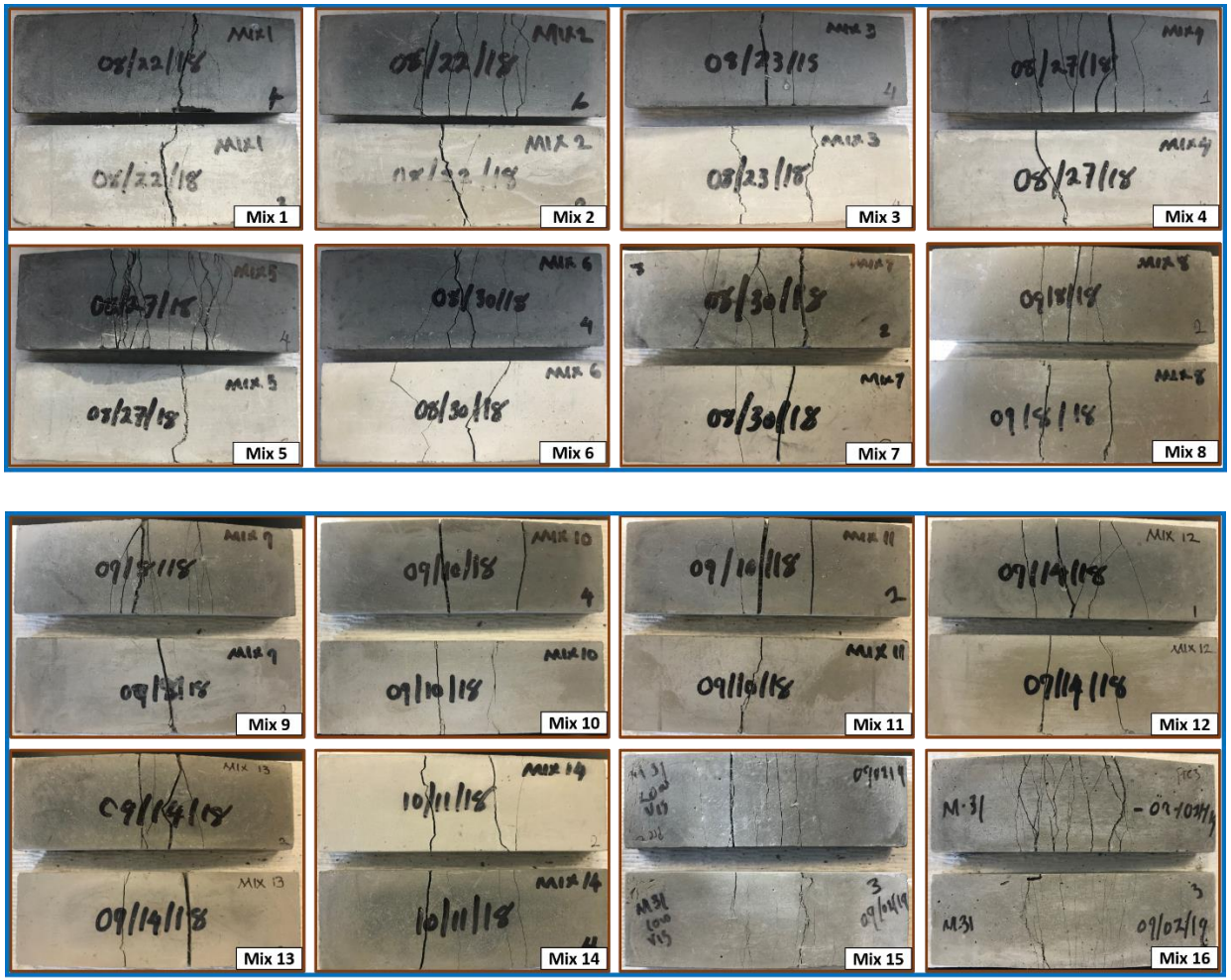

Appendix Figure C.3: Cracks patterns for ECC mixes. The top image for each mix represents the uncarbonated specimen while the bottom image is the carbonated specimen.

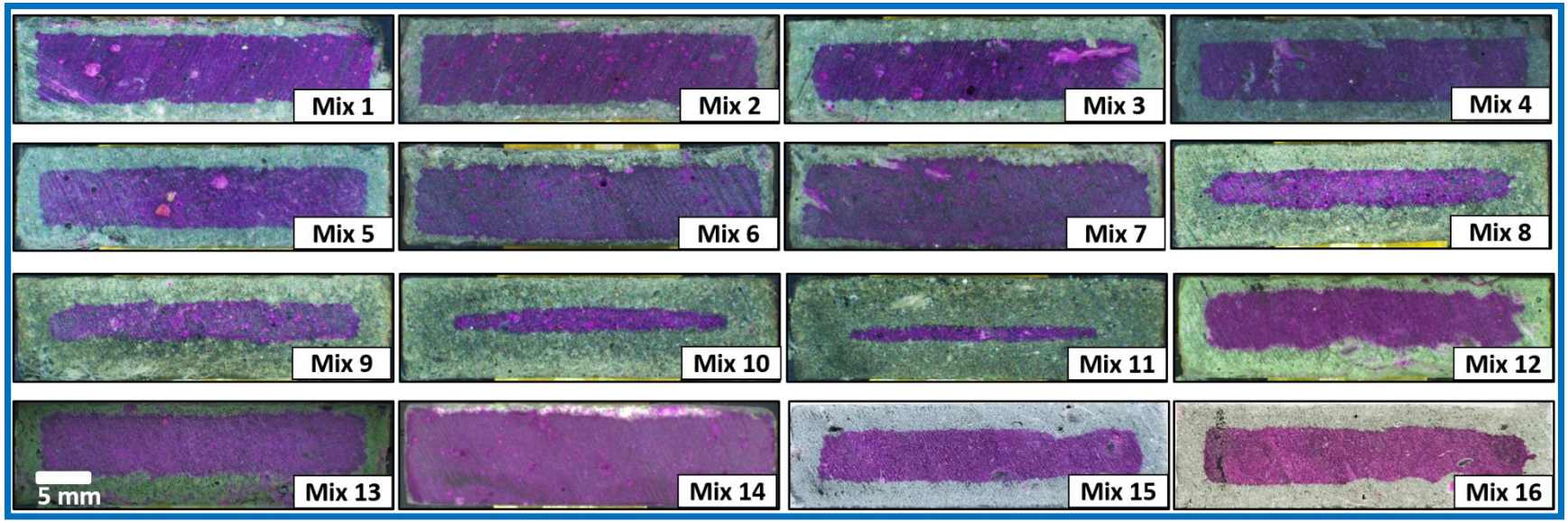

Appendix Figure C.4: Depth of carbonation for different ECC mixes. The pink region represents the uncarbonated region while the clear region is the carbonated region of the specimens.

C.3.3 Effect of mix composition on ECC carbonation

Appendix Figure C.4 shows the optical images of phenolphthalein-stained specimens after carbonation. The pink area represents the uncarbonated area while the brown area is the carbonated area. The result shows that the depth of carbonation is dependent on the composition of the mixtures. For Mix 1 to Mix 3, which have similar mix compositions, the total depth of carbonation was comparable. However, Mix 3 showed a slightly higher depth of carbonation than Mix 1 and Mix 2 likely because of its lower viscosity (**Appendix Table C.3**). Mix 10 and Mix 11 exhibited the largest extent of carbonation (~ 4.1 mm) after 2 days. This is likely due to the high proportion of fly ash in the mix, which has been shown to increase the depth of carbonation. Although Mix 6 and Mix 7 also had similar fly ash content as Mix 10 and Mix 11, Mix 6 and Mix 7 exhibited a lower depth of carbonation due to the higher ratio of cement to fly ash. Apart from Mix 14, which contained only Class H cement, Mix 6 and Mix 7 exhibited the least depth of carbonation. This can be explained by the high content relative to fly ash. For specimens with similar composition but varying fiber volume, no significant difference was observed in the depth of carbonation, indicating that the fiber volume in the range tested did not impact the depth of carbonation in ECC.

Based on slurry rheology (marsh cone flow time, mini-slump diameter, and slurry density), pre- and post-carbonation mechanical properties (flexural deflection, flexural strength, and 24-hour compressive strength), microcracking behavior, and the extent of carbonation, Mix 15 was selected as a suitable mix for wellbore cementing applications during GCS. In **Chapter 4**, Mix 16, which has a similar composition as Mix 15 but with a higher viscosity, was used to carry out the self-healing study. The selection was made because of more consistent microcracking behavior as a result of uniform fiber dispersion in the ECC mix of higher viscosity.

C.4 Conclusion

1) The addition of silica fume enables free-water control in ECC and will not compromise the 24-hour compressive strength requirement for wellbore cementing.
2) A higher fiber volume will promote a higher ductility in wellbore ECC. However, 1.5% fiber volume is likely the practical limit of fiber PVA volume in ECC as fiber clumping, which significantly impacts the flow properties of ECC and its ductility, will occur at 2% fiber volume.
3) The ability of ECC to maintain its ductility and tight microcracking behavior after carbonation depends significantly on the uniform dispersion of fibers in the matrix. Poor fiber dispersion will negatively impact the reproducibility of ductile and tight micro-cracking behavior in unaltered and carbonated ECC.
4) The extent of carbonation in ECC will not be impacted but the volume of fiber in the mix as similar compositions of ECC showed the same extent of carbonation with 1.5% and 2% fiber after reacting with CO_2-acidified water.
5) An increase in superplasticizer content more significantly impacts the mini-slump diameter (yield stress) of the slurry in comparison to the marsh cone flow time (plastic viscosity).

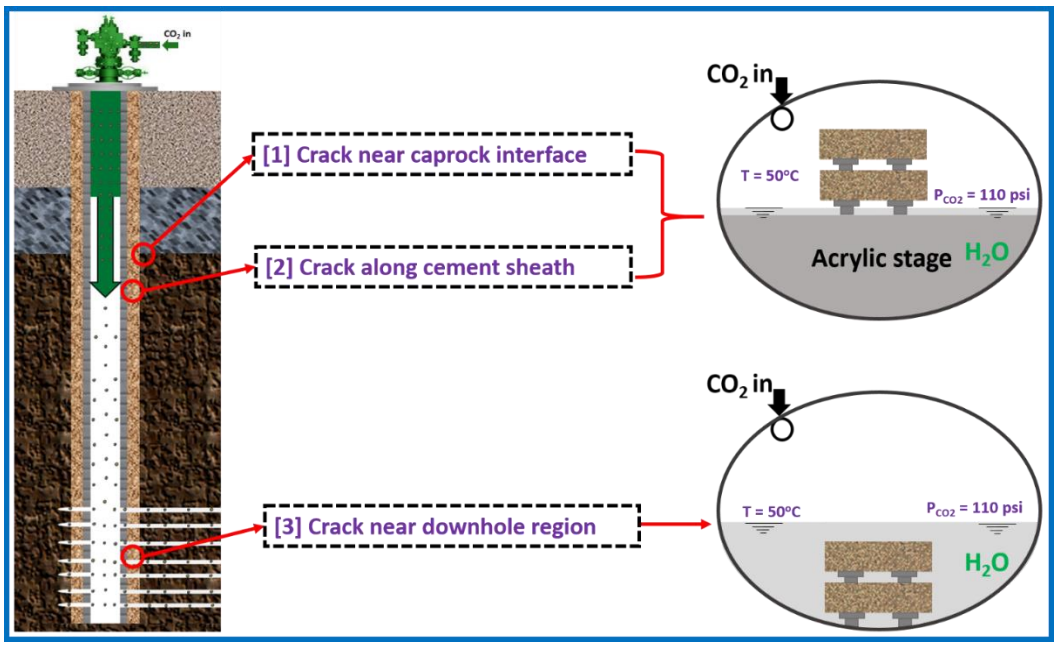

Appendix Figure C.5: Schematics of the experimental conditions tested and the corresponding representative locations in a typical GCS well.

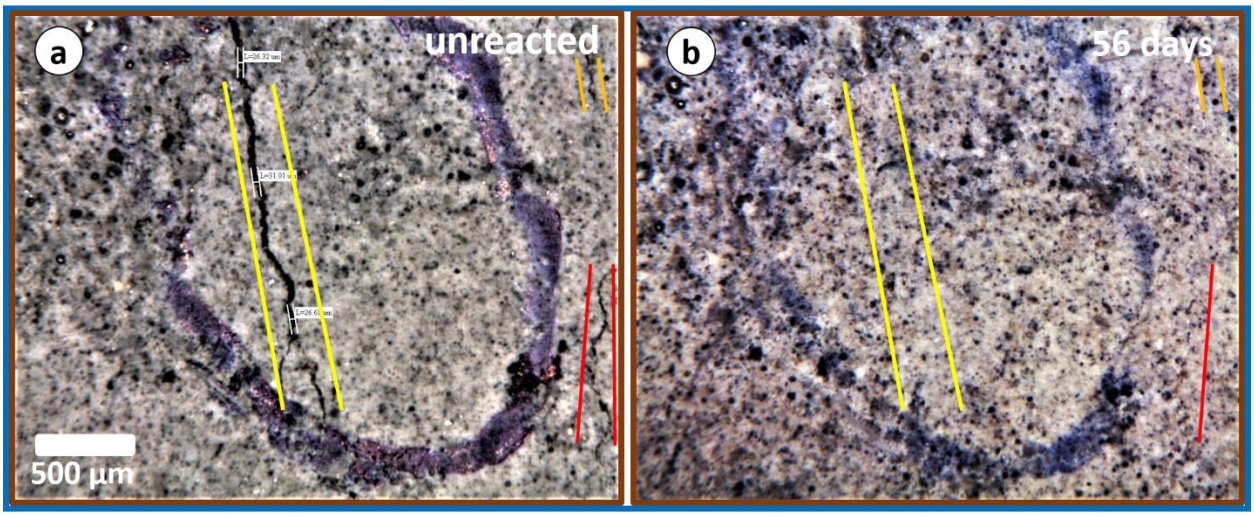

Appendix Figure C.6: (a) optical image of cracked ECC and (b) after exposure to CO_2-acidified water for 56 days. Three cracks with approximate crack widths of 32 um, 12um and 10 um can be seen to have self-healed following 56 days of reaction with CO_2-acidified water.

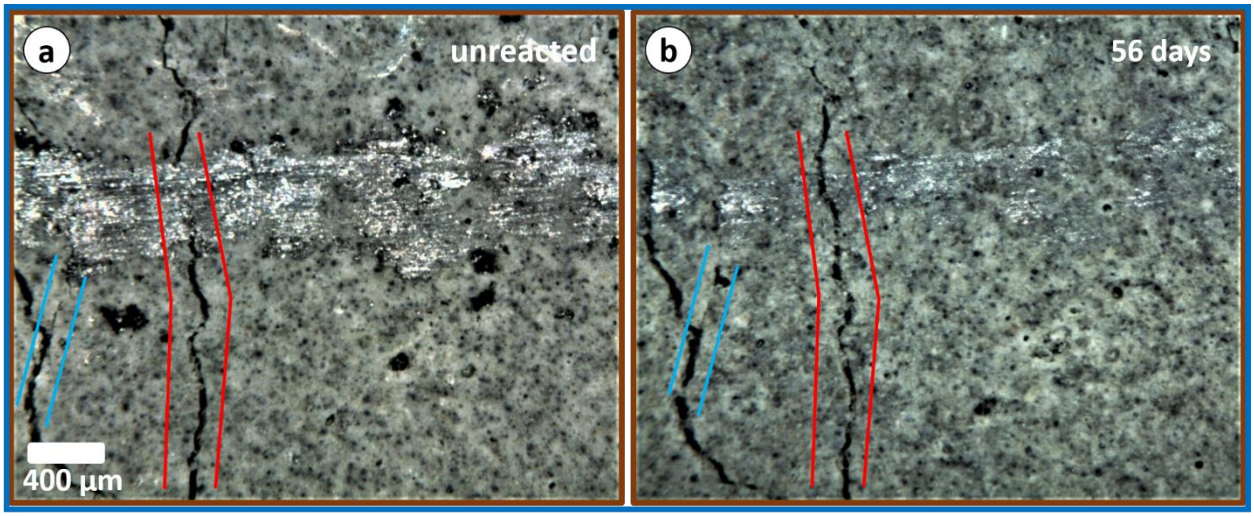

Appendix Figure C.7: (a) optical image of cracked ECC and (b) after exposure to CO_2-acidified water for 56 days. In contrast to the self-healed cracks, these cracks with a similar width as the self-healed cracks did not show self-healing. Parallel lines of similar colors match cracks tracked at different time points.

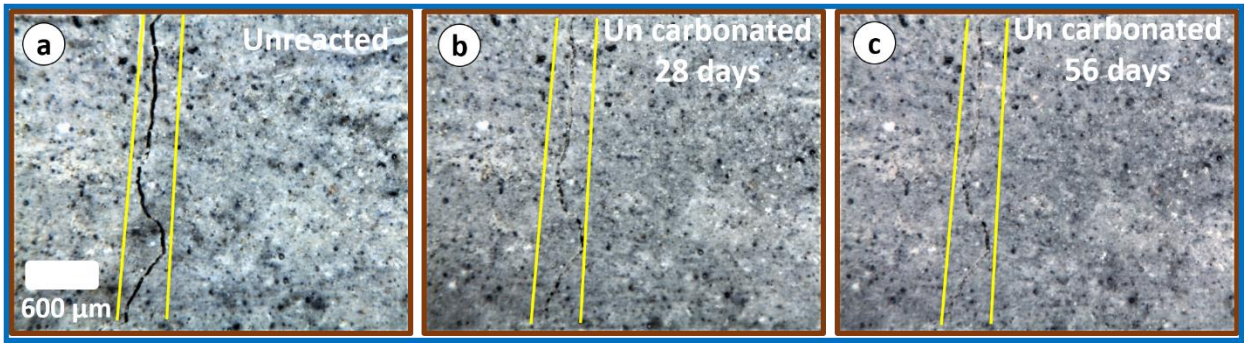

Appendix Figure C.8: (a) optical image of cracked ECC and (b) after exposure to 99% RH atmosphere for 28 days (C) after exposure to 99% RH environment for 56 days. Note that the specimen shows continuous self-healing although it was not exposed to CO_2-environment. Parallel lines show a crack tracked at different time points.

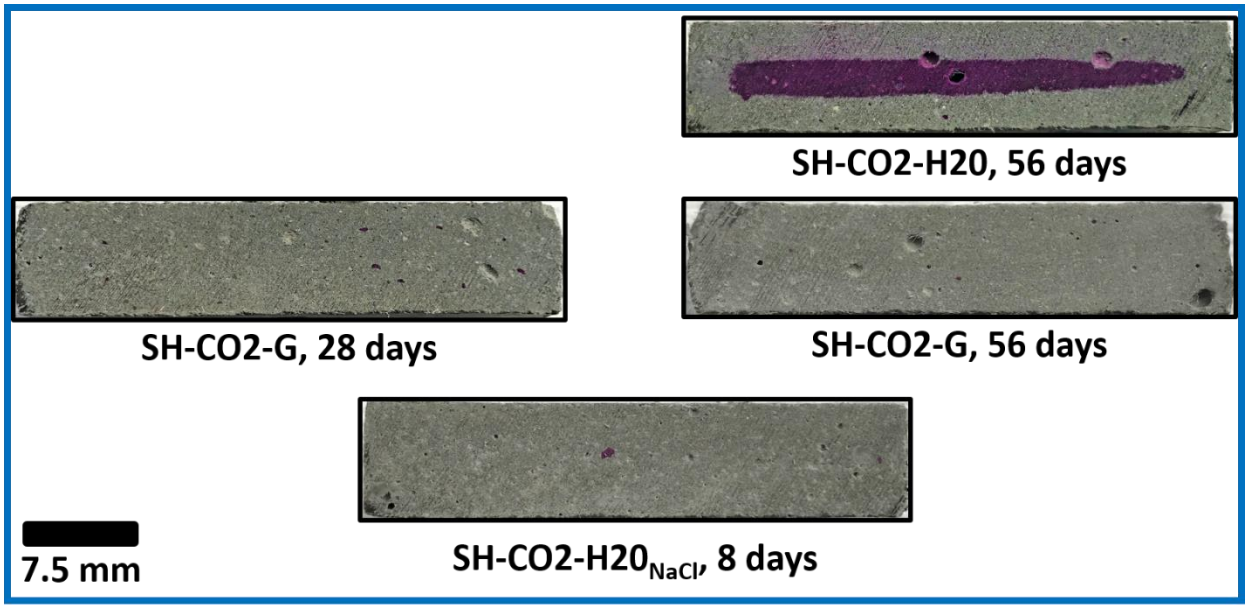

Appendix Figure C.9: Carbonation depth of specimens exposed to different environmental conditional. (1) SH-CO2-H2O: dogbone specimens exposed to CO_2-acidified water, (2) SH-CO2-G: dogbone specimens exposed to CO_2 gas in the presence of DI water, (3) SH-CO2-Gsat: dogbone specimens pre-saturated in water and exposed to CO_2 gas in the presence of DI water, and (4) SH-CO2-GNaCl: dogbone specimens exposed to CO_2 gas in the presence of 1M NaCl solution.

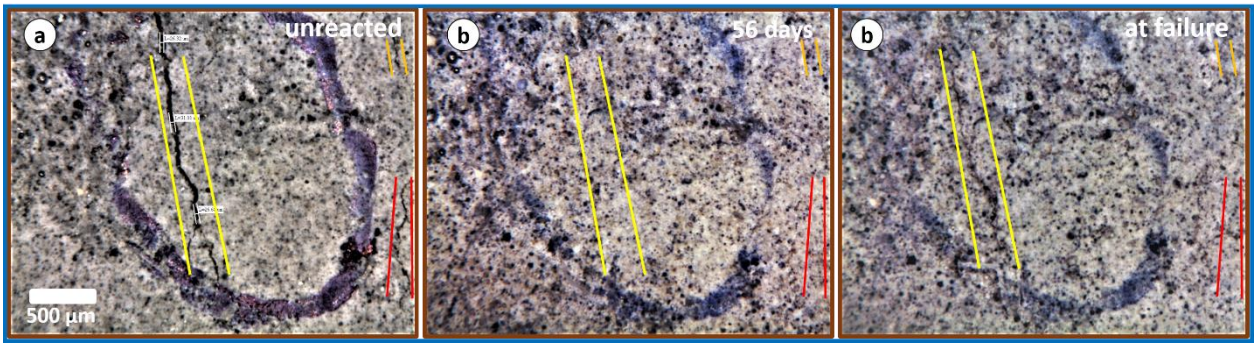

Appendix Figure C.10: (a) optical image of cracked ECC and (b) after exposure to CO_2-acidified water for 56 days (C) after stressing to failure. Parallel lines match similar cracks tracked at different time points. Note that the large crack partially reopened while the small cracks were not reactivated.

C.5 References

Broni-Bediako, E., Joel, O.F., Ofori-Sarpong, G., 2016. Oil Well Cement Additives: A Review of the Common Types. Oil Gas Res. 2, 1–7. https://doi.org/10.4172/2472-0518.1000112

Lam, L., Wong, Y.L., Poon, C.S., 1998. Effect of Fly Ash and Silica Fume on Compressive and Fracture Behaviors of Concrete. Cem. Concr. Res. 28, 271–283. https://doi.org/10.1016/S0008-8846(97)00269-X

Li, M., Li, V.C., 2013. Rheology, fiber dispersion, and robust properties of Engineered Cementitious Composites. Mater. Struct. 46, 405–420. https://doi.org/10.1617/s11527-012-9909-z

Nelson, E.B., 1990. Well Cementing. Newnes.